Kadir Kaan Karaveli

Ph.D. Thesis

AGU 2025

AI-ASSISTED OPTIMIZATION OF SHOT PEENING PROCESS AND INVESTIGATION OF THE EFFECTS OF SECONDARY PROCESSES ON HYDROGEN EMBRITTLEMENT RESISTANCE AND MECHANICAL PERFORMANCE OF SLM-MANUFACTURED ALSI10MG ALLOY

Ph.D. THESIS
SUBMITTED TO THE DEPARTMENT OF MATERIALS SCIENCE AND MECHANICAL ENGINEERING
AND THE GRADUATE SCHOOL OF ENGINEERING AND SCIENCE OF ABDULLAH GUL UNIVERSITY
IN PARTIAL FULFILLMENT OF THE REQUIREMENTS FOR THE DEGREE OF
PHD

By
Kadir Kaan KARAVELİ
June 2025

AI-ASSISTED OPTIMIZATION OF SHOT PEENING PROCESS AND INVESTIGATION OF THE EFFECTS OF SECONDARY PROCESSES ON HYDROGEN EMBRITTLEMENT RESISTANCE AND MECHANICAL PERFORMANCE OF SLM MANUFACTURED ALSI10MG ALLOY

A THESIS
SUBMITTED TO THE DEPARTMENT OF MATERIALS SCIENCE AND MECHANICAL ENGINEERING
AND THE GRADUATE SCHOOL OF ENGINEERING AND SCIENCE OF ABDULLAH GUL UNIVERSITY
IN PARTIAL FULFILLMENT OF THE REQUIREMENTS
FOR THE DEGREE OF
PHD

By

Kadir Kaan Karaveli

June 2025

SCIENTIFIC ETHICS COMPLIANCE

I hereby declare that all information in this document has been obtained in accordance with academic rules and ethical conduct. I also declare that, as required by these rules and conduct, I have fully cited and referenced all materials and results that are not original to this work.

Name-Surname: Kadir Kaan Karaveli
Signature :

REGULATORY COMPLIANCE

Ph.D. thesis titled AI-Assisted Optimization of Shot Peening Process and Investigation of the Effects of Secondary Processes on Hydrogen Embrittlement Resistance and Mechanical Performance of SLM-Manufactured AlSi10Mg Alloy has been prepared in accordance with the Thesis Writing Guidelines of the Abdullah Gül University, Graduate School of Engineering & Science.

Prepared By	Advisor
Kadir Kaan KARAVELİ	Prof. Dr. Burak BAL

Head of the Materials Science and Mechanical Engineering Program
Assist. Prof. Dr. Zeliha Soran Erdem

ACCEPTANCE AND APPROVAL

Ph.D. thesis titled AI-Assisted Optimization of Shot Peening Process and Investigation of the Effects of Secondary Processes on Hydrogen Embrittlement Resistance and Mechanical Performance of SLM-Manufactured AlSi10Mg Alloy and prepared by Kadir Kaan Karaveli has been accepted by the jury in the Materials Science and Mechanical Engineering Graduate Program at Abdullah Gül University, Graduate School of Engineering & Science.

28 /05 / 2025

JURY:

Advisor : Prof. Dr. Burak Bal……………………………………………………………………

Member : Assist. Prof. Dr. İlker Erdem…………………………………………………………

Member : Assoc. Prof. Dr. Ramazan Ünlü………………………………………………………

Member : Assoc. Prof. Dr. Murat Aydın…………………………………………………………

Member : Assoc. Prof. Dr. Umut Çalışkan………………………………………………………

APPROVAL:

The acceptance of this Ph.D. thesis has been approved by the decision of the Abdullah Gül University, Graduate School of Engineering & Science, Executive Board dated ….. /….. / ……….. and numbered ………….……. .

……….. /……….. / ………..

Graduate School Dean
Prof. İrfan ALAN

ABSTRACT

AI-ASSISTED OPTIMIZATION OF SHOT PEENING PROCESS AND INVESTIGATION OF THE EFFECTS OF SECONDARY PROCESSES ON HYDROGEN EMBRITTLEMENT RESISTANCE AND MECHANICAL PERFORMANCE OF SLM MANUFACTURED ALSI10MG ALLOY

Kadir Kaan Karaveli
Ph.D. in Materials Science and Mechanical Engineering
Advisor: Prof. Dr. Burak Bal
June 2025

This thesis investigates the optimization of shot peening processes and the mitigation of hydrogen embrittlement in AlSi10Mg alloys produced via Selective Laser Melting (SLM). Chapter one reviews process optimization techniques (e.g., Taguchi, Box-Behnken), additive manufacturing (AM) challenges like residual stress and porosity, and introduces hydrogen embrittlement mechanisms and testing methods. Chapters two and three focus on optimizing shot peening intensity using AI-based approaches validated by Almen tests and analyze real-world aviation failures, such as Bell 412EP and Piper PA-32R, to highlight hydrogen embrittlement's impact on component degradation. Chapters four and five explore the effects of strain rates and post-processing treatments, including shot peening and heat treatment, on mechanical performance, demonstrating significant improvements in fatigue resistance. Advanced strategies for mitigating hydrogen embrittlement are also proposed. The thesis concludes by emphasizing the societal benefits of enhanced material reliability and sustainability, suggesting future research into AI-assisted methods and real-time monitoring systems in manufacturing.

Keywords: Additive Manufacturing, Shot Peening, Hydrogen Embrittlement, AI Optimization, AlSi10Mg Alloy

ÖZET

YAPAY ZEKA DESTEKLİ SHOT PEENİNG PROSESİNİN OPTİMİZASYONU VE İKİNCİL PROSESLERİN SLM İLE ÜRETİLEN ALSİ10MG ALAŞIMININ HİDROJEN KIRILGANLIK DİRENCİ VE MEKANİK PERFORMANSI ÜZERİNDEKİ ETKİLERİNİN İNCELENMESİ

Kadir Kaan Karaveli
Malzeme Bilimi ve Makine Mühendisliği Anabilim Dalı Doktora
Tez Danışmanı: Prof. Dr. Burak Bal
Haziran 2025

Bu tez, Seçici Lazer Ergitme (SLM) yöntemiyle üretilen AlSi10Mg alaşımlarında bilyalı dövme işlemlerinin optimizasyonunu ve hidrojen gevrekliğinin azaltılmasını araştırmaktadır. Birinci bölümde, süreç optimizasyon yöntemleri (ör. Taguchi, Box-Behnken), metal katkı üretimdeki (AM) sorunlar (artık gerilme, gözeneklilik) ve hidrojen gevrekliğinin mekanizmaları ile test yöntemleri ele alınmıştır. İkinci ve üçüncü bölümler, Almen testleriyle doğrulanan yapay zeka tabanlı yaklaşımlarla bilyalı dövme yoğunluğunun optimizasyonunu ve Bell 412EP ile Piper PA-32R gibi gerçek havacılık arızalarını inceleyerek hidrojen gevrekliğinin bileşenlerdeki etkilerini analiz etmektedir. Dördüncü ve beşinci bölümler, SLM ile üretilen AlSi10Mg alaşımlarının mekanik performansına, gerinim hızı ve işlem sonrası uygulamaların (bilyalı dövme, ısıl işlem) etkilerini değerlendirmiş ve yorulma direncinde önemli iyileşmeler göstermiştir. Ayrıca hidrojen gevrekliğini önlemek için ileri düzey stratejiler önerilmiştir. Tez, artırılmış malzeme güvenilirliği ve sürdürülebilirliğin toplumsal faydalarını vurgulamakta ve yapay zeka destekli yöntemler ile üretimde gerçek zamanlı izleme sistemleri üzerine gelecekteki araştırmaları önermektedir.

Anahtar kelimeler: Katmanlı Üretim, Bilyalı Dövme, Hidrojen Kırılganlığı, Yapay Zeka Optimizasyonu, AlSi10Mg Alaşımı

Acknowledgements

I would like to take a moment to express my heartfelt gratitude to everyone who supported me throughout this challenging journey.

First and foremost, I am deeply grateful to my advisor, Prof. Dr. Burak Bal, for his unwavering patience, guidance, and continuous support during my Ph.D. studies. His immense knowledge and expertise have been invaluable in shaping my research. His enthusiasm and passion for science have profoundly inspired me, leaving a lasting impact on both my academic and personal life. This journey would not have been possible without his mentorship, motivation, and encouragement.

I would also like to extend my sincere thanks to my thesis committee members, Asst. Prof. Dr. İlker Erdem and Assoc. Prof. Dr. Ramazan Ünlü, for their insightful feedback and challenging questions. Their perspectives have significantly enriched my research and broadened my academic vision.

Special thanks go to my colleagues and supporters at Turkish Aerospace: Faruk Oğuz, Osman Çağlar Baysallı, Arman Uluoğlu, Ali Ayaz, Sefa Kayır, Alihan Cambaz, Ömer Özgüner, Assoc. Prof Dr. Emre Doruk, Assoc. Prof. Dr. Tamer Saraçyakuboğlu, Dr. Mete Bakır, Dr. Ahmet Alptuğ Tanrıkulu, Kadir Göker Önder, Zafer Yıldırım, Murat Saatçi, Kerem Korkmaz, Mustafa Sarıkaya, Sertan Karaşoğlu, Ahmet Can Doğancı, and Emre Yılmaz. Their help during the test sessions were invaluable.

I am also deeply thankful to my dear friends Ahmet Taha Karakaya, Büşra Karakaya, Kevser Tuğba Yaman, Abdülvehab Yaman, and Sümeyye Betül Özoğul for their constant support and companionship. Their encouragement and kindness have been a source of immense strength throughout this process.

To my beloved wife, Ayşe Berna Karaveli, my parents, Engin Karaveli and Nurten Karaveli, my sister Kübra Özcan, my brothers Hamza Alp Karaveli and Gökhan Özcan, and my uncles Abdulah Buğrahan Karaveli, Erol Dok, and Birol Dok: words cannot express my gratitude for your unwavering belief in me and your constant encouragement to pursue my dreams. Your love and support have been my greatest source of strength.

This Ph.D. study was generously supported by Turkish Aerospace's Scientific Research Project Program, under grant number 2021-TUSAS-BAP-01.

TABLE OF CONTENTS

1. **INTRODUCTION 1**

1.1 INTRODUCTION TO PROCESS OPTIMIZATION 3

1.1.1 Design of Experiments and Its Models 4

1.1.1.1 Taguchi Design (TD) 5

1.1.1.2 Box Behnken Design (BBD) 6

1.1.1.3 Factorial Design (FD) 6

1.1.1.4 Central Composite Design (CCD) 7

1.1.1.5 One Variable at a Time (OVAT) 7

1.1.1.6 D-Optimal Design 8

1.1.1.7 Comparison of Experimental Design Methods 8

1.1.2 Mathematical Modelling 10

1.1.2.1 Neuro Regression Method (NRM) 11

1.1.3 Optimization Methods 12

1.2 INTRODUCTION TO ADDITIVE MANUFACTURING 14

1.2.1 Metal Additive Manufacturing 15

1.2.1 Post-Processes in AM 17

1.3 INTRODUCTION TO HYDROGEN EMBRITTLEMENT 20

1.3.1 Hydrogen Embrittlement Mechanisms 21

1.3.1 Hydrogen Embrittlement Testing Methods 24

2. **COMPREHENSIVE OPTIMIZATION OF SHOT PEENING INTENSITY USING A HYBRID MODEL WITH AI-BASED TECHNIQUES VIA ALMEN TESTS 26**

2.1 INTRODUCTION 27

2.2 EXPERIMENTAL PROCEDURE 29

2.3 RESULTS AND DISCUSSIONS 35

2.3 CONCLUSION 45

3. **CRITICAL FAILURES IN AVIATION COMPONENTS: THE ROLE OF HYDROGEN EMBRITTLEMENT 46**

3.1 INTRODUCTION OF HYDROGEN EMBRITTLEMENT 46

3.2 AIRWORTHINESS DIRECTIVES 52

3.3 PROTECTION MECHANISMS AGAINST HYDROGEN EMBRITTLEMENT 53

3.3.1 Failure of the Bell 412EP Helicopter (ERA10TA493) 56
3.3.2 Failure of the Bell 222U Helicopter (CEN10FA291) 59
3.3.3 Failure of the Piper PA-32R-301T (IAD02FA091) 63
3.3.4 Failure of the Piper PA-32R-301 (MIA02LA108) 66
3.3.5 Failure of the Center Landing Gear on FedEx MD-11 (ENG08IA025) 69
3.4 CONCLUSIONS AND RECOMMENDATIONS 71

4. **STRAIN RATE AND POST PROCESSING EFFECT ON MECHANICAL PROPERTIES OF ADDITIVELY MANUFACTURED ALSI10MG ALLOYS 73**

4.1 INTRODUCTION 74
4.2 MATERIALS AND METHODS 76
4.2.1 Specimen Fabrication 76
4.2.2 Post-Process Treatments 77
4.2.3 Mechanical Testing 77
4.3 RESULTS AND DISCUSSIONS 78
4.4 CONCLUSIONS 86

5. **MITIGATING HYDROGEN EMBRITTLEMENT IN ADDITIVELY MANUFACTURED ALSI10MG ALLOYS: THE ROLE OF POST-PROCESSING TREATMENTS 88**

5.1 INTRODUCTION 89
5.2 MATERIALS AND METHODS 91
5.3 RESULTS 94
5.3.1 Secondary Process effects on hydrogen embrittlement 98
5.3.2 Shot Peening effects on hydrogen embrittlement 101
5.3.3 Strain Rate effects on hydrogen embrittlement 103
5.4 DISCUSSIONS 105
5.5 CONCLUSIONS 108

6. **CONCLUSIONS AND FUTURE PROSPECTS 110**

6.1 CONCLUSIONS 110
6.2 SOCIETAL IMPACT AND CONTRIBUTION TO GLOBAL SUSTAINABILITY 111
6.3 FUTURE PROSPECTS 113

LIST OF FIGURES

Figure 1.1 Additive Manufacturing Technologies 15
Figure 1.2 Secondary Process Methods 18
Figure 1.3 HE mechanisms' schematic diagrams, (a) HIPT; (b) HEDE; (c) HELP; (d) HEDE + HELP (e) NVC [106]. 22
Figure 2.1 Shot Peening Process for Almen Test Strips 31
Figure 2.2 Process optimization flow chart of shot peening 32
Figure 2.3 Intensity vs Inverse Feedrate for SOTN Model (Air Pressure=3 Bar, Mass Flow=4.5 kg·min-1, Impact Angle=90 Degree Distance Between Nozzle and Specimen =25 cm) 38
Figure 2.4 Intensity vs a) Air Pressure and Inverse Feedrate (Mass Flow = 4.5 kg·min^{-1}, Impact Angle = 90°, Distance Between Nozzle and Specimen = 25 cm), b) Mass Flow and Inverse Feedrate (Air Pressure = 3 bar, Impact Angle = 90°, Distance Between Nozzle and Specimen = 25 cm), c) Impact Angle and Inverse Feedrate (Air Pressure = 3 bar, Mass Flow = 4.5 kg·min^{-1}, Distance Between Nozzle and Specimen = 25 cm), d) Distance Between Nozzle and Specimen and Inverse Feedrate (Air Pressure = 3 bar, Mass Flow = 4.5 kg·min^{-1}, Impact Angle = 90°) 39
Figure 2.5 Target intensity vs optimized intensity results for a) Differential Evolution, b) Nelder-Mead, c) Simulated Annealing and d) Random Search 40
Figure 2.6 Target intensity vs hybrid optimized intensity results 42
Figure 2.7 Monte Carlo Mean Intensity Simulation Results 43
Figure 2.8 Figure caption Monte Carlo Standard Deviation Results 44
Figure 3.1 Aircraft incident cases with probable cause 49
Figure 3.2 Global Aviation Accidents (2017-2022) [162] 50
Figure 3.3 Yearly distribution of aviation accident causes (2017-2022) [162] 51
Figure 3.5 The Bell 412EP helicopter resting in Jamaica Bay after the emergency landing [210]. 56
Figure 3.6 Detailed view of the fractured output drive gear from the reduction gearbox [210]. 57
Figure 3.7 Close-up of the origin region of the fatigue crack on the output drive gear, showing the initial intergranular cracking due to hydrogen embrittlement [210]. 58

Figure 3.8 Microscopic view of the fracture surface, showing the distinct patterns of fatigue crack propagation starting from the hydrogen-embrittled region [210]. 58
Figure 3.9 Image showing the rotor head of the Bell 222U helicopter before the accident, with critical components identified [211]. 60
Figure 3.10 Separated rotor components prior to disassembly, highlighting the critical assemblies (swashplate, drive assembly, and pitch links) [211]................................... 61
Figure 3.11 SEM image of radial cracks on the washer face of the A-side pin, showing areas of localized plasticity [211]. 62
Figure 3.12 Higher magnification SEM image showing the transition between brittle cleavage and ductile dimples on the A-side drive pin fracture surface [211]................ 63
Figure 3.13 Image of the crankshaft assembly and fractured crankshaft gear retaining bolt after disassembly [212]. 64
Figure 3.14 SEM image showing intergranular cracking along the fracture surface of the crankshaft bolt, indicating hydrogen-assisted cracking [212]. 65
Figure 3.15 Front view of the aircraft wreckage after recovery at Meridian Aviation [213]. 66
Figure 3.16 Image of the disassembled engine components, highlighting the fractured crankshaft gear bolt [213]. 67
Figure 3.16 SEM image under 1000x magnification showing intergranular separation on the fractured surface of the crankshaft gear bolt, indicating hydrogen-assisted cracking [213]. 68
Figure 3.17 Photograph of the cracked CLG strut cylinder, showing the longitudinal crack along the aft side [214]. 69
Figure 3.18 Cross-sectional view of the CLG strut cylinder, showing the intergranular cracking that initiated the failure [214]... 70
Figure 3.19 SEM image of the fracture surface, showing a combination of intergranular cracking and ductile overload [214]. 71
Figure 4.1 Sample Drawings and Production Workflow for Additive Manufacturing .. 77
Figure 4.2 Force-Displacement curves for AlSi10Mg specimens under different post-processing treatments (AL, AL-SP, AL-SR, AL-SR-SP) and strain rates (10^{-1} and 15 • 10^{-3} s^{-1}). 79
Figure 4.3 Engineering Stress-Engineering Strain curves for AlSi10Mg specimens under different post-processing treatments (AL, AL-SR, AL-SP, AL-SR-SP) and strain rates (10^{-1} and 15 • 10^{-3} s^{-1}). 80

Figure 4.4 True Stress-True Strain curves for AlSi10Mg specimens under different post-processing treatments (AL, AL-SP, AL-SR, AL-SR-SP) and strain rates (10^{-1} and 15 • 10^{-3} s^{-1}). 81
Figure 4.4 Strain rate effect on true stress values on samples 84
Figure 5.1 Sample Drawings 92
Figure 5.2 Tensile test of samples with extensometer 93
Figure 5.3 True Stress strain values of all samples with 0.1 and 0.015 s^{-1} strain rates... 95
Figure 5.4 True Stress strain values of all samples with 0.1 s^{-1} strain rate. 95
Figure 5.5 True Stress strain values of all samples with 0.015 s^{-1} strain rate. 96
Figure 5.6 Secondary Process (as-built, SP, SR, SP and SR+SP) effects on hydrogen embrittlement at different strain rates 99
Figure 5.7 Effect of HC before and after SP 102
Figure 5.8 Strain rate effect on true stress values on samples and strain rate sensitivity (*m*) values 104

LIST OF TABLES

Table 1.1 DOE Method Comparisons.. 9
Table 2.1 Shot Peening Process Parameters 29
Table 2.2 Chemical Composition of SAE 1070/75 TR Carbon Steel (wt.%) [136]...... 30
Table 2.3 Multiple regression model types... 33
Table 2.4 Results of neuro-regression models for shot peening almen test samples...... 35
Table 4.1 Powder chemical composition (wt.-%).. 76
Table 4.2 Specimens' tensile test results 82
Table 4.3 Strain rate sensitivity 84
Table 5.1 Powder chemical composition (wt.-%).. 91
Table 5.2 Summary of Post-Processing and Testing Combinations for SLM-Produced AlSi10Mg Samples... 92
Table 5.3 Specimens' tensile test results 96
Table 5.4 HE Index of Specimens 100

LIST OF ABBREVIATIONS

AM	Additive Manufacturing
BCC	Body-Centered Cubic
CHA	Cathodic Hydrogen Absorption
CM	Conventionally Manufacturing
EAC	Environmentally Assisted Cracking
EBM	Electron Beam Melting
EHE	Environmental (External) Hydrogen Embrittlement
FCC	Face-Centered Cubic
EPBF	Electron Beam Powder Bed Fusion
FCT	Face-Centered Tetragonal
FCGR	Fatigue Crack Growth Rate
FPZ	Fracture Process Zone
GB	Grain Boundary
HAC	Hydrogen-Assisted Cracking
HCF	High Cycle Fatigue
HE	Hydrogen Embrittlement
HEDE	Hydrogen-Enhanced Decoherence
HELP	Hydrogen-Enhanced Localized Plasticity
HIC	Hydrogen-Induced Cracking
HT	Heat Treatment
HSR	High Strain Rate
IG	Intergranular
IHE	Internal Hydrogen Embrittlement
LCF	Low Cycle Fatigue
LPBF	Laser Powder Bed Fusion
LSR	Low Strain Rate
SCC	Stress Corrosion Cracking
SLM	Selective Laser Melting
TG	Transgranular
UMT	Unified Mechanics Theory

To My Family

Chapter 1

Introduction

The field of materials science has witnessed a paradigm shift with the introduction of advanced manufacturing technologies, particularly Additive Manufacturing (AM). Selective Laser Melting (SLM) is one of the most widely adopted additive manufacturing methods due to its capacity to produce geometrically intricate and lightweight parts with enhanced mechanical performance, directly based on design files. The process utilizes a high-powered laser to melt metal powders layer by layer, enabling precise fabrication of components with minimal material usage and close-to-final dimensions. These features have positioned SLM as a cornerstone technology in industries such as aerospace, automotive, and defense, where high performance and lightweight design are paramount.

AlSi10Mg, a popular aluminum-silicon alloy in SLM applications, is favored for its outstanding mechanical behavior, particularly its strength-to-weight efficiency, fatigue endurance, and thermal conductivity, making it ideal for demanding engineering uses. These characteristics make AlSi10Mg a preferred material for applications requiring structural integrity and durability under cyclic loading. However, the layer-by-layer nature of SLM introduces challenges such as residual tensile stresses, microstructural heterogeneity, and porosity, which can compromise the mechanical performance of components. These issues necessitate the application of post-processing methods, such as shot peening, to enhance surface properties and mitigate inherent manufacturing defects.

Aside from mechanical limitations, AlSi10Mg and similar lightweight alloys face the risk of hydrogen embrittlement (HE). This occurs when hydrogen penetrates the alloy's microstructure, causing a noticeable decrease in both ductility and toughness. The presence of hydrogen embrittlement significantly compromises the structural soundness of components, especially under hydrogen-rich conditions like fuel cells or aggressive industrial surroundings. Despite extensive research on hydrogen embrittlement mechanisms, the interplay between HE and post-processing techniques in SLM-produced components remains underexplored.

This thesis aims to address these critical gaps by focusing on the optimization of shot peening parameters for SLM-produced AlSi10Mg components. By employing a combination of experimental techniques and computational tools, the study seeks to enhance the mechanical performance of the alloy while mitigating its susceptibility to hydrogen embrittlement. The research outcomes are expected to contribute significantly to the broader adoption of SLM in high-performance and safety-critical applications.

The development of new manufacturing technologies has always paralleled the evolving demands of industrial applications. From the aerospace sector to automotive and biomedical fields, the need for lightweight, geometrically complex, and high-performance components has become paramount. In response to these needs, Additive Manufacturing (AM), often referred to as 3D printing, has emerged as a transformative technology. By enabling layer-by-layer construction of parts directly from digital models, AM minimizes material waste and allows unprecedented design flexibility.

Selective Laser Melting (SLM) distinguishes itself from other additive manufacturing methods through its capacity to fabricate fully dense metal parts with customizable mechanical characteristics. In SLM, a high-energy laser selectively melts powdered metal material, building components layer by layer. This method is especially beneficial in producing complex and lightweight structures for high-performance uses, as it overcomes the limitations found in conventional processes such as casting or machining. Industries such as aerospace, automotive, and defense have widely integrated SLM into their production workflows due to its efficiency in material use and its ability to ensure structural integrity in critical components.

Despite its transformative potential, SLM is not without its challenges. The process introduces intrinsic defects, including residual stresses, porosity, and anisotropy in mechanical properties. Due to these challenges and the microstructural traits inherent to SLM-fabricated parts, additional post-processing strategies are frequently required to improve component performance. A commonly applied method is shot peening, known for increasing surface hardness, introducing beneficial compressive residual stresses, and reducing surface-level defects.

In addition to these mechanical challenges, the interaction of hydrogen with materials has emerged as a critical issue in high-performance applications. Hydrogen embrittlement (HE) refers to the penetration of hydrogen atoms into the internal structure of a material, significantly diminishing its ductility and toughness and often resulting in early failure. Lightweight materials such as AlSi10Mg, an aluminum-silicon alloy extensively used in SLM, are particularly susceptible to hydrogen embrittlement under certain conditions. Understanding the mechanisms of hydrogen embrittlement and its mitigation through advanced post-processing methods forms a critical research area, especially in industries where safety and performance are non-negotiable.

This thesis addresses these intertwined challenges by focusing on the optimization of shot peening parameters for SLM-produced AlSi10Mg components to improve their mechanical properties and mitigate hydrogen embrittlement. By employing a combination of experimental methodologies, computational modeling, and Artificial Intelligence (AI)-driven optimization, the research bridges key gaps in the literature and contributes to the broader adoption of SLM in demanding industrial applications.

1.1 Introduction to Process Optimization

Process optimization is a fundamental approach to improving the efficiency, reliability, and quality of systems that transform inputs into outputs. At its core, process optimization seeks to identify and refine the parameters influencing a process to achieve better performance. These parameters can be classified as controllable, which can be adjusted or held constant (e.g., temperature, pressure), and uncontrollable, which are subject to variability and external influences (e.g., environmental conditions). By analyzing and adjusting these parameters, organizations can design processes that minimize inefficiencies, reduce costs, and improve output quality [1].

Process optimization plays a key role in overcoming the challenges faced by contemporary manufacturing and service sectors [2]. As businesses strive to meet increasing demands while operating within limited resources, optimization provides a structured way to maximize productivity, reduce waste, and enhance the consistency of outputs. Moreover, as global emphasis on sustainability grows, process optimization becomes vital for reducing energy consumption, minimizing environmental impact, and achieving eco-friendly operational goals [3]. These benefits make it an indispensable tool for industries seeking long-term success and competitiveness.

Applications of process optimization are widespread across various sectors. In manufacturing, optimization ensures smoother production flows by identifying bottlenecks, reducing defects, and increasing throughput [4,5]. In healthcare, it supports efficient scheduling, resource allocation, and patient care delivery [6,7]. Supply chain and logistics processes benefit from optimization through improved routing, inventory control, and delivery precision. The energy sector leverages process optimization to enhance energy production efficiency and reduce losses [8]. Additionally, in fields such as artificial intelligence and technology development, optimization plays a key role in refining algorithms, improving system performance, and managing large-scale data processes [9,10].

To systematically approach process optimization, various methodologies have been developed. This thesis will focus on three key areas: Design of Experiments (DoE), Mathematical Modeling, and the Optimization Process. Design of Experiments provides a structured framework for identifying the relationships between input factors and output performance. Mathematical modeling enables the quantitative representation of processes, allowing for predictive analysis and simulations. Finally, the optimization process brings these elements together by defining objectives, constraints, and methods for achieving the desired outcomes. These approaches form the foundation for understanding and improving processes across industries, which will be explored in detail in subsequent sections.

1.1.1 Design of Experiments and Its Models

The Design of Experiments (DoE) serves as a structured methodology for process improvement by clarifying the link between influencing parameters and resulting outputs. Its systematic nature facilitates controlled trials, helping scientists and engineers gain actionable insights into process behaviors [11]. It not only identifies critical factors but also optimizes system performance with minimal resource expenditure, thereby offering significant value in both research and industrial applications [12]. For example, in manufacturing, DoE is widely applied to optimize production processes, such as improving product quality by reducing defects and fine-tuning process parameters like temperature and pressure. In healthcare, it is used to streamline patient care by optimizing workflows and treatment protocols, while in agriculture, DoE supports the development of better crop management strategies by examining factors such as irrigation levels and soil composition.

A typical DoE study comprises three core components: factors, levels, and responses [13]. Factors are variables that influence the output, while levels represent the specific values these factors can assume. Responses are the outputs measured during experiments, providing insight into the performance of the process. By systematically varying the factors, DoE identifies statistical patterns and relationships, paving the way for process optimization and improved outcomes. For example, in energy systems, DoE can optimize factors such as energy input and operating conditions to reduce consumption while maintaining output efficiency. Similarly, in pharmaceutical research, the method is used to evaluate combinations of chemical compounds to enhance drug efficacy and safety [14].

To ensure robust and reliable results, DoE relies on three fundamental principles: replication, randomization, and blocking [15]. Replication involves repeating experiments to minimize the impact of random errors and enhance the accuracy of results. Randomization eliminates bias by ensuring that experimental runs are conducted in a random sequence, reducing the influence of external factors such as operator skill levels or material variability. Blocking groups experiments into homogeneous sets to account for uncontrollable variability, such as differences in equipment or environmental conditions. These principles are particularly useful in fields such as food technology, where blocking can isolate variations in raw material quality, or in automotive testing, where it can account for variability between different vehicle models.

By combining these principles with its ability to identify optimal factor-response relationships, DoE proves invaluable across a wide range of applications. From improving manufacturing processes to enhancing agricultural productivity, DoE remains a cornerstone of experimental research, offering actionable insights and facilitating performance optimization in diverse fields.

1.1.1.1 Taguchi Design (TD)

The Taguchi technique has become a widely recognized tool in the literature, particularly for structuring experiments, constructing models, and optimizing complex problems in multiple application areas [16,17]. The main reason why Taguchi is a highly preferred method is that it reduce the number of experiments that need to be done in the process of designing experiments and as a natural consequence of this, it reduces the cost, which stands out as the most important factor in all problems [18–20]. This efficiency is achieved using orthogonal arrays (OAs), which enable systematic evaluation of multiple factors with a smaller subset of trials. By strategically selecting combinations of factors and levels, Taguchi minimizes the experimental workload while still providing valuable insights into main effects and certain interactions. This makes it an attractive choice for fields like engineering, chemistry, biology, and social sciences, where experimental resources may be limited [21–23].

One of the significant advantages of the Taguchi method is its ability to drastically reduce experimental costs [24,25]. As an illustration, while a full factorial experiment involving eight variables at two levels each would require 256 separate trials, the Taguchi method can achieve comparable insights with as few as 12 experiments. However, this efficiency comes with certain limitations. The reduced number of experiments may fail to capture higher-order interactions or more subtle effects between factors, making the method less suitable for highly complex systems. Additionally, while the method is effective at identifying main effects, it may oversimplify systems where non-linear relationships play a significant role.

1.1.1.2 Box Behnken Design (BBD)

Box-Behnken Design (BBD) is widely regarded as an efficient and practical method for experimental studies involving three-level factors [26]. Unlike Central Composite Design (CCD), which requires axial points that may extend beyond the experimental space, BBD focuses on midpoints and center points, forming a spherical design [27]. This makes BBD particularly advantageous in scenarios where testing extreme factor levels is costly, impractical, or even unsafe [28].

A notable feature of BBD is its ability to create detailed response surface models while requiring fewer experiments than full factorial designs. However, this method does not include corner points in the factorial space, potentially overlooking critical information about the behavior of the system at extreme values. For processes where boundary conditions significantly impact the outcome, this exclusion can lead to incomplete models. Despite this, BBD remains an excellent choice for optimization studies, particularly in controlled environments such as pharmaceutical research and food processing, where middle-range factor levels are of primary interest [29].

1.1.1.3 Factorial Design (FD)

Factorial Design is recognized as one of the most comprehensive experimental approaches, offering a complete evaluation of all possible combinations of factor levels. This makes it ideal for understanding both main effects and interactions in detail. A full factorial design ensures that every level of each factor is tested against all other levels, providing balanced and statistically robust data [30,31].

While factorial design is unmatched in its ability to provide thorough insights, it becomes increasingly impractical as the number of factors grows. For instance, a two-level factorial design for five factors requires 32 experiments, but adding just two more factors raises this to 128. The rapid growth in required trials often makes factorial design unsuitable for complex systems or resource-constrained settings. As a result, it is typically reserved for systems with a limited number of factors or preliminary studies aimed at identifying the most influential variables.

1.1.1.4 Central Composite Design (CCD)

Central Composite Design (CCD) is a highly versatile method within response surface methodology, enabling researchers to develop detailed quadratic models for multi-factorial systems [32]. CCD combines factorial points, axial points, and center points to capture both linear and quadratic effects. This structure allows researchers to model curvature in the response surface, making CCD particularly effective for studying non-linear systems [33].

For systems with "k" factors, CCD requires 2^k factorial points, $2k$ axial points, and at least one center point. Achieving this balance enables a more detailed evaluation of factor interdependencies and contributes to building robust and accurate models for prediction. However, the inclusion of axial points, which extend beyond the factorial space, can pose challenges. These points may fall outside the feasible range of the experimental system, complicating implementation. Additionally, CCD can be resource-intensive for systems with many factors, requiring a substantial number of experiments. Despite these limitations, CCD is widely used in material science and engineering for optimizing processes involving complex interactions [34].

1.1.1.5 One Variable at a Time (OVAT)

The One Variable at a Time (OVAT) method represents a basic yet straightforward experimental design strategy, where a single parameter is altered while all others remain fixed. This approach allows for clear interpretation of individual factor effects and is commonly used in introductory-level or exploratory research [35].

While OVAT has its merits in terms of simplicity, it is highly inefficient and limited in scope. The inability to account for interactions between factors makes it unsuitable for complex systems where variables influence each other. For instance, in multi-factorial systems, OVAT fails to reveal combined effects or dependencies between factors, potentially leading to incomplete or misleading conclusions [36]. Consequently, OVAT is rarely used in advanced research but may still serve as a useful starting point for identifying critical factors in a process [37].

1.1.1.6 D-Optimal Design

D-Optimal Design represents a more advanced and flexible approach to experimental design. Unlike fixed designs such as CCD or BBD, D-Optimal Design uses optimization algorithms to tailor experimental sets to the specific requirements of a system. This method is particularly advantageous for systems with mixed numerical and categorical factors or when certain factor combinations must be excluded due to feasibility or safety constraints [38].

The key strength of D-Optimal Design lies in its adaptability. Researchers can define constraints, adjust factor levels, and prioritize interactions of interest, creating an experimental set that maximizes the efficiency of data collection. However, the reliance on computational algorithms can make D-Optimal Design resource-intensive, especially for systems with many factors or complex constraints. Additionally, the results of D-Optimal Design may vary between runs, which could introduce inconsistencies if the optimization process is not carefully controlled. Despite these challenges, D-Optimal Design is widely used in fields like biotechnology and drug development, where tailored experimental sets are essential for addressing specific research questions [39].

1.1.1.7 Comparison of Experimental Design Methods

Experimental design methods differ in their efficiency, ability to capture interactions, and suitability for various applications. Taguchi Design is highly efficient, making it ideal for cost-sensitive and time-constrained studies. However, its simplicity limits its ability to capture higher-order interactions, making it less suitable for complex systems. Similarly, Box-Behnken Design (BBD) is efficient for three-level systems and avoids extreme conditions, but it may miss critical boundary effects, restricting its use in systems where extremes significantly impact results [40].

For more detailed modeling, Central Composite Design (CCD) captures both linear and quadratic effects, making it effective for complex systems requiring response surface models [40]. However, its resource-intensive nature and the feasibility challenges of axial points can pose practical limitations. Factorial Design, on the other hand, provides the most comprehensive analysis by testing all factor combinations, capturing main effects and interactions. Yet, its exponential growth in trials with increasing factors makes it impractical for larger systems.

Simpler methods like One Variable at a Time (OVAT) are intuitive but inefficient, as they fail to account for factor interactions. In contrast, D-Optimal Design offers tailored experimental setups using computational algorithms, making it highly flexible for constrained systems with mixed factors. While this adaptability is invaluable, the computational demands and variability in outcomes may complicate its application [41].

Table 1.1 DOE Method Comparisons

Method	Efficiency (Trials)	Captures Interactions	Ideal Use Case	Limitations
Taguchi Design (TD)	Very High	Partial	Cost-sensitive and time - sensitive setups	Limited in detecting higher - order interactions, risk of oversimplified designs
Box-Behnken Design (BBD)	Moderate	Partial	Moderate numbers of factors (3–5), especially 3-level systems	Excludes extreme boundary points, which may impact output when boundary effects are critical
Central Composite Design (CCD)	Moderate	Comprehensive	Complex systems requiring quadratic models	Can be expensive for systems with many factors; axial points may not always be practical
Factorial Design (FD)	Moderate to High	Comprehensive (full factorial)	Systems with a small number of factors	Rapidly becomes unfeasible as the number of factors and levels increases
One Variable at a Time (OVAT)	Low to Moderate	None (single - factor only)	Very simple systems without factor interactions	Cannot evaluate factor interactions; highly inefficient for multi-factorial systems
D-Optimal Design	Very Low	Partial to Comprehensive	Systems with mixed factor types (numerical / categorical) and constraints	Results vary per run due to optimization; can be computationally intensive for large systems

In summary, selecting the optimal method depends on the system's complexity, resource constraints, and study objectives. Taguchi and BBD are suited for quick and cost-effective studies, while CCD and Factorial Design cater to detailed analyses. OVAT serves as a preliminary tool for identifying key variables, and D-Optimal is best for highly customized experimental setups. Table 1.1 explain of the key characteristics of these models [42].

1.1.2 Mathematical Modelling

As the second component of the DoE–Modeling–Optimization process, mathematical modeling focuses on establishing functional relationships between process variables and their outcomes using quantitative methods. This stage relies on the data obtained from experimental designs, which are based on carefully selected factors and their level values. Selecting a suitable experimental design method is essential for obtaining high-quality data, as it directly affects the accuracy and reliability of the resulting model.

During the modeling stage, a range of mathematical expressions—such as linear, polynomial, logarithmic, trigonometric, exponential, rational, hybrid, and other specialized functions—can be employed to characterize the connection between inputs and outputs [43]. The selection of a specific function type is guided by the system's inherent behavior and the complexity of the parameter interactions. The choice of model depends on the complexity and nature of the relationships present in the system. While linear or polynomial models may suffice for simpler systems, more intricate systems often require hybrid or non-linear functions to accurately capture interactions and system behavior. Regardless of the function used, mathematical modeling bridges experimental data with predictive capabilities, providing a foundation for system optimization [44].

In addition to traditional mathematical functions, modern literature introduces a wide range of advanced methods and approaches for modeling. Techniques such as Artificial Neural Networks (ANNs), Response Surface Methods (RSM), Support Vector Machines (SVM), Support Vector Regression (SVR), Decision Trees, Regression, Fuzzy Logic, and the Adaptive Neural Fuzzy Inference System (ANFIS) are widely used [45]. These approaches are widely adopted due to their flexibility in capturing input-output relationships across diverse datasets, irrespective of data distribution characteristics or prior model constraints. Their ability to adapt to non-linear and complex relationships makes them particularly useful in modern research and industrial applications.

Nonetheless, it is important to recognize that mathematical modeling is inherently interconnected with other stages of analysis. Its value goes beyond merely achieving high predictive accuracy. Instead, the effectiveness of modeling lies in its ability to provide insights into the system, improve understanding of parameter relationships, and serve as a reliable foundation for subsequent optimization efforts. A well-constructed model should strike a balance between accuracy, generalizability, and practical application, enabling researchers to predict responses under varying conditions and guide decision-making for system improvement.

By leveraging both classical mathematical approaches and advanced computational methods, the modeling phase serves as a powerful tool for connecting experimental data with real-world applications. This stage ensures that the insights gained from experimental studies are translated into actionable knowledge, forming a critical link in the process optimization framework.

1.1.2.1 Neuro Regression Method (NRM)

The Neuro Regression Method (NRM) integrates the strengths of traditional regression techniques with the dynamic learning capabilities of artificial neural networks, offering improved accuracy during the mathematical modeling stage [46]. Unlike traditional ANN, where the model structure is determined through training, NRM allows the user to propose specific mathematical models, leveraging the least-squares method to determine model coefficients. This user-defined flexibility is a key distinguishing feature of NRM, offering a balance between computational efficiency and interpretability.

NRM typically involves dividing the dataset, commonly used in artificial intelligence applications, into three parts: training, testing, and validation [47]. In the training stage, typically involving around 80% of the dataset, the model is developed by enabling the algorithm to capture both the mathematical structure and the physical behavior of the system. The training data comprises both inputs and outputs, enabling the model to capture the intrinsic relationships between parameters.

The testing phase, conducted after model training, is designed to evaluate how effectively the model applies learned knowledge to unfamiliar data, thus confirming its ability to generalize beyond the training set. This stage is critical for distinguishing between models that generalize well and those prone to overfitting. Lastly, the validation phase subjects the model to an additional evaluation using a smaller subset of data. This phase confirms the reliability and robustness of the model under conditions like real-world applications [48].

The NRM approach effectively bridges the gap between conventional regression methods and artificial intelligence techniques, providing a flexible yet structured framework for developing mathematical models. By combining user-defined mathematical formulations with the learning capabilities of ANN, NRM achieves a balance of accuracy, interpretability, and adaptability, making it a valuable tool for modeling complex systems [49].

1.1.3 Optimization Methods

Mathematical modeling, which serves as the second phase in the structured DOE-based optimization strategy, aims to translate input-output interactions into mathematical expressions that can be analyzed and simulated computationally. This stage relies on the data obtained from experimental designs, which are based on carefully selected factors and their level values. The appropriate choice of experimental design method plays a critical role in generating meaningful data for building reliable models, as the success of this stage is directly linked to the quality of the experimental setup.

Optimization processes often involve various computational tools and algorithms to address linear, nonlinear, constrained, and unconstrained problems [50]. Mathematica is one of the primary software tools utilized for such tasks, offering commands such as NMinimize and NMaximize for global numerical optimization, Minimize and Maximize for analytical global optimization, and FindMinimum and FindMaximum for local numerical optimization. These commands, supported by robust algorithms, provide solutions to a wide range of optimization challenges. Additionally, other platforms such as MATLAB, Python (with libraries like SciPy and Pyomo), and R serve as complementary tools, offering specialized libraries and algorithms for optimization problems of varying complexities.

Global optimization techniques frequently rely on heuristic and metaheuristic algorithms to explore non-convex and complex solution spaces. Differential Evolution (DE), for example, is a widely used method that improves candidate solutions through iterative steps such as mutation, crossover, and selection [51]. Its derivative-free nature makes it particularly suitable for non-differentiable or noisy objective functions [52]. Simulated Annealing (SA), inspired by the annealing process in metallurgy, uses stochastic exploration, occasionally allowing uphill moves to escape local optima [53,54]. This feature makes SA highly effective for problems with many local minima, though it requires careful parameter tuning, such as the cooling schedule.

Nelder-Mead (NM) is another widely adopted algorithm, particularly for local optimization of nonlinear functions [55]. Unlike gradient-based approaches, it evaluates function values at simplex vertices and adapts these vertices iteratively to navigate the solution space [56]. While NM performs well for smooth and continuous functions, it may encounter challenges in handling high-dimensional or noisy problems. Random Search (RS), on the other hand, offers a straightforward approach by sampling the solution space randomly. Although less sophisticated, RS is often a useful exploratory method, particularly when little is known about the structure of the search space [57,58].

Optimization techniques can generally be categorized as local or global, with the choice of method depending on the characteristics of the problem. By employing the gradient information of the target function, these methods effectively navigate smooth optimization surfaces, making them well-suited for solving local optimization problems. In contrast, direct search methods, such as Simulated Annealing and Random Search, operate independently of derivatives, making them better suited for non-convex or non-differentiable problems.

The integration of these algorithms into software tools like Mathematica, MATLAB, and Python allows for flexible and precise optimization across various fields. For example, Differential Evolution, Simulated Annealing, and Random Search can be implemented in Mathematica using commands like NMinimize and NMaximize, while Nelder-Mead is supported via FindMinimum. MATLAB and Python also offer robust implementations of these methods, enabling users to select the platform and algorithm best suited to their problem. This range of options ensures that a wide variety of optimization challenges can be addressed effectively.

Overall, heuristic, gradient-based, and probabilistic methods provide a versatile framework for solving problems of different complexities. Differential Evolution and Simulated Annealing excel in global optimization tasks, while Nelder-Mead and gradient-based approaches are more suitable for local optimization. Random Search offers a simple and adaptable method for preliminary exploration of poorly understood solution spaces. Together, these methods and tools form a robust foundation for achieving accurate and efficient optimization results.

1.2 Introduction to Additive Manufacturing

Additive manufacturing, also known as 3D printing, is a cutting-edge production method and a key player in advanced manufacturing technologies. The technique enables additive manufacturing of complex parts by incrementally building up layers from diverse feedstocks, including wire and powder forms, thus supporting rapid prototyping applications [59]. It transforms digital 3D CAD models directly into physical objects, bypassing many traditional manufacturing constraints [60]. Additive manufacturing boasts significant advantages such as faster production times compared to traditional methods, the capability to produce parts with complex geometries, and reduced material waste [61].

On a global scale, the ASTM International F42 Committee on Additive Manufacturing Technologies, established in 2009, plays a critical role in standardizing and advancing additive manufacturing. Meeting biannually, the committee focuses on developing technical standards that encompass all aspects of this transformative technology [62]. Currently consisting of over 725 members, the committee oversees eight technical subcommittees. Their published standards, compiled in the ASTM Standards Book (Volume 10.04), provide a foundation for ensuring quality and consistency in additive manufacturing processes. These standards are indispensable for industries adopting additive technologies, offering structured guidelines and a shared understanding of the methodologies and applications involved [63].

The F42 Committee defines additive manufacturing as "a method that uses computer-aided design to build objects layer by layer." This definition encompasses a wide range of materials, including metals, ceramics, polymers, composites, and biological systems [64]. This method is not limited to prototyping; it is increasingly applied in manufacturing high-performance parts in critical industries like aerospace, biomedical, and defense. As an advanced fabrication approach, metal additive manufacturing has introduced groundbreaking changes to modern manufacturing processes. With its ability to produce intricate parts such as jet engine components, turbine blades, and rotary wing systems, it significantly reduces the buy-to-fly ratio—a critical metric in aviation, measuring the amount of raw material transformed into flight-ready parts [65].

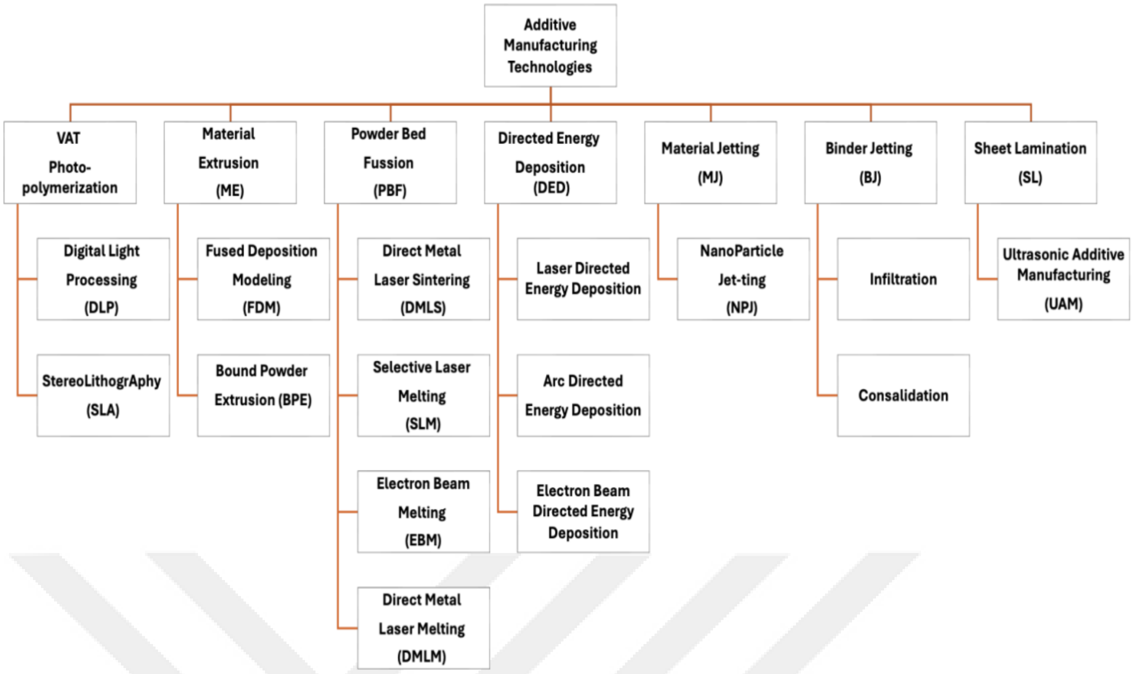

Figure 1.1 Additive Manufacturing Technologies

Additive manufacturing technologies are categorized into seven main types by the ASTM F42 Committee (Figure 1.1), with four methods specifically applicable to metals: Powder Bed Fusion (PBF), Direct Energy Deposition (DED), Binder Jetting, and Sheet Lamination. The remaining three—Material Extrusion, Material Jetting, and Vat Photopolymerization—primarily cater to non-metal applications [66]. Among the metal-focused techniques, DED and PBF are widely favored due to their ability to handle larger material volumes and produce parts with high precision and strength. Each method, however, carries unique advantages and limitations. For instance, PBF excels in producing highly detailed parts with excellent surface finish, while DED is ideal for creating larger components and repairing existing ones [67,68].

The progressive development of additive manufacturing has broadened its scope of application across sectors, facilitating the production of geometries and features that were traditionally infeasible. Moreover, it contributes to time and cost efficiency while fostering sustainable and flexible design practices. Its ability to handle high-cost raw materials, coupled with advancements in metal additive manufacturing, positions it as a transformative force in modern production landscapes.

1.2.1 Metal Additive Manufacturing

Metal Additive Manufacturing (AM) has established itself as a game-changing innovation in contemporary manufacturing, offering the capability to fabricate geometrically intricate and highly precise components that conventional techniques often struggle to realize. Its impact is especially pronounced in sectors like aerospace, defense, and energy, where the demand for lightweight and performance-critical parts is paramount. One of the distinctive benefits of metal AM is its ability to enhance material utilization efficiency—most notably reflected in the improvement of the "buy-to-fly" ratio, a crucial metric in aerospace that evaluates the effectiveness of raw material consumption. Unlike traditional methods that often result in significant material waste, metal AM minimizes this inefficiency, leading to substantial cost savings and greater sustainability [66,69].

Despite its potential, the adoption of metal AM in aerospace has been slower than anticipated. While polymeric materials have already started being used in additive manufacturing for Class 3 aerospace components, the integration of metal AM is still in its experimental phase. Companies like GE and Airbus are exploring the use of metal AM, but widespread application remains limited. One of the primary obstacles is the lack of standardized quality in production. Ensuring that parts meet strict aerospace standards consistently and reliably remains a significant challenge. Additionally, the qualification processes for AM-produced parts are lengthy and resource-intensive, further delaying the technology's broader adoption in high-performance industries [65,70].

In prototype aircraft production, where tooling costs are exceptionally high, additive manufacturing offers a compelling alternative. By removing the necessity for specialized tooling and significantly shortening production timelines, metal additive manufacturing offers a more economical and streamlined approach to part fabrication [71]. These features make it particularly advantageous for producing complex geometries in limited quantities. However, in large-scale manufacturing, traditional methods continue to dominate due to the limitations of AM, such as slower production speeds and constraints on the size of parts that can be produced. These factors, combined with the relatively high costs of AM equipment and materials, have restricted its use in mass production scenarios.

Metal additive manufacturing comprises a range of process types designed for specific materials and industrial needs. Among them, Powder Bed Fusion (PBF) and Direct Energy Deposition (DED) stand out for their widespread use. PBF is especially noted for producing intricate parts with high dimensional accuracy and refined surface quality, making it ideal for precision-driven applications [76,77]. Other methods, such as Binder Jetting and Sheet Lamination, offer unique capabilities but are generally less widely used in high-performance sectors like aerospace [78].

The potential of metal AM extends beyond its current applications, promising to revolutionize manufacturing by reducing material waste, enhancing design freedom, and enabling more sustainable production practices. However, its widespread adoption depends on overcoming key challenges, including the development of standardized processes and the completion of rigorous qualification procedures for aerospace components. As research and development efforts continue, metal AM is expected to expand its role in both prototyping and serial production, ultimately transforming how parts are designed and manufactured across industries.

1.2.1 Post-Processes in AM

In additive manufacturing, post-processes or secondary processes are crucial for addressing challenges such as high residual stress, poor surface quality, and porosity, which can negatively impact the mechanical performance of components. These processes are particularly vital in high-performance industries like aerospace, where both static and dynamic load behaviors are critical [79]. To optimize properties such as surface quality, porosity levels, and residual stress, secondary processes are applied and can be broadly classified into chemical, mechanical, and thermal methods [80–82].

Chemical methods, including chemical polishing, electro-polishing, and plasma polishing, are employed to improve surface finish and reduce imperfections that may lead to crack initiation. Mechanical methods, such as grinding, machining, and abrasive flow machining (AFM), focus on reducing surface roughness and eliminating defects, while thermal processes like laser polishing and electron beam irradiation modify surface characteristics and relieve residual stresses by controlled melting and re-solidification. Figure 1.2 illustrates these secondary process methods and their various subtypes, each targeting specific manufacturing challenges [83].

In the aerospace industry, these processes are essential for meeting stringent material performance requirements. Components produced via additive manufacturing must exhibit consistent quality, minimal porosity, and superior fatigue resistance. Post-processing techniques are essential for attaining the desired material properties, enabling the fabrication of dependable parts for high-demand applications like structural frameworks and engine components. By integrating these techniques into the manufacturing workflow, the functional properties of parts are significantly enhanced, contributing to their overall reliability and safety.

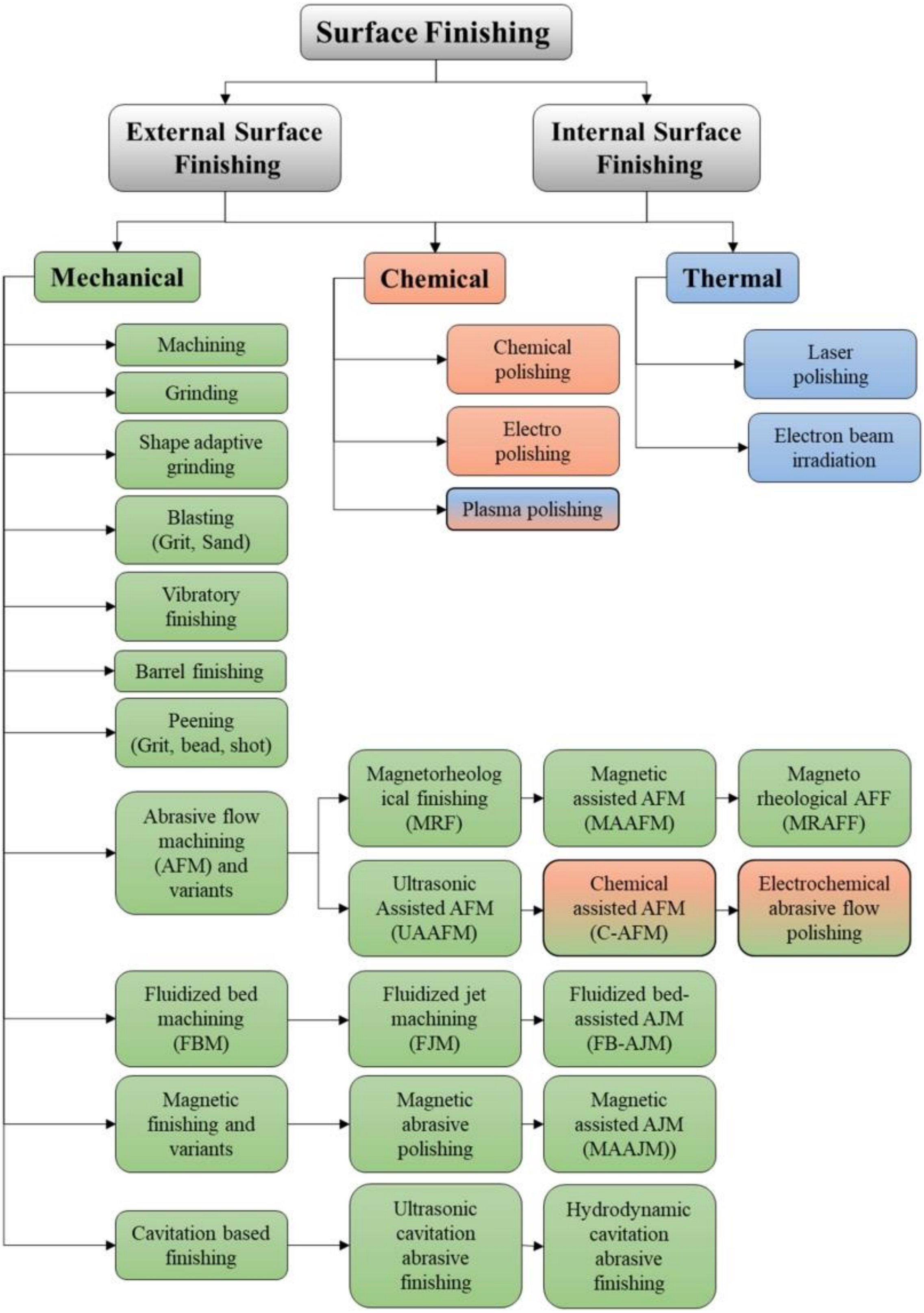

Figure 1.2 Secondary Process Methods

Several studies underline the importance of secondary processes in improving mechanical performance [84–89]. For example, Shui et al. (2017) investigated the impact of hot isostatic pressing (HIP) and heat treatment (HT) on Ti-6Al-4V alloys produced via the electron beam melting (EBM) method. Results revealed that HIP notably extended fatigue life, reaching up to 25 times that of untreated samples, primarily through porosity reduction. Yet, the microstructure changes observed did not entirely justify the magnitude of this improvement [90].

Maamoun et al. (2018) demonstrated the effectiveness of shot peening (SP) on AlSi10Mg alloys produced by selective laser melting (SLM). The application of SP led to surface densification, microstructural refinement, and stress-induced strengthening, which altogether enhanced the component’s mechanical behavior. While low-intensity SP yielded better surface finish, high-intensity SP provided greater depth of compressive stresses, highlighting the trade-offs between surface quality and performance [91].

Similarly, Wagner and Mueller (1992) investigated the effects of shot peening on Al 2024 alloys under different aging conditions. They found that shot peening improved high-cycle fatigue performance, particularly in underaged (T3) conditions, due to higher residual compressive stresses. The study emphasized the importance of combining shot peening with surface finishing techniques, such as polishing, to achieve maximum fatigue strength [92].

Uzan et al. (2018) further explored shot peening's effect on fatigue performance in AlSi10Mg specimens produced by SLM. Shot peening with steel or ceramic balls significantly enhanced fatigue resistance by introducing compressive stresses, effectively blocking crack initiation and propagation. Other processes, such as machining and polishing, showed only marginal improvements, reaffirming shot peening's unique advantages [93].

Overall, the results highlight the essential contribution of post-processing treatments in improving the mechanical behavior of parts produced via additive manufacturing. Methods such as Hot Isostatic Pressing (HIP), Shot Peening (SP), and surface polishing help mitigate common issues including porosity, surface irregularities, and residual stresses. These improvements are particularly vital for meeting the stringent reliability and performance criteria of critical sectors like aerospace.

1.3 Introduction to Hydrogen Embrittlement

The presence of hydrogen in the microstructure of metals can lead to hydrogen embrittlement (HE), a phenomenon that compromises mechanical integrity by severely reducing properties like ductility, toughness, and resistance to fracture [94]. This issue is especially critical for high-strength steels, titanium alloys, and other advanced materials that are often employed in structural applications. Due to its small atomic size and high diffusivity, hydrogen can infiltrate the metal's crystalline structure, compromising interatomic cohesion and inducing localized degradation. This degradation can ultimately cause premature failure, even when the applied stress is significantly lower than the material's yield strength. The susceptibility of materials to HE has been observed in various industries, from aerospace to energy, where structural reliability is crucial [95].

The scientific understanding of HE has evolved significantly, with several key studies providing insight into the mechanisms and influencing factors. For instance, Haiyang Yu et. al. (2019) [96] conducted simulations to explore the effects of hydrogen on dislocation mobility in body-centered cubic (bcc) materials. Their findings emphasized how hydrogen increases dislocation activity while simultaneously contributing to elastic shielding at crack tips. Similarly, Yejun Gu and El-Awady (2018) [97] developed a model that accounts for volume changes due to hydrogen diffusion, explaining the stress tensor variations caused by hydrogen interactions. These studies have advanced our understanding of how hydrogen facilitates crack initiation and propagation.

Further research into manufacturing methods has also revealed how microstructural differences affect hydrogen susceptibility. Michella Alnajjar et. al. (2020) [98] analyzed 17-4 PH steels produced via Selective Laser Melting (SLM) and found that the SLM process resulted in δ-ferritic microstructures with coarse grains, which made these steels more susceptible to hydrogen-induced damage compared to their wrought counterparts with martensitic structures. This highlights the critical role of manufacturing techniques and microstructural control in mitigating HE risks. In another study, Seung-Wook Baek et. al. (2017) [99] compared the effects of hydrogen on 304 stainless steels produced by Direct Metal Tooling (DMT) and rolling methods, finding that fine grain structures in DMT-produced samples exhibited better resistance to hydrogen embrittlement. The observations emphasize the necessity of examining how hydrogen influences materials with varying microstructural characteristics.

In the context of industrial applications, HE poses serious challenges in fields like aviation, where unexpected failures can have catastrophic consequences. Studies of aviation incidents have demonstrated that hydrogen introduced during manufacturing processes, such as electroplating, can remain trapped within components, leading to delayed cracking and failures. These observations have driven the development of stricter manufacturing controls, post-treatment methods like baking to release trapped hydrogen, and the use of hydrogen-resistant coatings [100–103].

1.3.1 Hydrogen Embrittlement Mechanisms

The phenomenon of hydrogen embrittlement is governed by a series of microstructural interactions wherein hydrogen alters material behavior, initiating distinct forms of mechanical failure. Despite extensive research, no single, universally accepted mechanism explains hydrogen embrittlement comprehensively, as the behavior of hydrogen varies significantly depending on the material, microstructure, and environmental conditions. Several mechanisms, such as Hydrogen-Enhanced Localized Plasticity (HELP), Hydrogen-Enhanced Decoherence (HEDE), and Hydrogen-Induced Phase Transformation (HIPT), have been proposed, each with distinct implications. Hydrogen-induced damage mechanisms are strongly affected by both the concentration of hydrogen, often quantified in ppm, and the intrinsic microstructure of the alloy. In some cases, hybrid mechanisms involving a combination of two or more processes have been observed, where interactions between localized plasticity and decohesion work together to accelerate crack propagation [104,105]. The observed differences point to the intricate mechanisms driving hydrogen embrittlement, emphasizing the importance of conducting focused studies tailored to individual material systems.

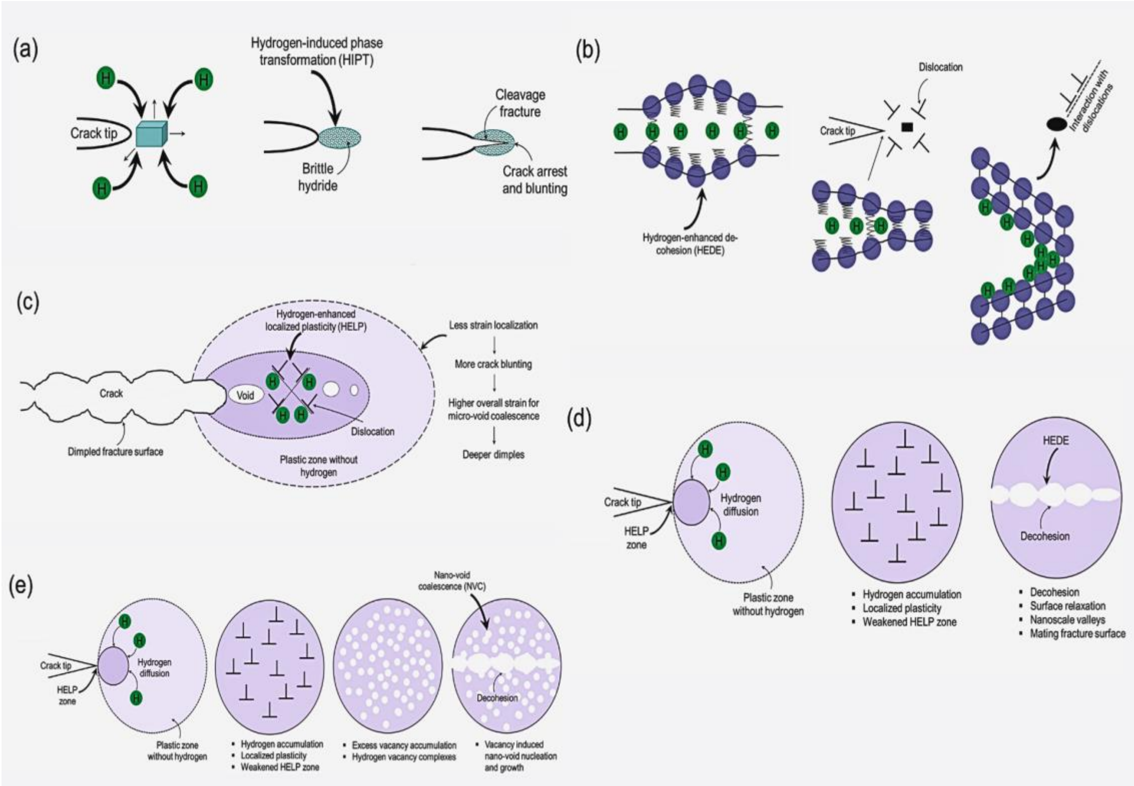

Figure 1.3 HE mechanisms' schematic diagrams, (a) HIPT; (b) HEDE; (c) HELP; (d) HEDE + HELP (e) NVC [106].

Hydrogen-Induced Phase Transformation (HIPT) is among the most examined mechanisms, wherein hydrogen accumulation promotes hydride formation near crack tips, ultimately triggering brittle cleavage failure [107]. This transformation is particularly relevant for metals like titanium, where hydrogen can form stable hydrides under stress, as depicted in Figure 1.3 (a). These phase changes create embrittled zones that serve as initiation sites for cracks, dramatically reducing the metal's ability to sustain loads [108].

Another critical mechanism is Hydrogen-Enhanced Decoherence (HEDE), where hydrogen weakens the atomic bonds within the metal lattice, promoting brittle cleavage fractures. This mechanism is particularly significant in titanium alloys and other high-strength metals exposed to hydrogen-rich environments [109,110]. As shown in Figure b of the provided visual, HEDE explains how interatomic decohesion facilitates crack propagation under stress.

A third mechanism, Hydrogen-Enhanced Localized Plasticity (HELP), which describes how hydrogen reduces the stress required for dislocation movement. By facilitating localized plastic deformation at crack tips, HELP accelerates crack growth while reducing the overall energy required for fracture [96,111]. The visual representation in Figure 1.3 (c) illustrates the development of a plastic zone enriched with hydrogen near the crack tip, highlighting the material's vulnerability to micro-void coalescence and subsequent crack propagation. This mechanism has been observed in studies focusing on dislocation-hydrogen interactions, such as those by Gu and El-Awady [97].

The combined effect of Hydrogen-Enhanced Decoherence (HEDE) and Hydrogen-Enhanced Localized Plasticity (HELP) represents a well-established synergistic mechanism, where these two processes act together to promote embrittlement. As shown in Figure 1.3 (d), HELP facilitates dislocation movement, increasing plasticity and enabling hydrogen to diffuse into high-stress zones, creating favorable conditions for the HEDE mechanism. In turn, HEDE weakens interatomic bonds, leading to brittle fracture and rapid crack propagation. This interplay is critically influenced by hydrogen concentration. At lower hydrogen levels, HELP-induced plasticity dominates the fracture process by localizing strain, whereas at higher hydrogen concentrations, HEDE becomes the prevailing mechanism, resulting in sudden and catastrophic failure [110]. The unified HELP+HEDE model, originally proposed by Milos B. Djukic et. al. [112], highlights this dynamic transition between mechanisms, demonstrating that the predominance of one over the other is determined by local and global hydrogen concentrations. The model also accounts for cases where HELP activity may not be a prerequisite for HEDE, particularly at high hydrogen levels ("non-HELP mediated decohesion") [113,114]. Recent studies, such as those by Lee et. al. [115], has expanded on the HELP+HEDE model by exploring its application to fatigue mechanisms and incorporating advanced theoretical frameworks such as Unified Mechanics Theory (UMT) proposed by Prof. Cemal Basaran, providing deeper insights into the synergistic action of hydrogen embrittlement mechanisms. These findings underscore the critical need for managing hydrogen concentration and optimizing microstructure to mitigate embrittlement, especially in materials like additively manufactured (AM) metals, where defects such as porosity and heterogeneous grain structures amplify HELP+HEDE interactions [104,116,117].

Additionally, Nano-Void Coalescence (NVC) is another mechanism through which hydrogen embrittlement manifests. As hydrogen diffuses into microstructural voids, it accumulates and promotes the formation of nano-voids that eventually coalesce into larger cracks. This phenomenon is particularly evident in materials with high defect densities or porous microstructures, such as those produced by SLM. Figure 1.3 (e) of the visual highlights this process, showing how void coalescence progresses to full-scale fracture under stress [118].

The interplay of these mechanisms varies depending on material composition, microstructure, and environmental factors, emphasizing the need for tailored approaches to mitigate hydrogen embrittlement in different applications. Understanding these mechanisms is crucial for developing advanced materials and manufacturing techniques that minimize the risks associated with hydrogen exposure.

1.3.1 Hydrogen Embrittlement Testing Methods

Hydrogen embrittlement (HE) testing methods are essential for evaluating the effects of hydrogen on material performance, particularly its impact on mechanical properties. These methods typically involve either electrochemical or gaseous hydrogen charging to introduce hydrogen into the material. Electrochemical hydrogen charging is conducted by immersing the specimen in a hydrogen-rich aqueous solution, such as sulfuric acid, and applying a cathodic current to facilitate hydrogen absorption. This method allows precise control over hydrogen concentration and is commonly used to study hydrogen diffusion, trapping, and its influence on material ductility and tensile strength [119]. However, its ability to simulate the full spectrum of hydrogen interaction scenarios observed in actual service conditions remains limited.

Gaseous hydrogen charging, on the other hand, involves exposing the material to high-pressure hydrogen gas [120]. This method can be performed in situ, where mechanical loading occurs simultaneously with hydrogen exposure, or ex situ, where the material is pre-charged with hydrogen and then tested under ambient conditions. While in situ testing closely mimics real-world applications, ex situ testing allows more controlled conditions but may suffer from hydrogen loss during testing.

To understand the mechanical impact of hydrogen, various tests are employed. Tensile testing evaluates the reduction in ductility and strength caused by hydrogen, while slow strain rate testing (SSRT) examines material behavior under low deformation rates to highlight hydrogen-induced brittleness [121,122]. Fatigue crack growth rate (FCGR) testing measures crack propagation under cyclic loading in hydrogen environments, and fracture toughness tests assess the material’s resistance to crack growth [120,123]. Additionally, hydrogen permeation and diffusion testing, such as thermal desorption analysis (TDA), quantify the ability of hydrogen to diffuse through or remain trapped within the material. Post-test analyses, such as scanning electron microscopy (SEM) and transmission electron microscopy (TEM), are often conducted to investigate fracture surfaces and microstructural changes, revealing evidence of hydrogen-induced damage mechanisms.

For additively manufactured (AM) metals, specialized testing approaches are increasingly customized to address their unique microstructures, such as porosity, residual stresses, and layered morphologies [104]. These customized approaches are designed to examine how hydrogen interacts with features unique to additive manufacturing, with particular attention to crack initiation and mechanisms like hydrogen-enhanced decohesion (HEDE) and localized plasticity (HELP). By adapting tests like slow strain rate testing (SSRT), fatigue crack growth rate (FCGR) analysis, and advanced microscopy techniques, these approaches provide precise insights into hydrogen embrittlement mechanisms. Overall, these customized testing strategies are critical for identifying hydrogen-material interactions and guiding the development of hydrogen-resistant materials for applications in hydrogen-rich environments.

Chapter 2

Comprehensive Optimization of Shot Peening Intensity Using a Hybrid Model with AI-Based Techniques via Almen Tests

Shot peening is a crucial surface treatment technique that significantly enhances the mechanical properties of metallic components, particularly their fatigue resistance and ability to withstand stress corrosion. This study focuses on optimizing the shot peening process within the aviation industry by evaluating and selecting the most effective mathematical models and optimization methods. Using a Neuro Regression Method (NRM), seven models were analyzed, with the Second-Order Trigonometric Nonlinear Model (SOTN) emerging as the most reliable, achieving R^2 values of 0.93 for training and 0.90 for testing datasets. To ensure robustness, the SOTN model was further tested using four optimization methods: Differential Evolution (DE), Simulated Annealing (SA), Nelder-Mead (NM), and Random Search (RS). Despite valuable insights, performance variability across the intensity spectrum led to the development of a hybrid optimization model that combined the strengths of all four methods. This hybrid model achieved an overall mean error percentage of approximately 10.93%, demonstrating superior capability in optimizing the shot peening process across a wide range of intensity targets. The findings enhance shot peening efficiency and contribute to the literature with a comprehensive approach to AI-based process optimization.

2.1 Introduction

Shot peening is a widely adopted surface enhancement technique known for its ability to boost fatigue performance and mitigate stress corrosion effects, especially in critical fields like aerospace, structural engineering, and automotive design [91,124–127]. The process entails subjecting a material's surface to high-velocity impacts by small particles, thereby inducing beneficial compressive residual stresses that enhance the material's mechanical performance [93,128].

Shot peening is widely recognized for its effectiveness yet optimizing key process parameters such as shot material, size, and intensity, remains essential for maximizing efficiency and meeting modern manufacturing demands [129]. Among these parameters, peening intensity is particularly crucial as it directly correlates with the kinetic energy transferred from the shots to the material surface, inducing plastic deformation and compressive residual stresses that enhance fatigue life [130]. The intensity (I), influenced by the shot's mass and velocity, can be precisely controlled through a logarithmic regression model ($\mathrm{I} = \mathrm{a}\ \ln(\Delta\mathrm{P})$), where velocity ($\mathrm{v}$) is proportional to the square root of the pressure drop (ΔP) across the system ($\mathrm{v} \propto \sqrt{\Delta\mathrm{P}}$) [131].

Engineers often rely on a logarithmic regression model to predict and optimize shot peening intensity, which is critical for enhancing the durability and performance of treated components [131,132]. The Almen test, introduced in 1963, serves as a standardized method to measure this intensity. Almen intensity is quantified by measuring the arc height of a peened SAE1070 steel strip, which bends under induced compressive stress. The saturation point is reached when successive peening cycles cause less than a 10% change in arc height [133]. SAE standards provide detailed procedures for this measurement, ensuring consistency and accuracy in process control, making the Almen test integral to various industries [134–138].

Coverage, another key parameter, represents the proportion of the treated surface area impacted by peening indentations, ensuring comprehensive treatment of the material. It, typically assessed visually, becomes challenging to measure accurately as it nears 100%, and 98% coverage is generally considered equivalent to full coverage according to industry standards [137]. Optimizing both intensity and coverage is vital to achieving the desired mechanical properties, with numerous studies demonstrating the importance of precise control over these parameters [139].

Numerous studies have been conducted to investigate the underlying mechanisms and effectiveness of the shot peening process in greater detail. Utilizing aluminum Al2024 test strips in L and T directions, and Almen test strips (SAE 1070 steel [135]), Miao *et al.* [140] established precise numerical relationships between peening time and variables such as saturation, surface coverage, and roughness. It was observed that the directional grain alignment in aluminum impacts shot peening effectiveness, with longitudinally rolled samples (L) exhibiting higher arc intensities than transverse (T) counterparts. The kinetics of surface coverage were accurately described by the Avrami model, $X(t) = 1 - \exp(-\mathrm{k}t^n)$, providing a high correlation with empirical data.

In another study, Wang *et al.* [141] focused on optimizing shot peening by testing various combinations of shot velocity, shot diameter, and coverage ratio to determine their influence on maximum compressive residual stress ($\sigma_{\max}^{\mathrm{RS}}$), the depth of compressive residual stress field (δ_0) and the stress concentration factor (K). They used response surface methodology (RSM) to optimize these parameters, finding that a shot velocity of 88 m/s, a shot diameter of 0.8 mm, and a coverage ratio of 170% for 42CrMo specimens resulted in a 104% increase in fatigue life.

Process optimization (PO) is crucial for maximizing efficiency in shot peening operations, but it should be integrated with the design of experiments (DOE) and mathematical modeling to ensure accurate results [5,50,142,143]. DOE is a powerful statistical method for optimizing processes, enabling the systematic exploration of multiple factors and their interactions [144,145]. By applying methods like D-Optimal, Taguchi, and Factorial designs, engineers can identify optimal process conditions that yield desired surface properties while optimizing resources and minimizing experimental runs [16,30,146–148].

Mathematical modeling (MM), the next stage in PO, defines the relationship between input and output parameters using models like linear, polynomial, and exponential functions [7,46,149]. This modeling is essential for deriving objective functions that guide the optimization process. Various optimization algorithms, including Differential Evolution (DE), Nelder-Mead (NM), Simulated Annealing (SA), and Random Search (RS), are then employed to find the optimal set of parameters [44,150]. Each method has strengths and is chosen based on the problem's complexity, available resources, and the desired accuracy of the optimization [53,151,152].

This study primarily aims to determine the optimal process parameters for a shot peening machine used in enhancing fatigue performance and mitigating hydrogen embrittlement, particularly in the aviation industry, under specific intensity and coverage criteria. Unlike traditional optimization approaches, this research focuses on identifying parameters that achieve the desired intensity level rather than minimizing or maximizing a cost function. By employing four optimization methods; Differential Evolution, Nelder-Mead, Random Search, and Simulated Annealing, the study identifies the method with the lowest error margin relative to the target intensity. The results are validated through incremental validation and Monte Carlo simulations, ensuring reliability and consistency. Additionally, seven different mathematical models are analyzed using neuro-regression, further optimizing the process. This comprehensive approach not only highlights the critical role of shot peening in production but also contributes to the literature on AI-based optimization, with significant implications for improving production efficiency within Turkish Aerospace Industries.

2.2 Experimental Procedure

The shot peening machine utilized in this study was the Wheelabrator MP 1000, known for its compliance with industry standards such as MIL-S 13165-C, MIL-S-851-D, and AMS 2431/1 (C). As outlined in Table 2.1, parameter values for air pressure, mass flow rate, impact angle, stand-off distance, and inverse feed rate were chosen in accordance with the upper and lower bounds of the shot peening system's capabilities.

Table 2.2 Shot Peening Process Parameters

Parameters	Units	Lower	Upper
Air Pressure	Bar	2	6
Mass Flow	Kilogram·Minutes^{-1}	1	8
Impact Angle	Degree	45	90
Distance Between Nozzle and Specimen	Centimeter	15	25
Inverse Feedrate	Minutes·Centimeter^{-1}	10	40

Steel VS170-MH shots, with a hardness range of 45–52 HRC, were selected for their proven quality, endorsed by industry leaders like Rolls Royce and British Aerospace. The nozzle was oriented both horizontally and at a 45-degree angle to evaluate directional impact effects. For simplicity, only normal impingement was considered, excluding interactions between individual shots to simplify the analysis.

Almen Strips, specifically Type A and Grade 1S (A-1S™) from Electronics Inc., made from SAE 1070 plain carbon steel, were used. These strips conform to standards like SAE AMS 2432 B and SAE J442, with hardness of 45–48 HRC and dimensions of 19 mm × 76 mm with a thickness of 1.30 mm. The chemical composition of the SAE 1070 material is shown in Table 2.2 Intensity values of the peened test strips were measured using a Model TSP-3 #2 Almen Gage, and coverage control was conducted using an optical microscope.

Table 2.3 Chemical Composition of SAE 1070/75 TR Carbon Steel (wt.%) [136]

C	S	Mn	P. Max	S. Max	Cr
0.70 - 0.80	**0.15 – 0.30**	**0.60 – 0.70**	**0.02**	**0.01**	**0.20**

Figure 2.1 illustrates the key steps involved in the shot peening process, with a focus on the testing and inspection phases. The process begins with the preparation of Almen test strips, which are placed in a shot peening machine for treatment. These strips are securely mounted on a specific tool to ensure stability during the procedure. As the machine operates, it bombards the strips with shot particles, inducing beneficial compressive stresses.

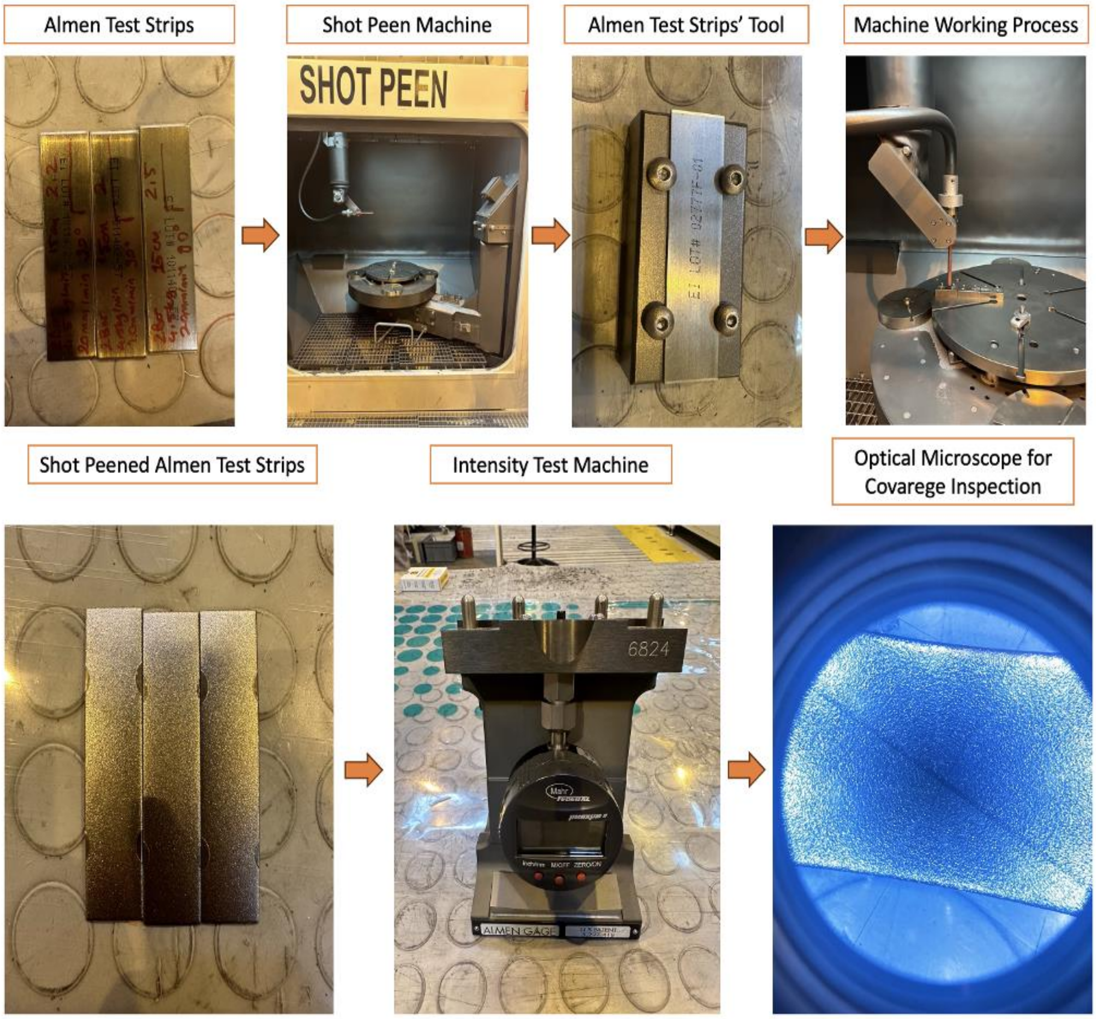

Figure 2.2 Shot Peening Process for Almen Test Strips

Following the shot peening process, the treated Almen test strips undergo intensity testing using a specialized machine that measures the arc height, serving as an indicator of the peening intensity. Subsequently, a coverage inspection is performed using an optical microscope to evaluate the uniformity and completeness of the shot peening on the strips. This inspection is critical for ensuring that the entire surface area has been effectively treated, which is essential for achieving the desired material properties. The sequence of steps shown in the Figure 2.1 is vital for validating and optimizing the shot peening process, ensuring consistent quality and performance in the treated components.

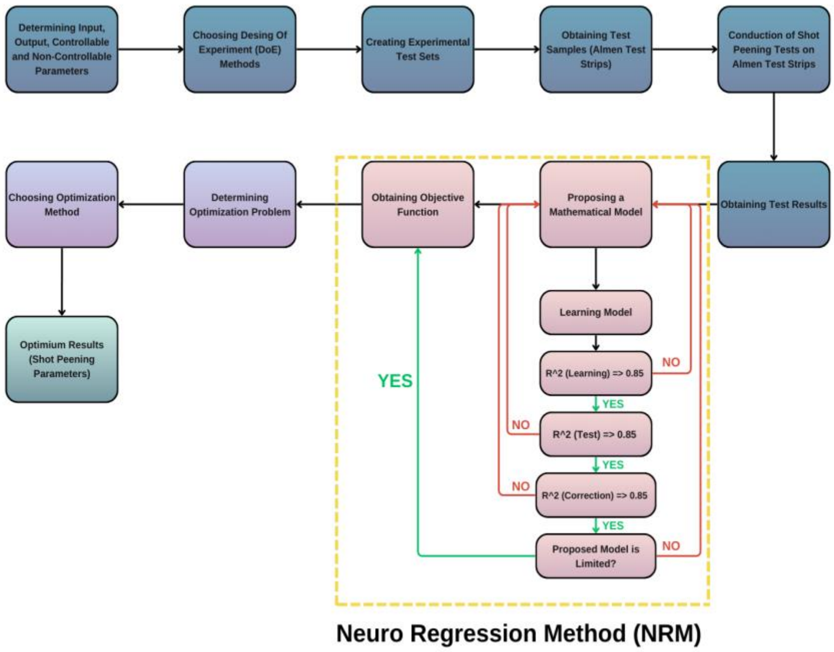

Figure 2.2 Process optimization flow chart of shot peening

As depicted in Figure 2.2, the optimization process for shot peening parameters begins with a precise definition of the objective function, design variables, and constraints. Unlike traditional methods, this study adopts a more advanced approach by employing the D-optimal design of experiments (DoE) to generate data. This method allows for the control and analysis of multiple parameter interactions, including Air Pressure, Mass Flow, Impact Angle, Distance Between the Nozzle and Specimen, and Inverse Feedrate. These data, obtained from 39 different experiments, are then used to develop and evaluate seven different linear and non-linear regression models to assess their predictive capabilities in capturing the physical phenomena associated with shot peening. To enhance accuracy, 18 additional experiments were conducted, bringing the total to 57 experiments, each repeated three times to ensure high consistency. Table 2.3 provides the mathematical expressions, associated nomenclature, and formulations of the linear and non-linear regression models examined in this study.

Table 2.4 Multiple regression model types

Model Name	Nomenclature	Formula
Multiple Linear	**L**	$f(x) = \alpha_0 + \sum_{i=1}^{5} (\alpha_i x_i)$
Multiple Linear Rational	**LR**	$f(x) = \frac{\alpha_0 + \sum_{i=1}^{5} (\alpha_i x_i)}{\beta_0 + \sum_{i=1}^{5} (\beta_i x_i)}$
Second Order Multiple Non-Linear	**SON**	$f(x) = \alpha_0 + \sum_{i=1}^{5} (\alpha_i x_i) + \sum_{i=1}^{5} (\alpha_{i+5} x_i^2) + \sum_{i=1}^{4} \sum_{j=i+1}^{5} (\alpha_{ij+9}\, x_i x_j)$
Third Order Multiple Non-Linear	**TON**	$f(x) = \alpha_0 + \sum_{i=1}^{5} (\alpha_i x_i) + \sum_{i=1}^{5} (\alpha_{i+5} x_i^2) + \sum_{i=1}^{4} \sum_{j=i+1}^{5} (\alpha_{10+ij}\, x_i x_j) + \sum_{i=1}^{5} (\alpha_{15+i} x_i^3) + \sum_{i=1}^{4} \sum_{j=i+1}^{5} (\alpha_{20+ij}\, x_i x_j^2) + \sum_{i=1}^{3} \sum_{j=i+1}^{4} \sum_{k=j+1}^{5} (\alpha_{25+ijk} x_i x_j x_k)$
First Order Trigonometric Multiple Non-Linear	**FOTN**	$f(x) = \alpha_0 + \sum_{i=1}^{5} \alpha_i\, sin(x_i) + \sum_{i=1}^{5} \alpha_{i+5}\, cos(x_i)$
Second Order Trigonometric Multiple Non-Linear	**SOTN**	$f(x) = \alpha_0 + \sum_{i=1}^{5} \alpha_i\, sin(x_i) + \sum_{i=1}^{5} \alpha_{i+5}\, cos(x_i) + \sum_{i=1}^{5} \alpha_{i+10} \sin^2(x_i) + \sum_{i=1}^{5} \alpha_{i+15} \cos^2(x_i)$
Second Order Exponential Nonlinear	**SOEN**	$f(x) = \alpha_0 + \sum_{i=1}^{5} \alpha_i e^{x_i} + \sum_{i=1}^{5} \alpha_{i+5} e^{2x_i}$

To achieve the most accurate mathematical model, the study employs a Neuro Regression Method (NRM), integrating machine learning with traditional regression. The data were divided into learning, testing, and validation sets, with the model refined until a coefficient of determination (R^2) value greater than 0.85 was achieved.

Upon model validation, optimization was performed using several algorithms, including Differential Evolution (DE), Simulated Annealing (SA), Nelder-Mead (NM), and Random Search (RS). These algorithms were implemented in Wolfram Mathematica, chosen for their effectiveness in process optimization. Each method was applied to determine the desired shot peening with optimal parameters, ensuring that the final model could predict optimal conditions accurately, leading to enhanced shot peening performance.

The performance of each model was quantitatively assessed through (R^2) (see Equation (2.1)) and model efficiency (ME) (see Equation (2.2)), ensuring a robust comparison with experimental observations. Furthermore, the established models facilitated the identification of boundary values within the operational limits of the test parameters.

$$R^2 = 1 - \frac{\sum_{i=1}^{n}\left(X_{A,i} - X_{P,i}\right)^2}{\sum_{i=1}^{n} X_{P,i}^2} \tag{2.1}$$

$$ME = 1 - \frac{\sum_{i=1}^{n}\left(X_{A,i} - X_{P,i}\right)^2}{\sum_{i=1}^{n}\left(X_{A,i} - \bar{X}_{P,i}\right)^2} \tag{2.2}$$

where, X_A represents actual data and X_P denotes predicted data.

In this study, instead of optimizing a traditional cost function, the focus was on identifying the process parameters that achieve the desired shot peening intensity as specified by the user. A hybrid optimization framework, integrating four distinct algorithms, Differential Evolution, Nelder-Mead, Random Search, and Simulated Annealing, was employed to navigate the multidimensional parameter space and systematically converge on the optimal set of parameters. The optimization results were subjected to rigorous validation protocols, including incremental validation and Monte Carlo simulations, to ensure robustness, reliability, and consistency of the derived solutions across varying operational conditions. This approach effectively balances exploration and exploitation within the optimization landscape, ensuring that the final model is both accurate and resilient.

2.3 Results and Discussions

In Table 2.4, candidate models along with their respective $R^2_{training}$, $R^2_{testing}$, $\mathrm{ME}_{\mathrm{learning}}$, $\mathrm{ME}_{\mathrm{testing}}$ and boundary values, which are used to define the shot peening intensity. A three-step control system was implemented in selecting the regression models developed for modeling the desired shot peening properties. This systematic approach required that $R^2_{training}$ values exceed 0.9, and the $R^2_{testing}$ values surpass 0.85, and that the statistical values be within acceptable limits. $ME_{learning}$ and $ME_{testing}$ are close to 1 are considered statistically valid. An evaluation of each model's output range was conducted by identifying its upper and lower prediction limits, thereby revealing potential boundary constraints. This method ensures that the predictions remain within a realistic and reliable range, thereby mitigating the risk of extreme outliers and enhancing the model's overall robustness.

Table 2.5 Results of neuro-regression models for shot peening almen test samples

Models	$\mathbf{R^2_{training}}$	$\mathbf{ME_{learning}}$	$\mathbf{R^2_{testing}}$	$\mathbf{ME_{testing}}$	**Min Intensity, 0.01 mmA**	**Max Intensity 0.01 mmA**
L	0.88	0.88	0.87	0.87	14.66	72.46
LR	0.94	0.94	0.88	0.88	16.46	75.05
SON	0.97	0.97	0.86	0.86	15.39	84.66
TON	0.99	0.99	0.78	0.78	13.99	81.57
FOTN	0.91	0.91	0.87	0.87	-43.35	85.86
SOTN	0.93	0.93	0.90	0.90	7.01	85.30
SOEN	0.92	0.92	0.87	0.87	-18746.30	77.22

In the mathematical model Equations (2.3)–(2.9) presented below, the variables x_1, x_2, x_3, x_4, and x_5 represent the following shot peening parameters: Air Pressure, Mass Flow, Impact Angle, Distance Between Nozzle and Specimen, and Inverse Feedrate, respectively.

Linear Model (L), as shown in Equation (2.3), demonstrates consistent performance across both training and testing datasets with R^2 and ME values of 0.88 and 0.87, respectively. However, the model does not push the physical limits, with a maximum predicted intensity value of 72.46, indicating a broad range of predictions.

$$f(x) = 1.4334 + 7.8843 \cdot x_1 - 0.1599 \cdot x_2 + 0.2853 \cdot x_3 - 0.0963 \cdot x_4 - 0.0833 \cdot x_5 \quad (2.3)$$

Logarithmic Regression Model (LR), as shown in Equation (2.4), performs well, with R^2 and ME values of 0.94 for the training data and 0.88 for the test data. The model predicts a minimum intensity of 16.46 mm and a maximum of 75.05 mm, indicating that it provides both acceptable performance metrics and physically meaningful intensity ranges.

$$f(x) = \frac{2524.4136 + 844.7950 \cdot x_1 - 145.1632 \cdot x_2 - 17.1118 \cdot x_3 + 4.7235 \cdot x_4 - 0.7505 \cdot x_5}{148.4690 + 5.3325 \cdot x_1 - 2.8906 \cdot x_2 - 1.04552 \cdot x_3 + 0.1705 \cdot x_4 + 0.0763 \cdot x_5} \quad (2.4)$$

Second-Order Nonlinear Model (SON), as shown in Equation (2.5), delivers the highest performance among all models, with R^2 and ME values of 0.97 for training data and 0.86 for test data. However, the model predicts a maximum intensity of 84.66 mm, which suggests the possibility of overestimation in some cases.

$$f(x) = 10.3222 - 0.5138 \cdot x_1 - 0.0342 \cdot x_1^2 - 0.2268 \cdot x_2 + 0.4560 \cdot x_1 \cdot x_2 - 0.0603 \cdot x_2^2 + 0.1090 \cdot x_3 + 0.0713 \cdot x_1 \cdot x_3 - 0.0072 \cdot x_2 \cdot x_3 + 0.0010 \cdot x_3^2 + 0.3255 \cdot x_4 + 0.1313 \cdot x_1 \cdot x_4 - 0.0369 \cdot x_2 \cdot x_4 - 0.0048 \cdot x_3 \cdot x_4 + 0.0083 \cdot x_4^2 + 0.3411 \cdot x_5 - 0.0579 \cdot x_1 \cdot x_5 + 0.0224 \cdot x_2 \cdot x_5 - 0.0031 \cdot x_3 \cdot x_5 - 0.0257 \cdot x_4 \cdot x_5 + 0.0088 \cdot x_5^2 \quad (2.5)$$

Third-Order Nonlinear Model (TON), as shown in Equation (2.6), achieves the highest R^2 and ME values at 0.99, but it experiences a significant drop in performance on test data, where these values fall to 0.78. The model's predictions range from 13.99 mm to 81.57 mm, indicating that it may be overfitting the training data and could lack generalization capability.

$$f(x) = 16.2010 - 4.0185 \cdot x_1 + 0.4620 \cdot x_1^2 - 0.04251 \cdot x_1^3 + 1.7092 \cdot x_2 - 0.4871 \cdot x_1 \cdot x_2 - 0.0261 \cdot x_2^2 + 0.0995 \cdot x_1 * x_2^2 - 0.0265 \cdot x_2^3 + 0.09407 \cdot x_3 + 0.0178 \cdot x_1 \cdot x_3 + 0.0039 \cdot x_2 \cdot x_3 + 0.0002 \cdot x_3^2 + 0.0007 \cdot x_1 \cdot x_3^2 - 0.0001 \cdot x_2 \cdot x_3^2 - 0.000004 \cdot x_3^3 + 0.4117 \cdot x_4 - 0.03003 \cdot x_1 \cdot x_4 + 0.0284 \cdot x_2 \cdot x_4 - 0.0006 \cdot x_3 \cdot x_4 + 0.0058 \cdot x_4^2 + 0.0038 \cdot x_1 *\cdot x_4^2 - 0.0005 \cdot x_2 \cdot x_4^2 - 0.0002 \cdot x_3 \cdot x_4^2 - 0.0001 \cdot x_4^3 - 0.2650 \cdot x_5 + 0.3932 \cdot x_1 \cdot x_5 - 0.1669 \cdot x_2 \cdot x_5 + 0.0041 \cdot x_3 \cdot x_5 + 0.0079 \cdot x_4 \cdot x_5 - 0.0036 \cdot x_5^2 - 0.0091 \cdot x_1 \cdot x_5^2 + 0.0043 \cdot x_2 \cdot x_5^2 - 0.0002 \cdot x_3 \cdot x_5^2 - 0.0009 \cdot x_4 \cdot x_5^2 + 0.0007 \cdot x_5^3 \tag{2.6}$$

First-Order Trigonometric Nonlinear Model (FOTN), as shown in Equation (2.7), produces physically impossible minimum predicted values, such as -43.35 mm, suggesting that this model poorly represents the real-world data. Although R^2 and ME values are 0.91 for training and 0.87 for test data, its wide prediction range and violation of physical limits make it unreliable.

$$f(x) = 20.2130 + 6.8816 \cdot \cos(x_1) + 4.0602 \cdot \cos(x_2) - 10.7344 \cdot \cos(x_3) + 7.8479 \cdot \cos(x_4) - 2.416 \cdot \cos(x_5) - 11.4482 \cdot \sin(x_1) - 1.7804 \cdot \sin(x_2) + 23.1152 \cdot \sin(x_3) + 18.1155 \cdot \sin(x_4) + 1.0365 \cdot \sin(x_5) \tag{2.7}$$

Second-Order Trigonometric Nonlinear Model (SOTN), as shown in Equation (2.8), shows solid performance with R^2 and ME values of 0.93 for training and 0.90 for test data. The model’s predictions are within physically meaningful limits, making it a generally reliable option

$$f(x) = 4.7663 + 7.6278 \cdot \cos(x_1) + 9.30397 \cdot \cos^2(x_1) - 0.7245 \cdot \cos(x_2) + 14.5213 \cdot \cos^2(x_2) - 12.8208 \cdot \cos(x_3) + 16.3463 \cdot \cos^2(x_3) + 2.1915 \cdot \cos(x_4) + 5.7425 \cdot \cos^2(x_4) - 0.5353 \cdot \cos(x_5) + 9.6163 \cdot \cos^2(x_5) - 10.7670 \cdot \sin(x_1) + 4.4591 \cdot \sin^2(x_1) - 1.1994 \cdot \sin(x_2) + 5.5716 \cdot \sin^2(x_2) + 5.5874 \cdot \sin(x_3) + 6.5318 \cdot \sin^2(x_3) + 3.6211 \cdot \sin(x_4) + 10.05801 \cdot \sin^2(x_4) + 0.83534 \cdot \sin(x_5) + 5.7615 \cdot \sin^2(x_5) \tag{2.8}$$

Exponential Model (SOEN), as shown in Equation (2.9), is problematic, producing an extremely unrealistic minimum intensity value of -18746.30 mm, which suggests that the model parameters were not stabilized, and the model is incompatible with the actual data.

$$f(x) = 24.9081 + 0.4152 \cdot \exp(x_1) - 0.0009 \cdot \exp(2x_1) + 0.0029 \cdot \exp(x_2) - 0.000001 \cdot \exp(2x_2) + 4.8083 \times 10^{-39} \cdot \exp(x_3) + 3.9399 \times 10^{-78} \cdot \exp(2x_3) - 3.5908 \times 10^{-12} \cdot \exp(x_4) - 5.0251 \times 10^{-23} \cdot \exp(2x_4) - 2.1066 \times 10^{-13} \cdot \exp(x_5) + 8.9496 \times 10^{-31} \cdot \exp(2x_5) \quad (2.9)$$

After evaluating all models, the Second-Order Trigonometric Nonlinear Model (SOTN) emerges as the most suitable choice. It performs well in terms of R^2 (0.93) and ME (0.93) values and provides physically plausible intensity predictions. The model maintains consistent performance across training and testing datasets and does not violate any physical boundaries in its predictions. Therefore, the SOTN model is selected as the most reliable and generally acceptable model for predicting the intensity of this specific physical phenomenon.

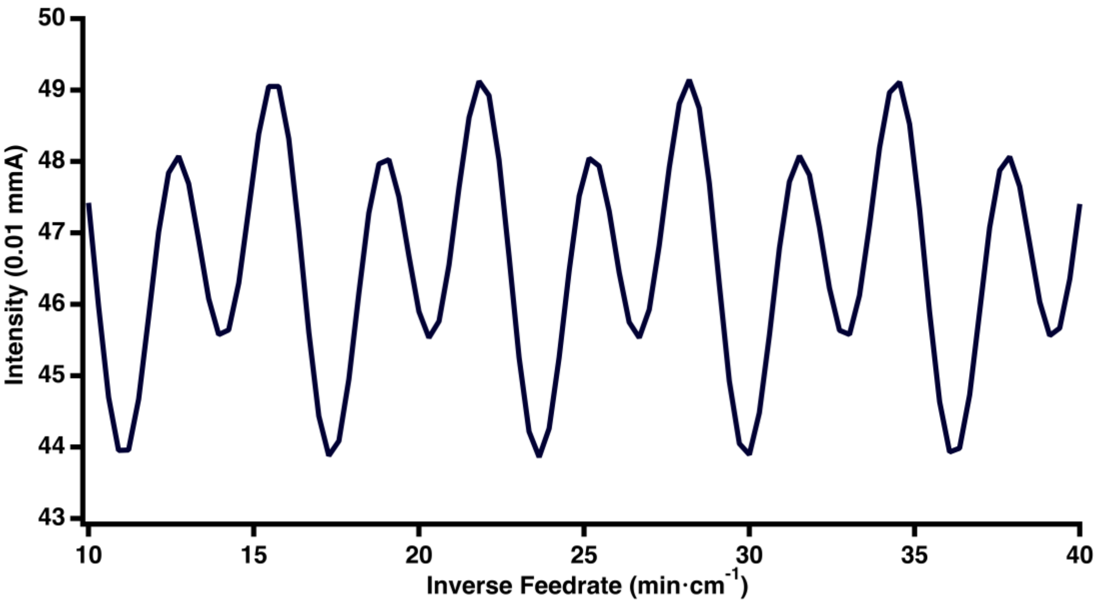

Figure 2.3 Intensity vs Inverse Feedrate for SOTN Model (Air Pressure=3 Bar, Mass Flow=4.5 kg·min-1, Impact Angle=90 Degree Distance Between Nozzle and Specimen =25 cm)

Figure 2.3 illustrates the relationship between peening intensity and inverse feed rate during the shot peening process. The graph reveals a periodic fluctuation in intensity as a function of inverse feed rate, indicating a dynamic interaction between feed rate and energy transfer. Slower feed rates (corresponding to higher inverse feed rates) result in increased amplitude of intensity oscillations, reflecting more pronounced energy deposition onto the material surface. The intensity values, which range between approximately $44*10^{-2}$ mmA and $49*10^{-2}$ mmA highlight the variability in energy absorbed by the surface, with higher intensities corresponding to more optimal energy transfer. The consistent frequency of these oscillations suggests a stable and repeatable process under the given conditions, emphasizing the critical role of feed rate control in achieving uniform and effective surface treatment through shot peening.

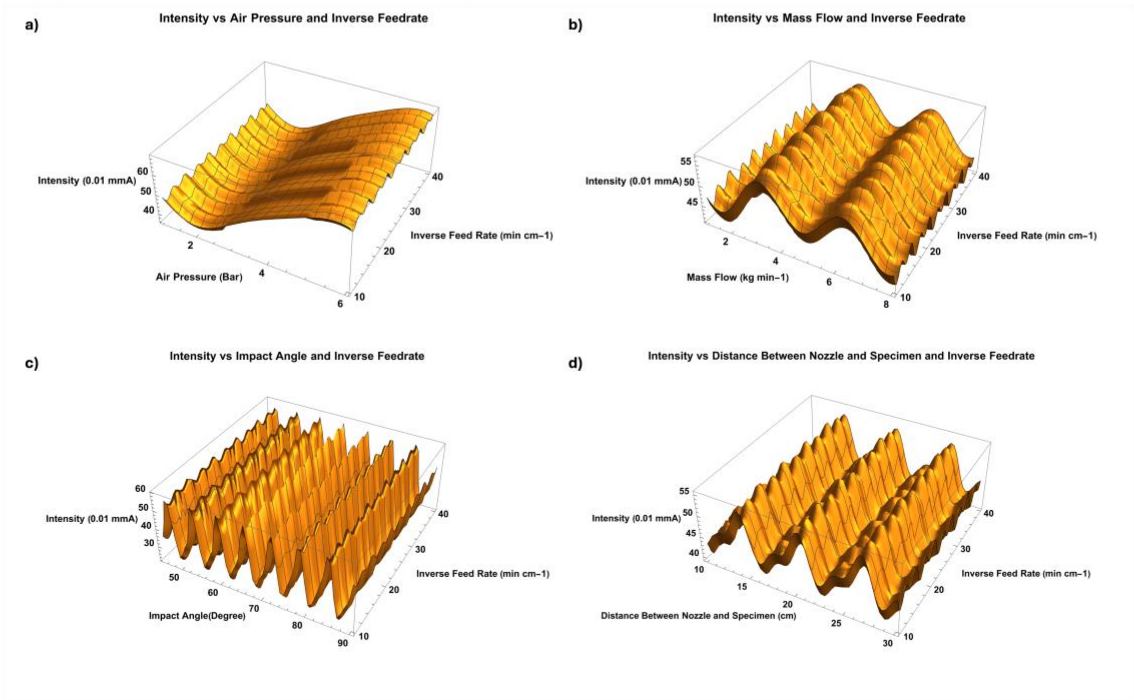

Figure 2.4 Intensity vs a) Air Pressure and Inverse Feedrate (Mass Flow = 4.5 kg·min^{-1}, Impact Angle = 90°, Distance Between Nozzle and Specimen = 25 cm), b) Mass Flow and Inverse Feedrate (Air Pressure = 3 bar, Impact Angle = 90°, Distance Between Nozzle and Specimen = 25 cm), c) Impact Angle and Inverse Feedrate (Air Pressure = 3 bar, Mass Flow = 4.5 kg·min^{-1}, Distance Between Nozzle and Specimen = 25 cm), d) Distance Between Nozzle and Specimen and Inverse Feedrate (Air Pressure = 3 bar, Mass Flow = 4.5 kg·min^{-1}, Impact Angle = 90°)

Figure 2.4 illustrates the intricate relationships between various shot peening parameters and their effects on intensity. In Figure 2.4a, it is evident that increasing air pressure generally elevates intensity; however, the interaction with the inverse feed rate introduces significant oscillations, indicating a non-linear relationship that requires careful balancing between these factors. This highlights the complexity of the relationship between air pressure and feed rate in controlling intensity.

Similarly, Figure 2.4b shows that a higher mass flow rate increases intensity, yet this relationship is also modulated by the inverse feed rate, resulting in periodic fluctuations. These fluctuations emphasize the importance of optimizing material throughput to achieve consistent intensity levels.

Figure 2.4c demonstrates that the intensity generally increases with a higher impact angle, but the influence of the inverse feed rate causes notable fluctuations, suggesting that an optimal combination of impact angle and feed rate is necessary for effective peening. This further underscore the intricate balance required between these parameters to achieve desired outcomes.

Finally, Figure 2.4d reveals that as the distance between the nozzle and the specimen increases, the intensity tends to decrease. This decrease is coupled with periodic variations driven by the inverse feed rate, underscoring the importance of nozzle distance in controlling energy transfer during the shot peening process.

These observations from the Figure 4 make it clear that each parameter significantly affects shot peening intensity. The observed fluctuations need to be carefully managed in practical applications to avoid undesirable effects. The strength of our model lies in its ability to accurately capture these complex interactions, making it a reliable tool for optimizing the shot peening process and ensuring consistent and effective surface treatment results.

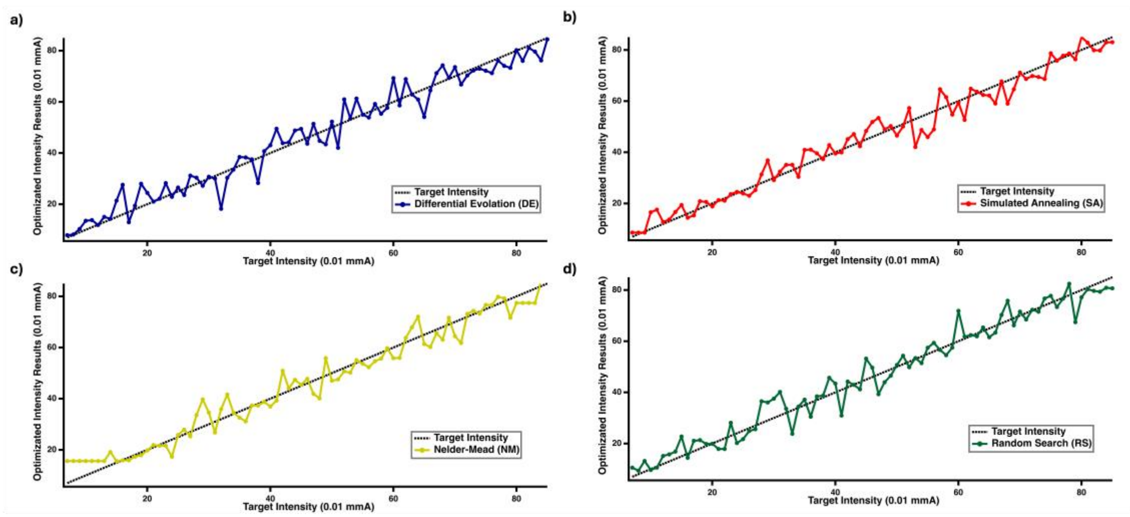

Figure 2.5 Target intensity vs optimized intensity results for a) Differential Evolution, b) Nelder-Mead, c) Simulated Annealing and d) Random Search

Figure 2.5 presents a comparison of four optimization methods: Differential Evolution (DE), Nelder-Mead (NM), Simulated Annealing (SA), and Random Search (RS), with their respective performance in achieving target intensity levels versus the optimized intensity results. The SOTN model functions served as the objective function for the nonlinear single-objective constrained optimization problems, providing a rigorous test environment for these methods. Throughout the optimization process, significant differences in computational time were observed among the methods. Random Search required the most computational time, followed by Differential Evolution, Simulated Annealing, and Nelder-Mead, which demonstrated the fastest performance. The primary objective of this analysis was to assess the reliability of these methods and identify the most suitable model for varying intensity levels, leading to a comprehensive recommendation.

Figure 2.5a focuses on Differential Evolution (DE), which generally shows strong alignment with the target intensities across various ranges. In the low-intensity range (10-20), DE performs well, with an average error of only 1.2%. However, in the middle-intensity range (30-40), DE's performance begins to fluctuate more, with an average error of 5.8%. As the target intensity increases into the high-intensity range (70-85), DE's effectiveness decreases further, with the average error rising to 9.5%. These fluctuations suggest that while DE is effective overall, it may require fine-tuning or additional constraints to reduce deviations and ensure more consistent performance across different intensity ranges [51,153].

Figure 2.5b presents the results of Simulated Annealing (SA), which shows varying levels of effectiveness depending on the intensity range. SA performs reliably in the low-intensity range (10-20), with an average error of 1%. However, in the middle-intensity range (30-40), SA maintains good accuracy, with an average error of 2.93%. As the intensity increases, SA begins to struggle more in the high-intensity range (70-85), with the average error increasing to 9%. These variations highlight the method's sensitivity to initial conditions and the stochastic nature of its search process, suggesting the need for adaptive strategies to maintain accuracy across the full intensity range [53,54].

Figure 2.5c examines the performance of the Nelder-Mead (NM) method, characterized by its simplicity and efficiency at lower intensities but struggling at higher intensities. In the low-intensity range (20-30), NM performs best, with an average error of 1.5%. However, NM shows increased deviations in the middle-intensity range (40-50), where the average error rises to 5.5%. As the intensity further increases into the high-intensity range (70-85), NM's performance declines significantly, with the average error rising to 12%. The method's tendency to converge to local minima, particularly in more complex landscapes, might explain these discrepancies, highlighting the potential benefits of integrating NM with other methods to improve its robustness [150].

Figure 2.5d illustrates the performance of the Random Search (RS) method, which, while covering a wide range of possibilities, displays varying effectiveness depending on the intensity range. RS performs well in the low-intensity range (20-30), with an average error of 2%. However, in the middle-intensity range (40-50), RS maintains a moderate performance, with an average error of 5.5%. In the high-intensity range (70-85), RS shows significant deviations, with the average error escalating to 10%. The inherently exploratory nature of RS, while beneficial for global search, seems to lack the precision needed for consistent performance, particularly as the complexity of the optimization landscape increases [58].

These detailed observations underscore the unique strengths and limitations of each optimization method. Figure 5 highlights that no single method universally outperforms the others across all intensity levels. Instead, each method has specific ranges, suggesting that a hybrid approach, combining the strengths of these methods, could offer a more reliable and effective optimization strategy [56,154].

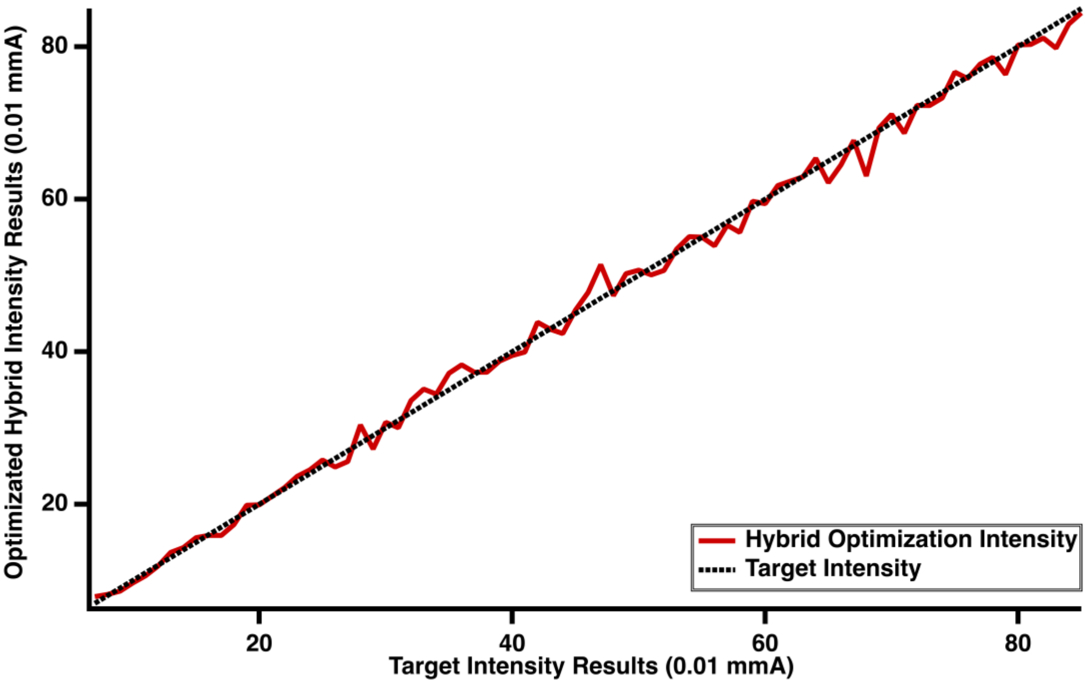

Figure 2.6 Target intensity vs hybrid optimized intensity results

Figure 2.6 shows the results obtained with the Hybrid Optimization Method. In this method, a combination of DE, SA, NM, and RS methods was used to obtain the results closest to the target intensity, respectively. The method utilized the corresponding optimization technique if the error rate was below 1%. If the error rate exceeded 1%, the next method was employed.

This Hybrid Optimization Method provided results closest to the target intensity values across different intensity ranges. In the Low-Intensity Range (10-20), the method achieved around 0.5% error. In the Middle-Intensity Range (30-40), it demonstrated approximately 1.5% error. In the High-Intensity Range (70-85), the error remained below 3%. Overall, the hybrid method outperformed other individual optimization methods with an average error percentage of 2.69%, indicating its superior accuracy and reliability across a wide range of intensities.

These results suggest that the hybrid method offers more consistent and accurate results across a wide range of intensities and minimizes error compared to other methods. Thus, the hybrid optimization approach is considered a more reliable and effective method.

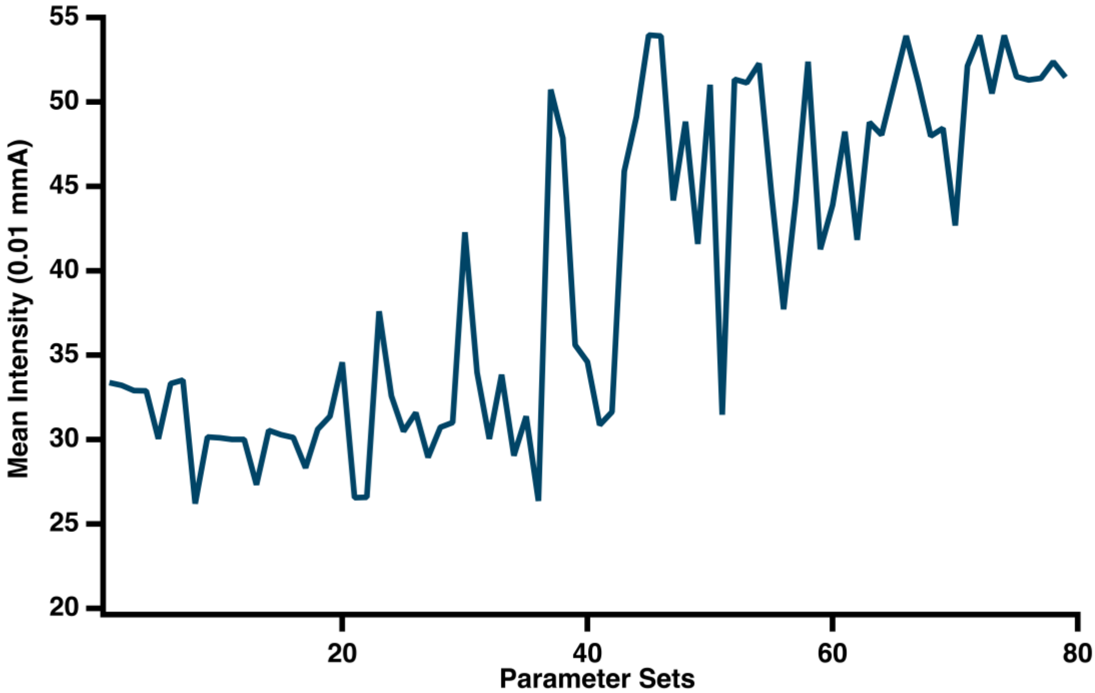

Figure 2.7 Monte Carlo Mean Intensity Simulation Results

The Monte Carlo simulations were conducted to evaluate the robustness of the model across different parameter sets. Figure 2.7 indicates that the average Intensity values show significant variability across the parameter sets. For instance, the mean Intensity value ranged from approximately 26.2 to 53.9 across the different parameter sets. Notably, around parameter set 37, the mean Intensity value reached a peak of 50.7, indicating a strong model performance in this region. However, earlier parameter sets, such as set 8 and 22, exhibited lower mean intensity values around 26.2, suggesting potential weaknesses in the model under these conditions.

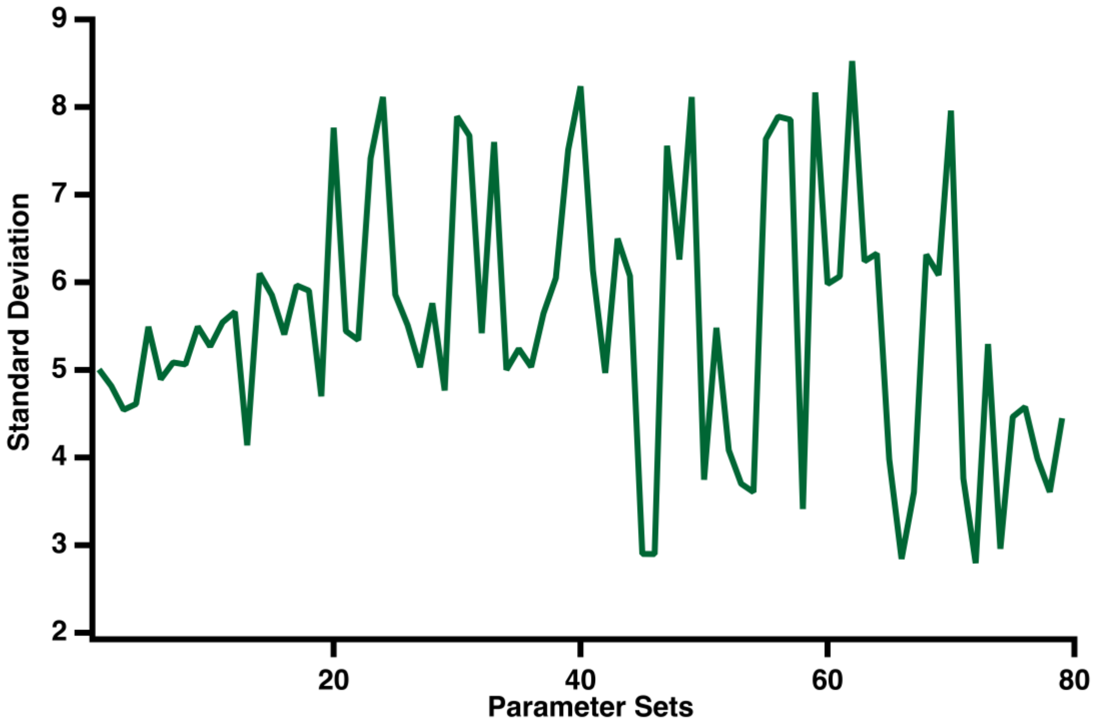

Figure 2.8 Figure caption Monte Carlo Standard Deviation Results

Figure 2.8 provides further insights by illustrating the variability within each parameter set. The standard deviations ranged from approximately 2.7 to 8.2, indicating the degree of uncertainty in the model's predictions. Higher standard deviations, such as 8.2 around parameter set 20, suggest greater variability and, consequently, less reliable model performance. Conversely, lower standard deviations, like the 2.7 observed at parameter set 54, indicate more consistent predictions, thus higher reliability in those scenarios.

These results from the Monte Carlo simulations highlight the sensitivity of the model to different parameter sets. The significant fluctuations in both mean Intensity values and standard deviations suggest that while the model performs reliably under certain conditions, there is a need for further refinement, especially in the parameter sets that introduce higher variability. Addressing these areas could enhance the model's overall accuracy and predictive power [16,155].

The analysis confirms that the Hybrid Optimization Method consistently provides the most accurate and reliable results across varying intensity levels, with a particularly strong performance in the low and middle-intensity ranges. The average error rate of

2.69% underlines its superiority over other methods, making it the recommended choice for applications requiring precision. While Differential Evolution (DE) is effective, particularly in mid to high-intensity scenarios, the variability in Nelder-Mead (NM) and Random Search (RS) suggests that they are less suited for tasks demanding high accuracy. These findings are consistent with existing literature, affirming the Hybrid Method's efficacy in optimizing complex landscapes.

2.3 Conclusion

In this study, the Second-Order Trigonometric Nonlinear (SOTN) model emerged as the most reliable for predicting shot peening intensity, achieving R^2 values of 0.93 in training and 0.90 in testing, with consistent Model Efficiency (ME) values of 0.90. Four optimization methods were tested, with Simulated Annealing (SA) yielding the lowest mean error of 4.8%. The DE method achieved a mean error percentage of 7.2%. However, Nelder-Mead (NM) and Random Search (RS) showed higher errors of 13.5% and 17.2%, respectively. To improve reliability, a hybrid optimization approach combining DE, SA, NM, and RS was developed, reducing the overall error to 2.69%.

Monte Carlo simulations further validated this hybrid approach, showing consistent performance across various intensity levels. Mean intensity values ranged from 32.94 to 53.9, with standard deviations between 2.7 and 8.2, confirming the hybrid model’s robustness and accuracy. These findings provide a reliable and practical solution for optimizing shot peening parameters, ensuring precise and consistent results across a broad range of conditions.

Chapter 3

Critical Failures in Aviation Components: The Role of Hydrogen Embrittlement

Hydrogen embrittlement (HE) poses a critical safety risk in the aviation industry, causing unexpected failures in high-strength metals and alloys used in essential components. This study focuses on detailed analyses of multiple aviation incidents and accidents where HE played a significant role, with particular attention to failures in helicopter drive systems and fixed-wing aircraft crankshaft bolts. Investigations revealed that these failures were primarily caused by hydrogen introduced during manufacturing processes, such as electroplating and surface treatments, which were insufficiently mitigated by post-processing techniques like dehydrogenation. These incidents led to the issuance of Airworthiness Directives (ADs), which mandated corrective actions to prevent similar occurrences, such as improved manufacturing protocols and enhanced material testing. By presenting concrete evidence from metallurgical analyses and documented aviation failures, this paper highlights the critical need for robust manufacturing controls, stringent post-treatment procedures, and continuous monitoring to address hydrogen embrittlement risks effectively and enhance aviation safety.

3.1 Introduction of Hydrogen Embrittlement

The history of aviation is marked by significant milestones in technology, safety, and operational advancements. From the Wright brothers' first powered flight in 1903 to the supersonic speeds of Concorde and the advanced automation of modern commercial jets, aviation has consistently pushed the boundaries of what is possible. Early pioneers faced considerable challenges, including unreliable engines, rudimentary aerodynamics, and limited materials science knowledge. Early aircraft, often constructed from wood and fabric, were prone to wear and structural failures. Compounding these issues were adverse weather conditions, inadequate infrastructure, and a lack of standardized safety protocols, making early flight both daring and high-risk [156].

Advances in material technology have been pivotal in addressing these challenges, transforming aviation into a safer and more reliable mode of transportation. The introduction of lightweight metals like aluminum in the 1920s revolutionized aircraft design, enabling stronger, more durable airframes while maintaining fuel efficiency [157]. In later decades, composite materials such as carbon fiber provided unparalleled strength, flexibility, and resistance to fatigue and corrosion. These innovations enhanced safety, reduced weight, and extended the operational lifespan of modern aircraft [158].

Technological advancements have also shaped other aspects of aviation. The evolution of engines from piston-driven to jet propulsion increased speed, range, and reliability, while avionics innovations reduced human error and operational workload [159]. Today, aviation is one of the safest modes of transportation, reflecting the relentless efforts of engineers, scientists, and regulators. These breakthroughs have also made air travel more accessible, connecting people and cultures worldwide.

Despite these advancements, accidents have remained a persistent concern throughout aviation history. In the early years, accidents were frequent and catastrophic, often caused by unreliable engines, limited pilot training, and unpredictable weather. Over time, as technologies and operations became more complex, the nature of accidents evolved to include both human and technical factors. Human errors, such as miscommunication or procedural deviations, remain the leading cause of incidents. However, technical failures, including engine malfunctions, structural weaknesses, and environmental factors, like severe weather or runway conditions, pose significant risks [160].

To address these challenges, organizations like the National Transportation Safety Board (NTSB) and the International Civil Aviation Organization (ICAO) have developed robust accident investigation frameworks. These efforts have enhanced understanding, prevention, and mitigation strategies, leading to a steady decline in accident rates. However, with growing air traffic and evolving technologies, the aviation industry must continuously adapt to emerging risks.

Among these risks, material degradation mechanisms, such as Hydrogen Embrittlement (HE), have emerged as critical technical challenges. HE has been implicated in multiple severe aviation accidents, especially involving high-strength alloys subjected to cyclic mechanical stresses and harsh environmental conditions. Analyzing such cases is vital for formulating effective prevention methods and enhancing structural integrity in aerospace systems.

The NTSB aviation database highlights the complexity of aviation safety. Database has a total of 176,673 recorded accidents and incidents, and only 61,492 cases include detailed explanations of probable causes [161]. These findings emphasize the importance of addressing diverse issues, including human performance, technical reliability, structural integrity, and aerodynamic functionality, to improve safety. Figure 3.1 illustrates the distribution of cases with probable causes. Human factors account for 52.1% of incidents, emphasizing the critical role of pilot performance and decision-making. Technical issues contribute 22.4%, highlighting the importance of engine reliability, maintenance, and electronic systems. Aerodynamic performance accounts for 13.8% of cases, reflecting challenges such as directional control and airspeed management. Structural issues comprise 7.2%, encompassing material fatigue, corrosion, and design failures, while cases involving multiple factors represent 4.2%. This distribution underscores the dominance of human-related factors while also highlighting the need to address technical and structural challenges to improve aviation safety further.

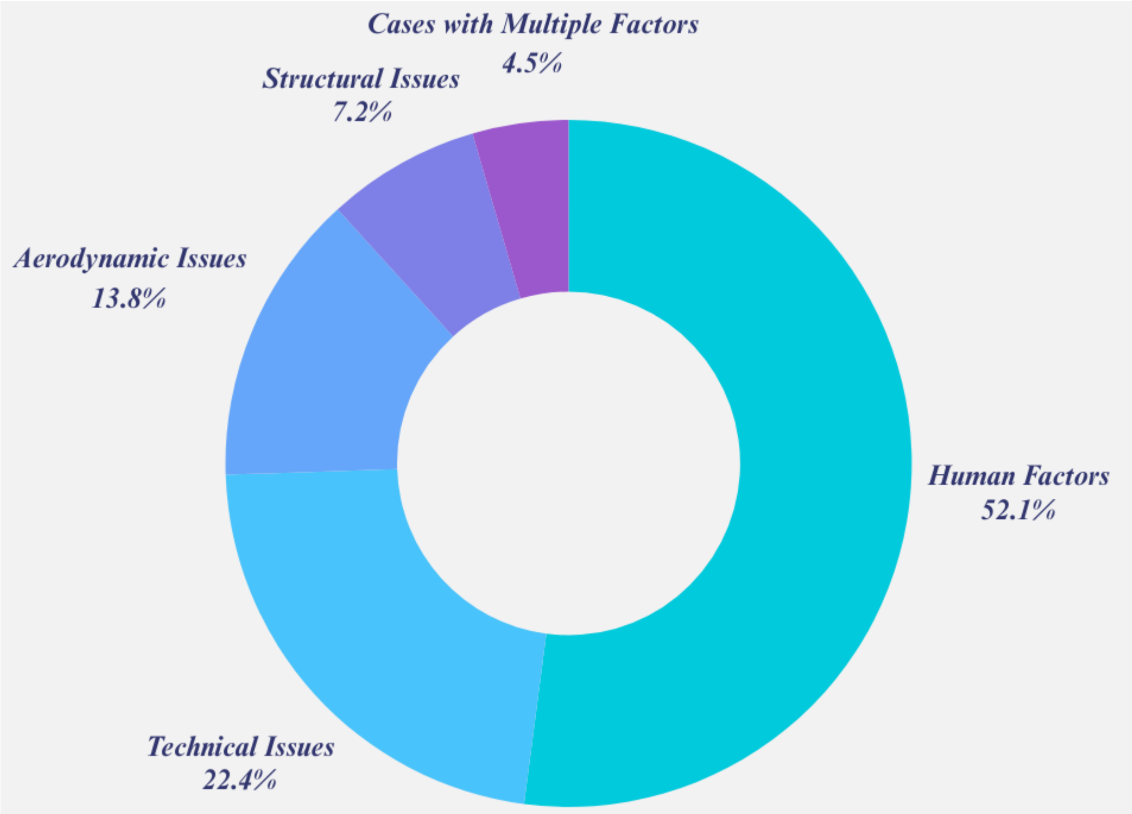

Figure 3.1 Aircraft incident cases with probable cause

Figure 3.2 illustrates the annual number of global aviation accidents in scheduled commercial air transport operations. According to ICAO safety reports, accident numbers fluctuated during this period [162]. The highest number of accidents occurred in 2019, with 114 incidents preceding the COVID-19 pandemic. The pandemic years 2020 and 2021 saw a significant decline, with only 48 accidents each year, likely due to reduced air traffic. In 2022, as aviation activities resumed, accidents increased to 64. This data reflects the correlation between operational volume and accident occurrence, emphasizing the need for vigilance as air traffic normalizes.

Figure 3.2 Global Aviation Accidents (2017-2022) [162]

According to ICAO safety reports, Figure 3.3 highlights the percentage distribution of aviation accident causes from 2017 to 2022 [162]. Human factors consistently represent the largest share, ranging between 50% and 54%, reinforcing their significant role in aviation safety. Technical failures, the second-largest contributor, account for 21% to 25% of accidents, underscoring the importance of reliable systems and maintenance. Aerodynamic performance issues remain relatively steady at 11% to 14%, while structural issues contribute 6% to 8%. Cases involving multiple factors hover around 5% to 6%, reflecting the complexity of interactions in aviation incidents. This distribution underscores the need for targeted improvements in both technical and operational domains.

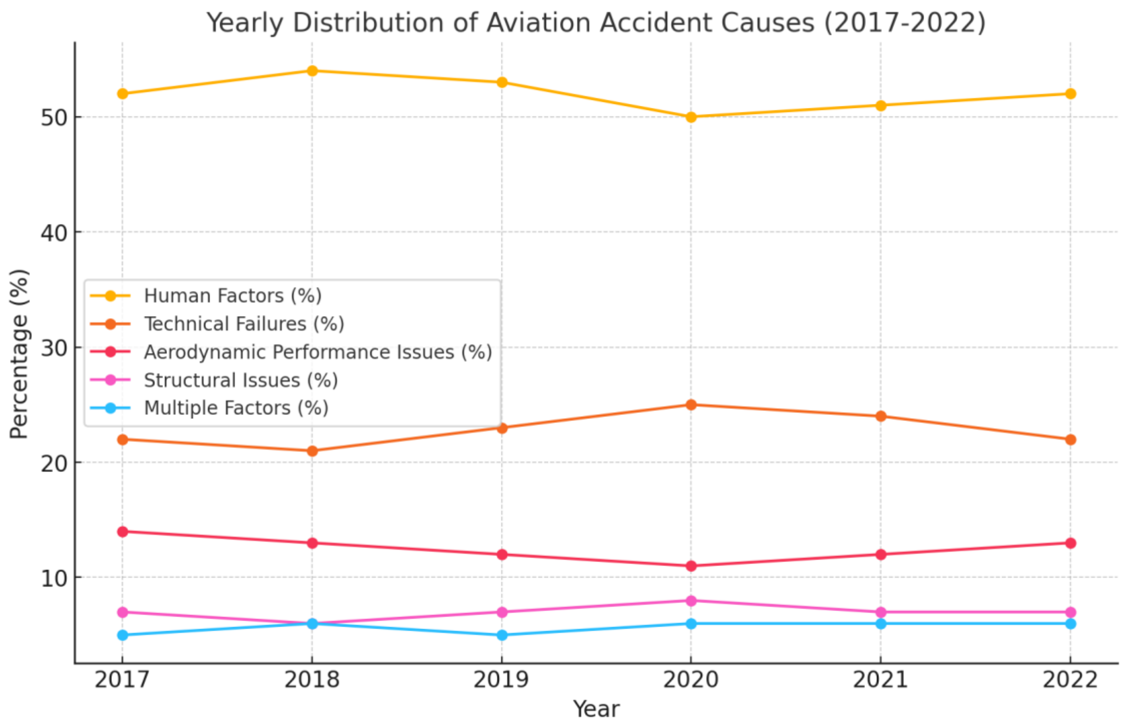

Figure 3.3 Yearly distribution of aviation accident causes (2017-2022) [162]

Among the multifaceted challenges in aviation safety, material degradation mechanisms like Hydrogen Embrittlement (HE) require focused attention due to their potential to cause catastrophic failures. Characterized by hydrogen absorption and diffusion into metallic components, HE poses significant risks, especially in environments where high-strength materials are exposed to hydrogen during manufacturing, maintenance, or service. Notable aviation incidents have implicated HE, underscoring the need for comprehensive analysis and mitigation strategies. The importance of this study lies in its detailed presentation of real-world aviation incidents and accidents linked to hydrogen embrittlement, supported by concrete evidence and metallurgical analysis. Unlike many aviation safety studies that predominantly focus on statistical analyses, this work provides an in-depth examination of documented cases, bridging the gap between theoretical understanding and practical implications. This review aims to shed light on critical vulnerabilities and offer actionable solutions to improve aviation safety by emphasizing robust material selection, manufacturing controls, and post-processing techniques.

3.2 Airworthiness Directives

Airworthiness Directives (ADs) are essential regulatory mandates designed to ensure the flight safety and operational reliability of aircraft [163]. The mentioned directives, typically issued by aviation authorities like the FAA, EASA and National Airworthiness Authorities (NAA) address identified unsafe conditions in aircraft systems, engines, or components that could compromise flight safety. ADs often emerge following accident investigations, recurring operational issues, or identified manufacturing flaws, requiring operators to take specific corrective actions such as inspections, modifications, or part replacements. Their primary goal is to mitigate risks, ensure continued airworthiness, and prevent further incidents. [164].

When a safety concern arises, manufacturers are often required to thoroughly assess the affected components or systems, identifying root causes and providing solutions. In some cases, this process may lead to an immediate grounding of aircraft or urgent part replacements under an AD to prevent further risks. For instance, ADs might mandate inspections to detect hidden defects, operational restrictions to mitigate risk, or the replacement of defective parts with redesigned or higher-quality alternatives. This collaborative approach between regulatory bodies, manufacturers, and operators ensures that identified issues are promptly resolved, safeguarding aviation safety.

As illustrated in Figure 3.4, the FAA has issued 167,751 ADs addressing a wide variety of concerns [165]. Among these, operational issues like directional control (5,963 ADs) and inappropriate airspeed (3,348 ADs) dominate, reflecting the complexity of managing real-world flight conditions. Structural challenges, such as cracks (1,532 ADs), corrosion (1,322 ADs), and fatigue (1,254 ADs), also represent critical focus areas. While less frequent, issues like hydrogen embrittlement (HE) and stress corrosion cracking account for 12 and 150 ADs, respectively. Although small, these ADs highlight the significant risks posed by material degradation in critical components, requiring precise mitigation efforts.

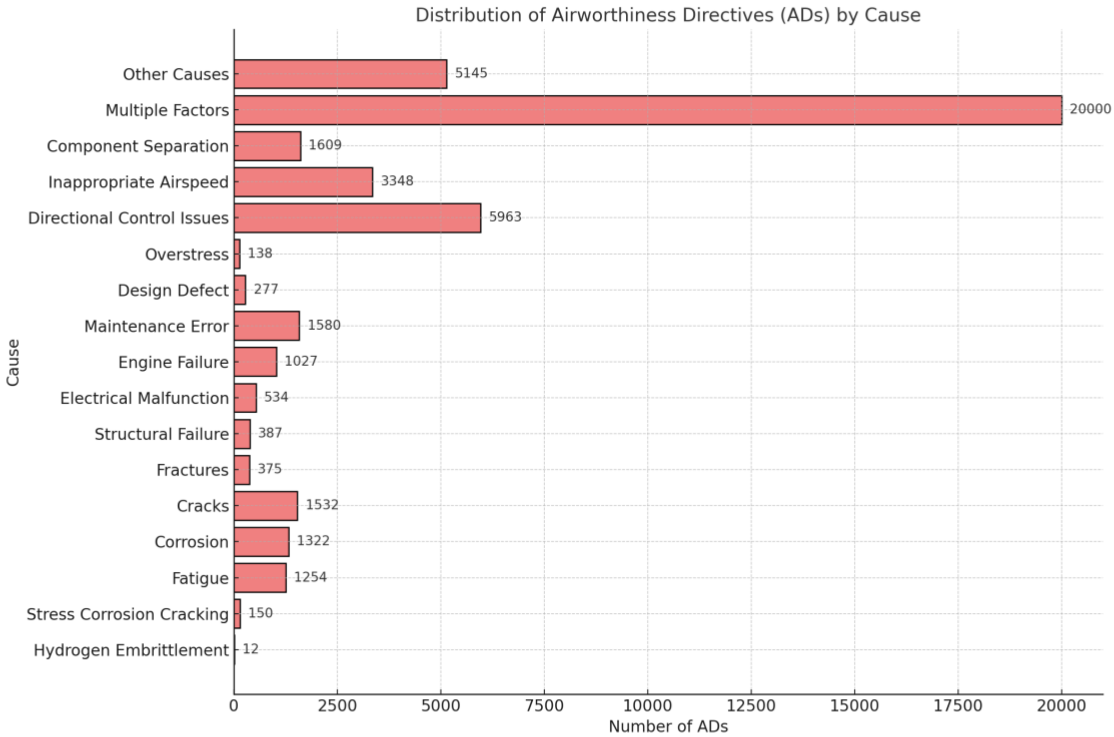

Figure 3.4 Global Aviation Accidents

The inclusion of hydrogen embrittlement among ADs emphasizes the growing recognition of material failures in aviation safety. Hydrogen embrittlement has been implicated in failures of critical parts like landing gear struts, crankshaft bolts, and helicopter drive assemblies. While accounting for only 12 ADs, HE incidents demonstrate the catastrophic potential of undetected material weaknesses, often introduced during manufacturing processes such as electroplating or insufficient post-treatment baking.

This transition from broader AD-related concerns to the specific challenges of HE underscores the need for precise manufacturing protocols and rigorous maintenance practices. In the following section, an in-depth exploration of hydrogen embrittlement, its mechanisms, and real-world impacts will illuminate this critical aviation safety challenge.

3.3 Protection Mechanisms Against Hydrogen Embrittlement

Hydrogen-induced damage occurs when hydrogen atoms diffuse into metals, leading to mechanical property degradation, reduced ductility, and eventual failure [113,166,167]. This phenomenon, known as hydrogen embrittlement (HE), presents significant challenges, particularly in industries such as aerospace and energy [168]. The mechanisms behind HE includes complex mechanisms such as Hydrogen-Enhanced Local Plasticity (HELP) and Hydrogen-Enhanced Decoherence (HEDE), which alter the metal's microstructure and increase susceptibility to cracking under stress [104,169–171]. HELP promotes dislocation movement and localized deformation, while HEDE weakens atomic bonds at grain boundaries, leading to brittle fractures [172,173]. Additionally, processes like Adsorption-Induced Dislocation Emission (AIDE) facilitate dislocation movement at crack tips, further contributing to embrittlement [174]. These processes collectively alter a material's microstructure, increasing its susceptibility to cracking under stress. Numerous studies have been conducted to better understand these mechanisms, providing valuable insights into how hydrogen interacts with different materials and the conditions that exacerbate embrittlement [105,111,114,175–178].

Aviation components are particularly vulnerable to hydrogen embrittlement due to their exposure to cyclic loads, harsh environmental conditions, and high material strength requirements. For example, in certain Airbus A380 aircraft, hydrogen-assisted cracking accelerated the development of cracks in wing spars after extended periods of storage in specific environmental conditions [179]. Similarly, failures in helicopter drive systems and fixed-wing aircraft crankshaft bolts have been traced to hydrogen embrittlement introduced during manufacturing processes, such as electroplating and surface treatments [180]. These incidents underscore the critical need for stringent manufacturing controls, post-processing treatments, and improved material testing methods to mitigate hydrogen-induced risks [87,120]. It is noteworthy that, by eliminating residual hydrogen and enhancing system reliability, flight safety can be significantly improved.

Efforts to mitigate HE focus on preventing hydrogen ingress and removing residual hydrogen through post-treatment processes. Advancements in protective treatments, such as anodizing, coatings (e.g., Al-Si-Zn, Zn-Ni, Graphene), and platings (e.g., Cr, Zn-Co, Zn-Ni, ZrN, Cd), have been developed. These methods aim to enhance corrosion resistance and act as barriers against hydrogen ingress during the service life of critical components [181–191]. However, these protective methods can inadvertently introduce hydrogen into the material surface through chemical solution exposure. [100,192–194]. If manufacturing controls and post-treatment processes are insufficient, parts subjected to high cyclic loads and environmental exposure, making them vulnerable to HE-related failures [95,195,196]. Post-treatment processes such as baking and pulsed electric current, a heat treatment designed to remove residual hydrogen through diffusion, are critical for reducing the risk of embrittlement.

To address this issue, baking—a post-treatment heat treatment process—is designed to remove hydrogen introduced during manufacturing through diffusion, thereby reducing the risk of hydrogen embrittlement. This process operates under specific temperature and duration parameters, which vary depending on the material and are typically defined in manufacturer specifications [197,198]. However, the efficacy of this process is often assessed using specimens placed alongside the component during the process, leaving the component itself untested. This approach introduces uncertainties about the process's reliability. Additionally, current verification methods, which predominantly rely on destructive testing, such as Thermal Desorption Analysis (TDA) and Scanning Electron Microscopy (SEM), limit the ability to evaluate components comprehensively [199–203]. However, these methods necessitate component destruction, limiting their use to samples and making them impractical for widespread operational evaluations. These limitations highlight the need for more advanced techniques to ensure thorough hydrogen removal and component integrity [204].

Non-destructive testing (NDT) methods are emerging as promising alternatives, offering the potential to evaluate materials and detect HE without damaging components. Techniques such as neutron imaging, x-ray diffraction, and electrochemical permeation testing demonstrate potential for real-time assessments [205–209]. However, these technologies are still in developmental stages and have yet to be widely implemented on a large scale. The primary challenge lies in integrating such detection methods into the operational lifecycle, where design constraints and control requirements for HE-specific evaluations remain difficult to define.

This gap between current detection capabilities and the operational reality of aviation highlights the critical importance of robust manufacturing controls and maintenance practices. Failures due to HE, as underscored by documented incidents, often stem from lapses in manufacturing or post-processing protocols, such as insufficient dehydrogenation. Furthermore, the complexity of defining HE-specific detection and control measures exacerbates the difficulty of integrating effective solutions into design specifications.

The following sections delve into five detailed aviation incidents investigated by the National Transportation Safety Board (NTSB), where HE-induced failures played a significant role. These case studies not only illustrate the devastating potential of HE but also underline the urgency of implementing stringent quality control measures, effective maintenance strategies, and proactive regulatory oversight to prevent such occurrences. This synthesis of real-world events provides a crucial foundation for understanding the systemic improvements needed to mitigate HE risks in the aviation industry.

3.3.1 Failure of the Bell 412EP Helicopter (ERA10TA493)

On September 22, 2010, a Bell 412EP helicopter, encountered a critical mechanical failure during its final approach to Floyd Bennett Field in Brooklyn, New York. The sudden mechanical failure forced the pilot to execute an emergency autorotation landing into Jamaica Bay. Thankfully, all six crew members sustained only minor injuries, but the helicopter suffered significant damage, particularly to its powerplant system. The flotation devices, shown in Figure 3.5, successfully deployed, preventing the helicopter from sinking despite the severe damage incurred during the emergency landing.

Figure 3.5 The Bell 412EP helicopter resting in Jamaica Bay after the emergency landing [210].

Subsequent investigations pinpointed the failure's origin in the output drive gear (ODG) of the helicopter's reduction gearbox. A detailed metallurgical analysis revealed a fatigue fracture that initiated at the root of one of the gear teeth, shown in Figure 3.6. The fracture propagated due to hydrogen embrittlement (HE), a phenomenon where hydrogen atoms penetrate the metal, resulting in brittleness and cracking. The microscopic examination identified both intergranular and transgranular crack propagation patterns, which are hallmark indicators of hydrogen embrittlement.

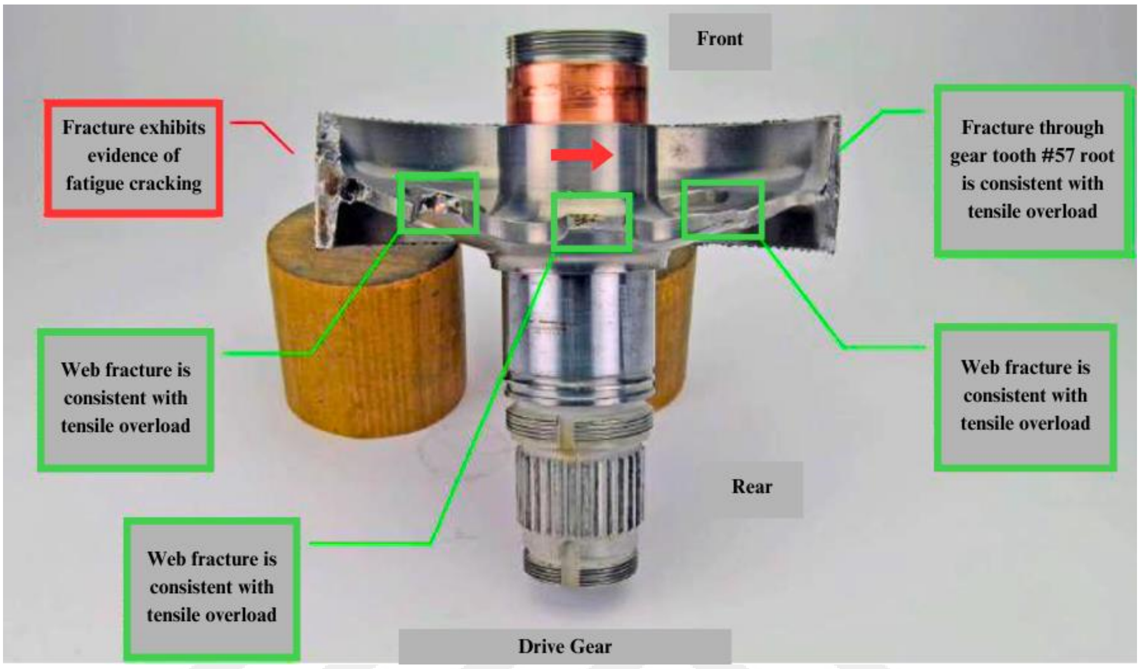

Figure 3.6 Detailed view of the fractured output drive gear from the reduction gearbox [210].

The microscopic examination provided further insight into the failure mechanism. As depicted in Figures 3.7 and 3.8, intergranular cracking at the gear tooth root and distinct patterns of fatigue crack propagation were observed. The intergranular cracking, shown in Figure 3.7, highlighted hydrogen's role in weakening grain boundaries, making the material more susceptible to stress. Meanwhile, Figure 3.8 revealed the propagation of fatigue cracks emanating from the hydrogen-embrittled region, with the microscopic evidence clearly indicating the insufficient removal of residual hydrogen during dehydrogenation treatments. Together, these findings confirmed hydrogen embrittlement as the root cause of the component's failure.

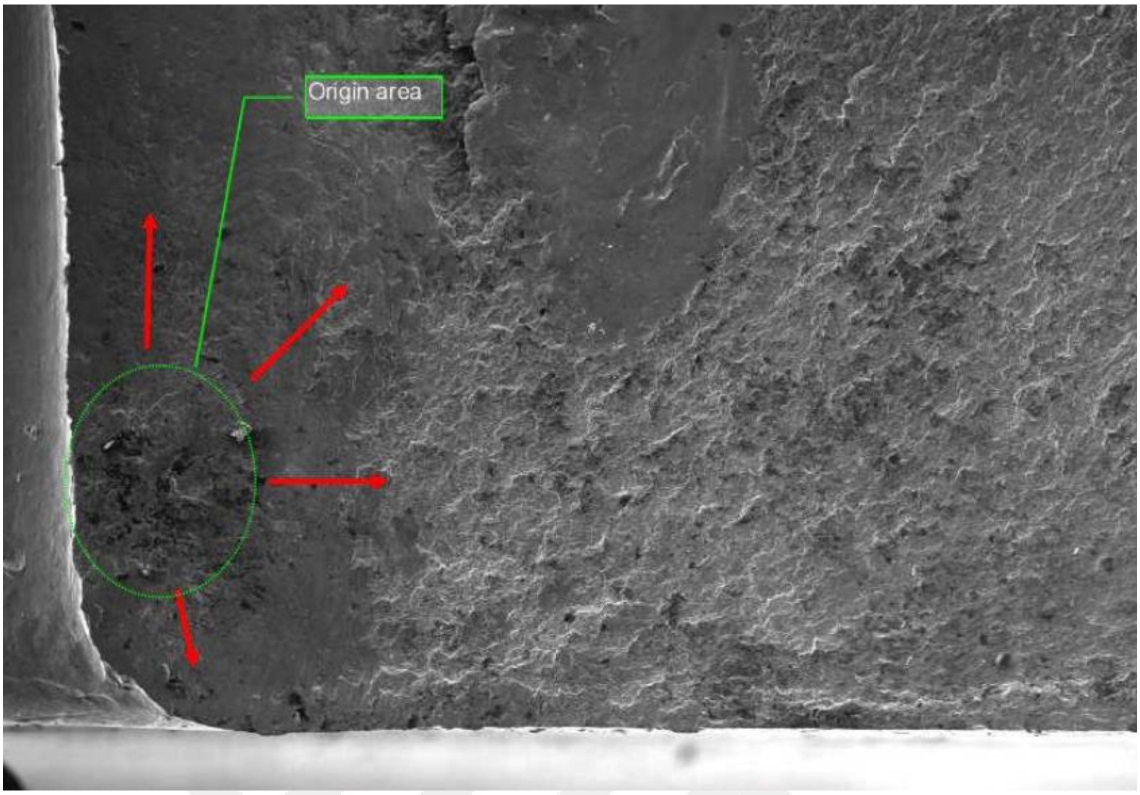

Figure 3.7 Close-up of the origin region of the fatigue crack on the output drive gear, showing the initial intergranular cracking due to hydrogen embrittlement [210].

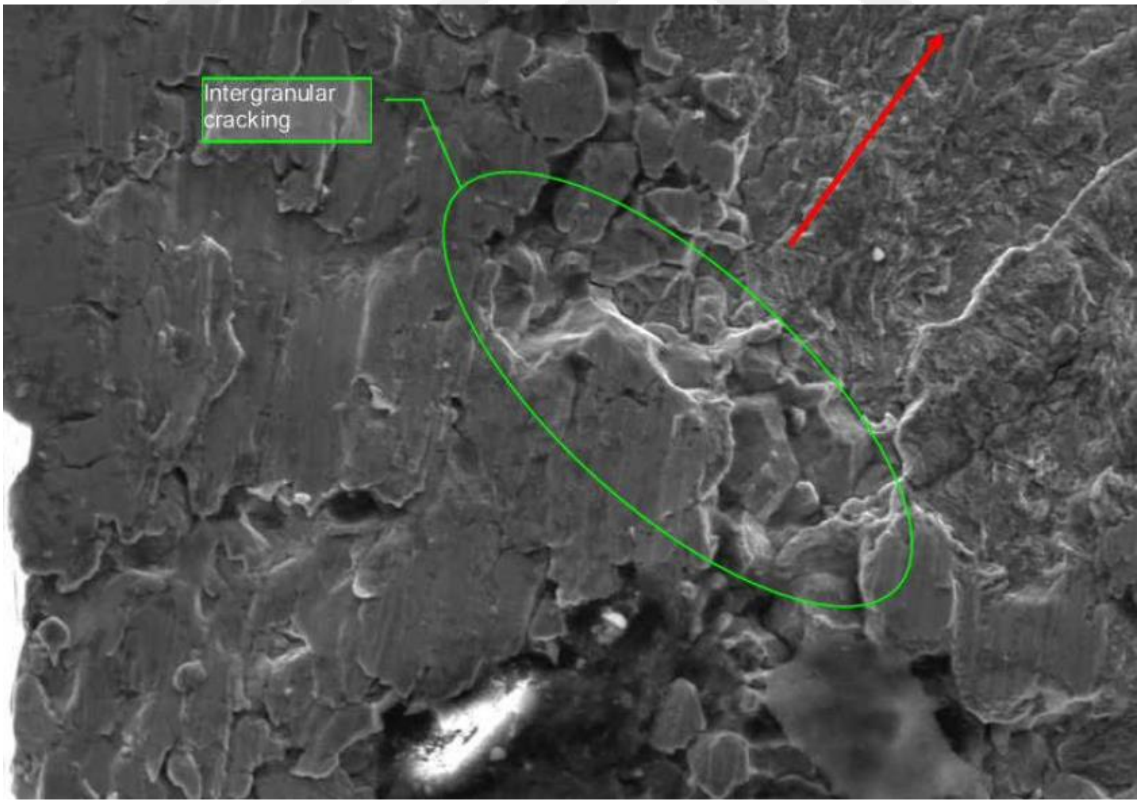

Figure 3.8 Microscopic view of the fracture surface, showing the distinct patterns of fatigue crack propagation starting from the hydrogen-embrittled region [210].

The Bell 412EP incident underscores the urgent need for improved manufacturing controls and rigorous quality assurance to address hydrogen embrittlement risks. The current reliance on destructive testing for hydrogen detection is inadequate for comprehensive component evaluation. This incident exemplifies the critical importance of advancing non-destructive testing methods to identify residual hydrogen during manufacturing and maintenance. By implementing these improvements, the aviation industry can enhance the reliability of high-stress components and mitigate risks associated with hydrogen embrittlement.

3.3.2 Failure of the Bell 222U Helicopter (CEN10FA291)

On June 2, 2010, a Bell 222U helicopter suffered a catastrophic in-flight breakup during a post-maintenance flight near Midlothian, Texas. The helicopter, piloted by an airline transport pilot and accompanied by a mechanic, experienced structural failure that led to the separation of critical components, including the tail boom and main rotor hub. Witnesses reported seeing debris falling from the aircraft before it impacted the ground and erupted into flames, resulting in the tragic loss of both crew members.

Prior to the incident, the rotor components of the helicopter were reported as fully operational. Figure 3.9 shows the rotor head assembly of the Bell 222U helicopter before the accident, with key components such as the A-side drive pin, B-side pitch link, and cyclic actuators clearly labeled.

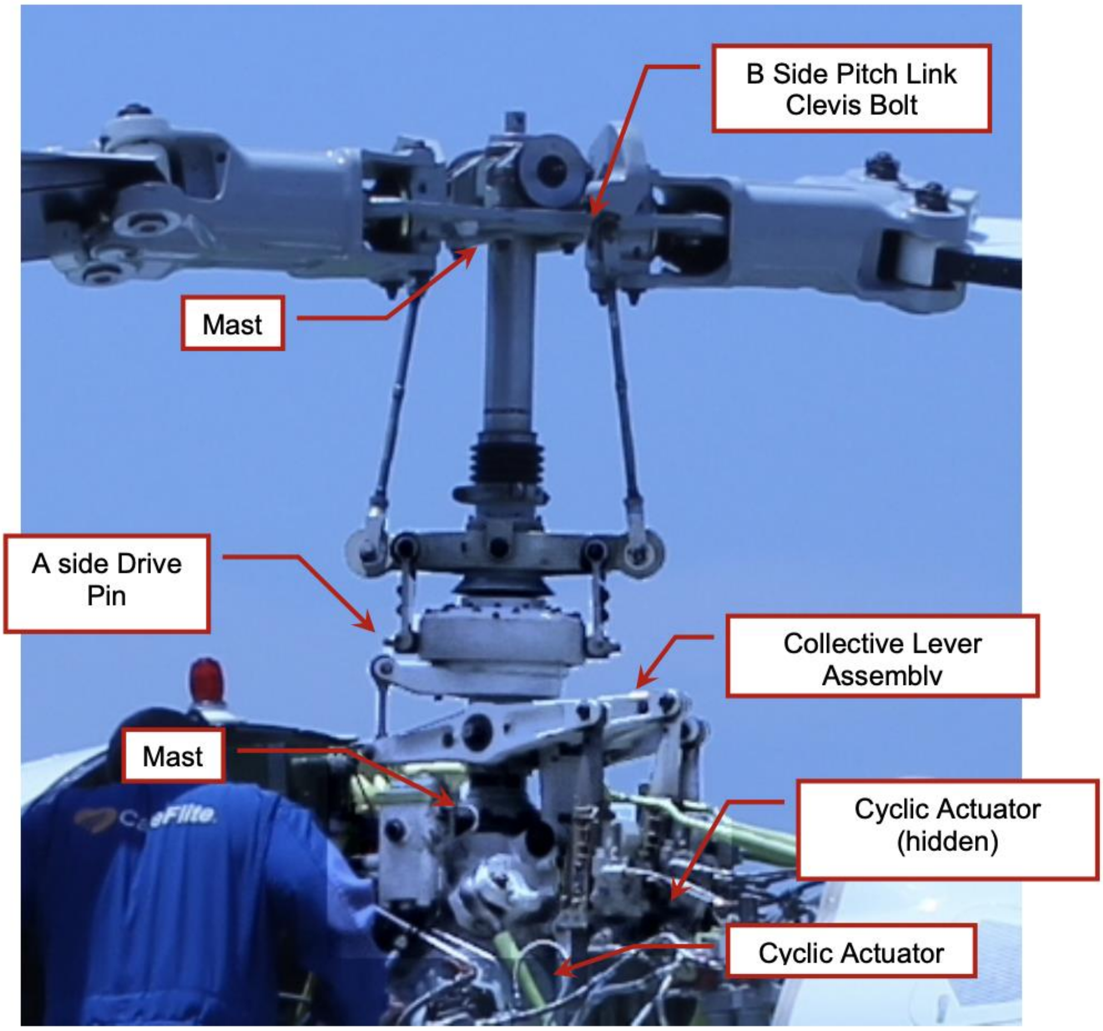

Figure 3.9 Image showing the rotor head of the Bell 222U helicopter before the accident, with critical components identified [211].

Subsequent investigations revealed that the primary cause of the structural failure was the fracture of the A-side drive pin within the swashplate assembly. Metallurgical analysis identified the fracture as overstress-induced, but further detailed examination of the fracture surface revealed brittle cleavage features and intergranular separations consistent with hydrogen embrittlement (HE). Measurements taken from the fractured pin confirmed hydrogen levels between 8.7 and 9.3 ppm, indicating that absorbed hydrogen significantly contributed to material degradation. Figure 3.10 shows the rotor components after disassembly, with failure points, including the A-side drive pin, highlighted.

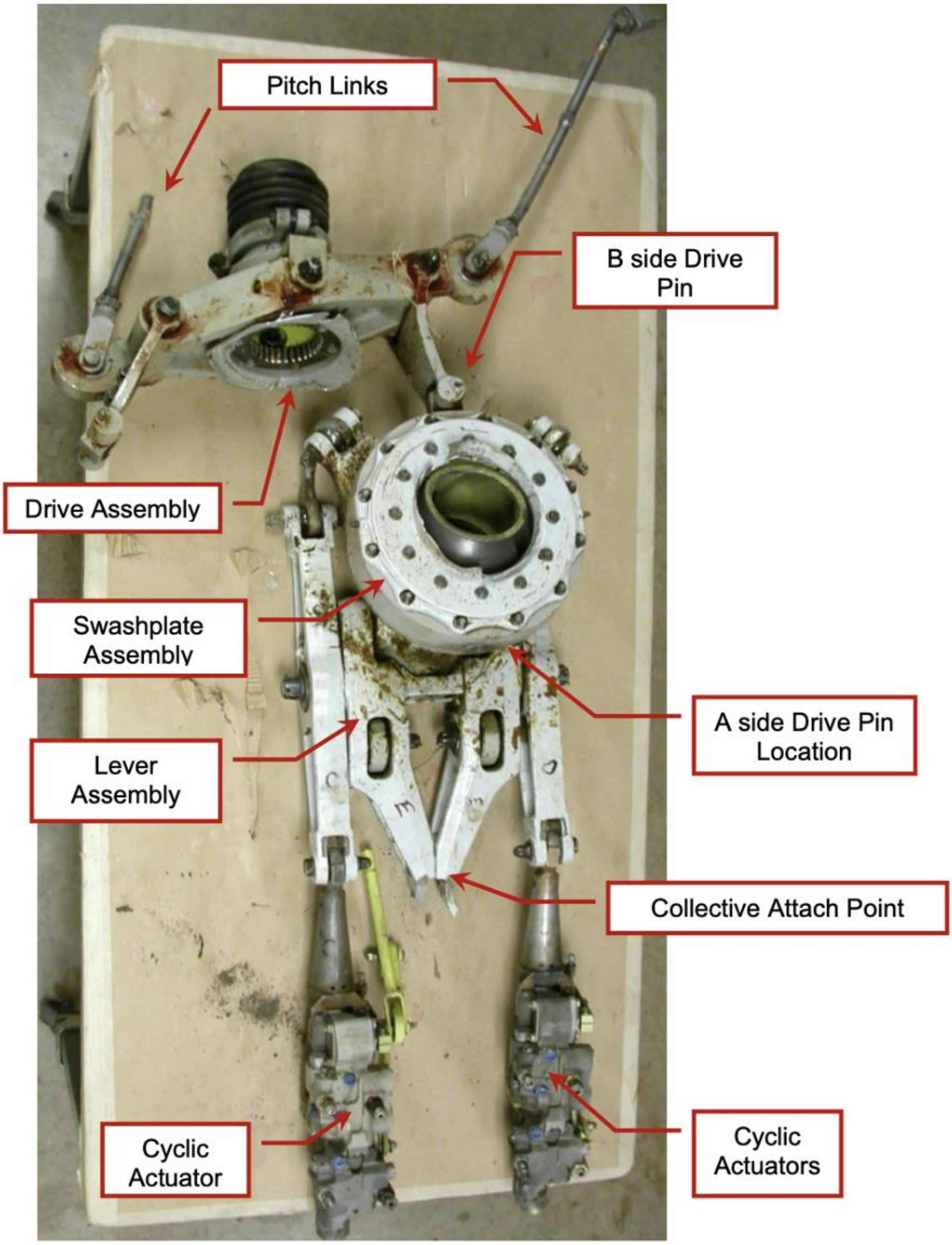

Figure 3.10 Separated rotor components prior to disassembly, highlighting the critical assemblies (swashplate, drive assembly, and pitch links) [211].

Further examination under a scanning electron microscope (SEM) provided critical evidence of the brittle failure mechanism. The fractured surface of the A-side drive pin showed brittle cleavage and intergranular separations, highlighting how hydrogen atoms migrated into areas of high stress within the material. This accumulation of hydrogen weakened the structural bonds, leading to the failure of the drive pin under conditions it would normally withstand. Additionally, Figure 3.11 shows radial cracks on the washer face of the A-side pin, further supporting hydrogen embrittlement as a key contributor to the failure. These cracks, observed at low magnifications, intersect the primary fracture and demonstrate localized plasticity near initiation sites where hydrogen atoms accumulated.

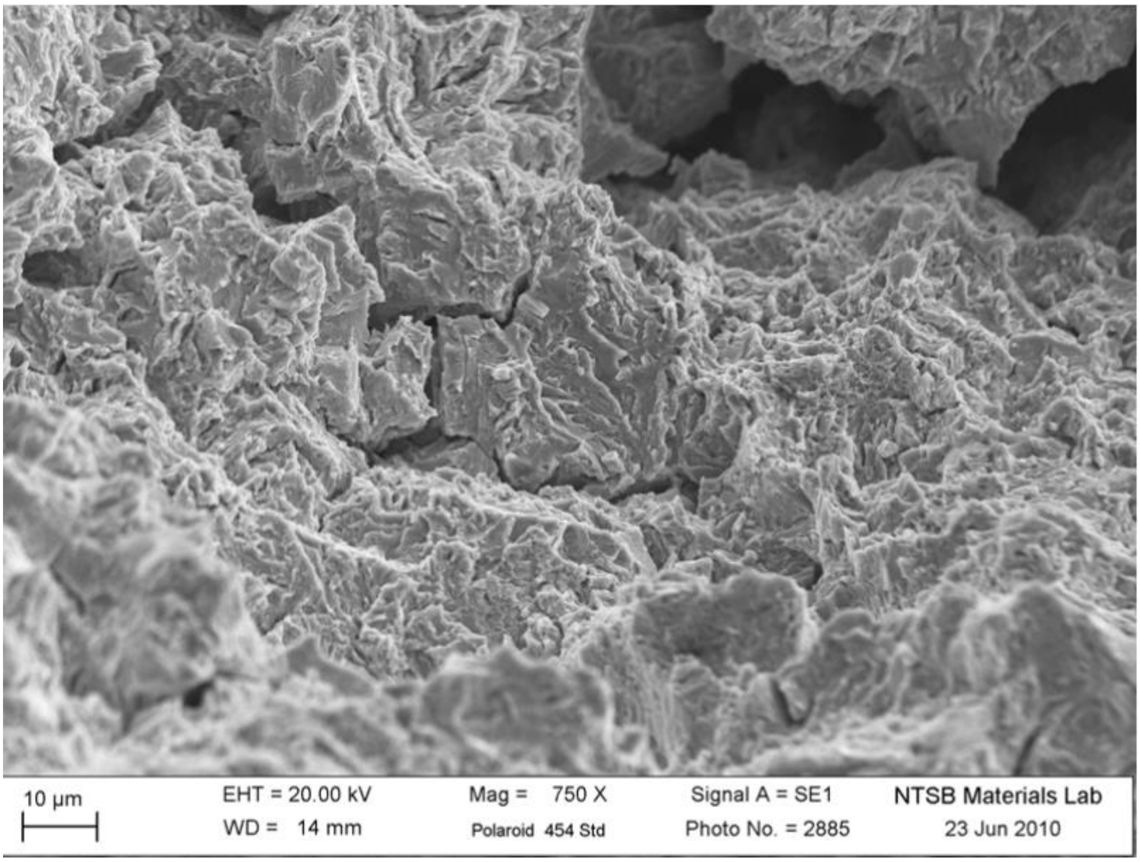

Figure 3.11 SEM image of radial cracks on the washer face of the A-side pin, showing areas of localized plasticity [211].

At higher magnifications, SEM analysis revealed ductile dimples adjacent to the main fracture surface, contrasting with brittle cleavage areas, as shown in Figure 3.12. This contrast suggests that the failure initiated in brittle regions due to hydrogen embrittlement and propagated until the final stages, where localized ductility emerged in isolated areas.

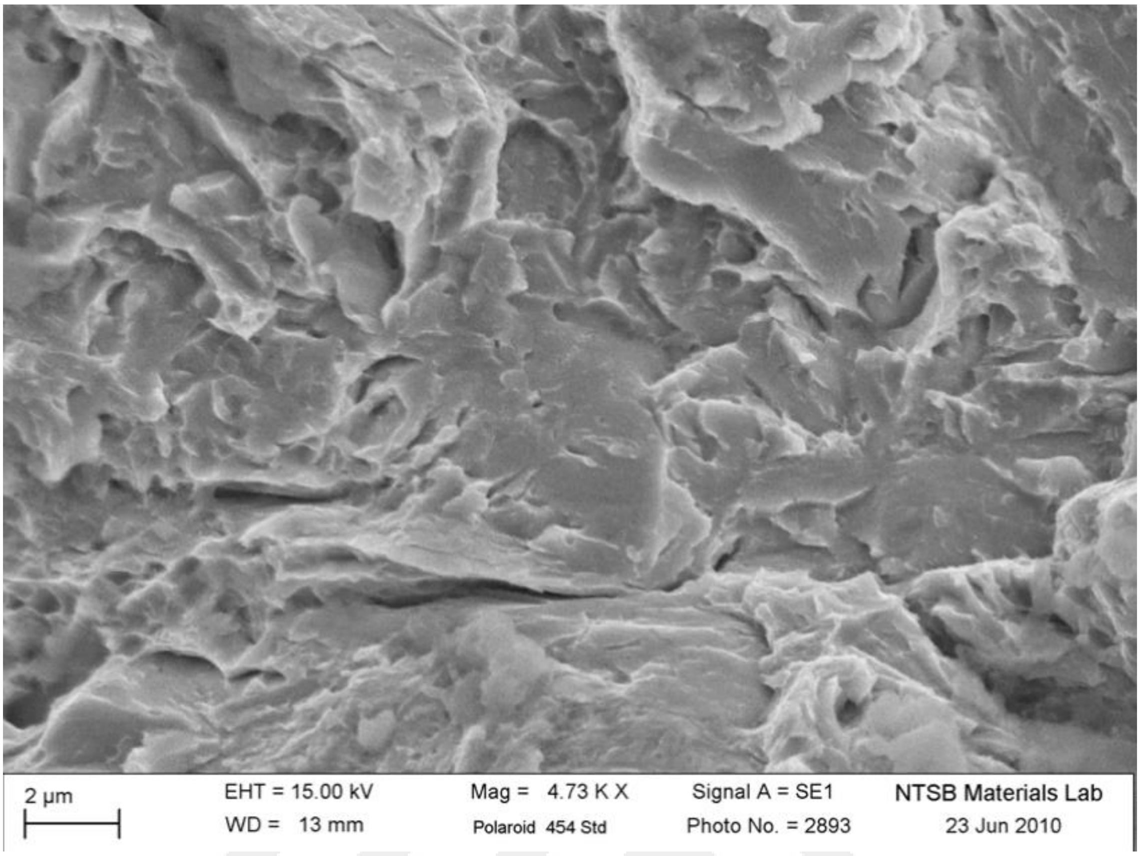

Figure 3.12 Higher magnification SEM image showing the transition between brittle cleavage and ductile dimples on the A-side drive pin fracture surface [211].

These findings highlight the urgent need for strict hydrogen control during the manufacturing and maintenance of aviation components. The incident involving the Bell 222U helicopter emphasizes the importance of comprehensive post-treatment procedures, such as baking after cadmium plating, to effectively remove absorbed hydrogen. Without these precautions, residual hydrogen can significantly weaken high-strength materials, potentially resulting in catastrophic failures in critical aerospace systems.

3.3.3 Failure of the Piper PA-32R-301T (IAD02FA091)

On September 8, 2002, a Piper PA-32R-301T experienced a catastrophic engine failure while cruising at 3,500 feet above Byram Township, New Jersey. The aircraft, operated by a private pilot, experienced a total loss of engine power due to the failure of the crankshaft gear retaining bolt, forcing a crash landing in a wooded area. The impact destroyed the aircraft, resulting in the deaths of the pilot and one passenger, with two others seriously injured.

Investigations identified the failed crankshaft gear bolt (part number STD-2209, SAE J429 grade 8 steel) as the root cause. Metallurgical analysis revealed hydrogen embrittlement as the primary failure mechanism. This condition was traced to residual hydrogen introduced during the zinc electroplating process. Unlike cadmium-plated bolts traditionally used, the substituted zinc-plated bolts lacked effective post-treatment baking, a critical step to mitigate hydrogen absorption. Figure 3.13 shows the disassembled crankshaft assembly, highlighting the fractured bolt.

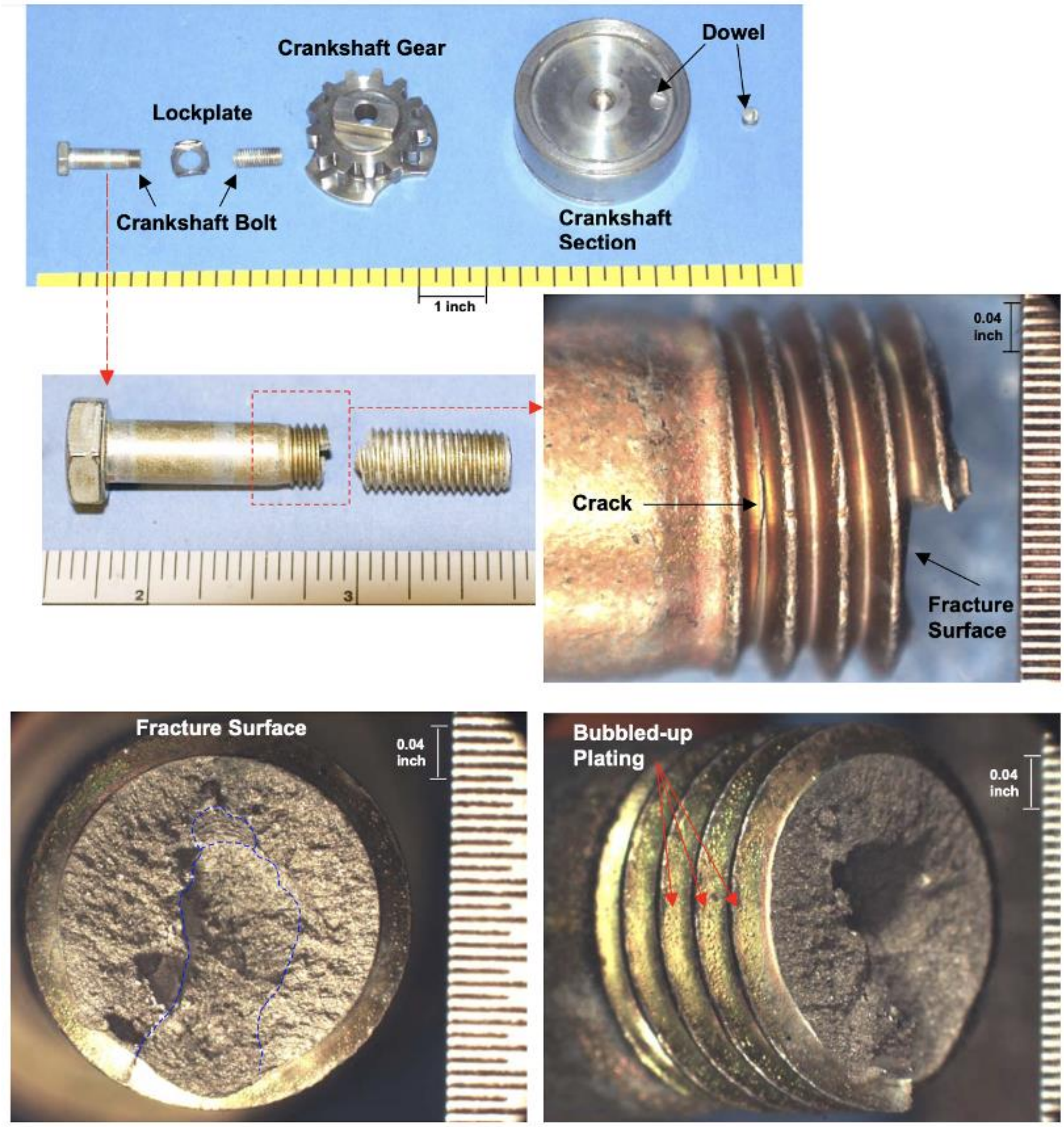

Figure 3.13 Image of the crankshaft assembly and fractured crankshaft gear retaining bolt after disassembly [212].

Scanning Electron Microscopy (SEM) provided insights into the failure mode, as illustrated in Figure 3.14. The fracture surface exhibited intergranular cracking and ductile failure patterns, hallmarks of hydrogen-assisted cracking. The fracture originated at the thread roots and propagated radially due to accumulated hydrogen, compromising the bolt's integrity.

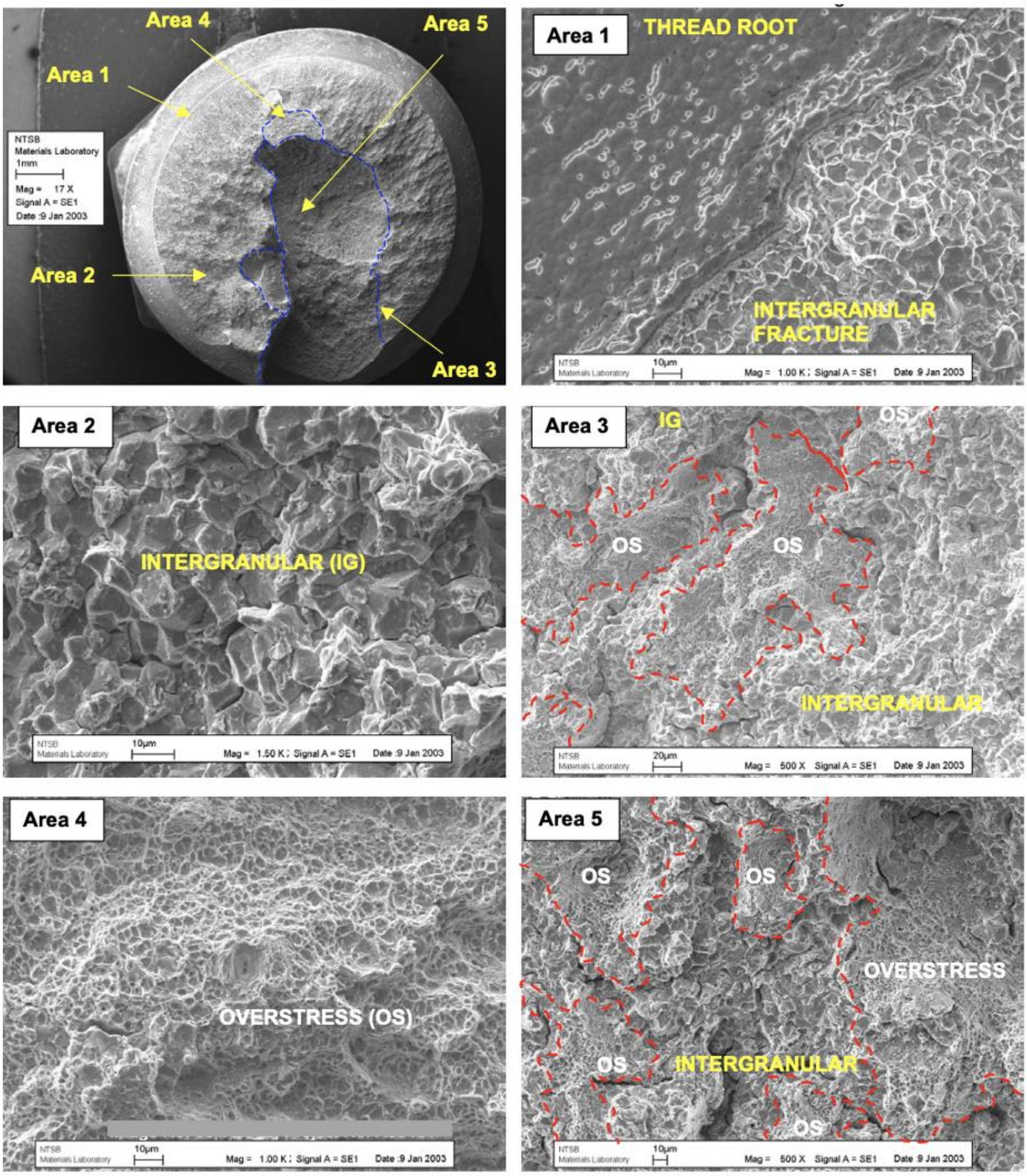

Figure 3.14 SEM image showing intergranular cracking along the fracture surface of the crankshaft bolt, indicating hydrogen-assisted cracking [212].

The problem of hydrogen embrittlement in zinc-plated bolts had been flagged earlier by Lycoming Engines following similar failures in O-540-F1B5 engines used in Robinson R44 helicopters. In response to these failures, Lycoming issued Special Service Advisory No. 48-798, mandating the replacement of zinc-plated bolts after limited operation hours. Despite these warnings, the substitution of cadmium with zinc-plated bolts persisted, leading to repeated incidents, including the Piper PA-32R-301T crash.

This case underscores the critical need for robust post-plating treatments, such as baking, to eliminate residual hydrogen effectively. It also highlights the importance of continuous monitoring and material verification, especially for high-stress components. In response to this incident, the FAA issued an emergency Airworthiness Directive requiring the immediate replacement of zinc-plated crankshaft gear bolts to prevent similar failures.

3.3.4 Failure of the Piper PA-32R-301 (MIA02LA108)

On June 7, 2002, a Piper PA-32R-301 suffered a catastrophic engine failure during a training flight near Key Field in Meridian, Mississippi. Operated by a private pilot, the aircraft experienced a sudden engine failure at 500-600 feet altitude, resulting in an emergency landing attempt. Unfortunately, the aircraft impacted a field and trees, overturning upon landing. The pilot sustained severe injuries, and the aircraft was destroyed. Figure 3.15 illustrates the wreckage following its recovery.

Figure 3.15 Front view of the aircraft wreckage after recovery at Meridian Aviation [213].

Subsequent investigation identified the failure of the crankshaft gear bolt (part number STD-2209) in the Lycoming IO-540-K1G5 engine (Serial No: L-25968-48A) as the primary cause. Examination revealed the bolt fractured between the second and fifth threads from the shank (Figure 3.16), with secondary cracks found at the 12th and 13th threads. The fracture was attributed to hydrogen embrittlement—a failure mechanism exacerbated by inadequate post-plating baking after zinc electroplating. This process allowed hydrogen to remain trapped, leading to material weakening and intergranular cracking.

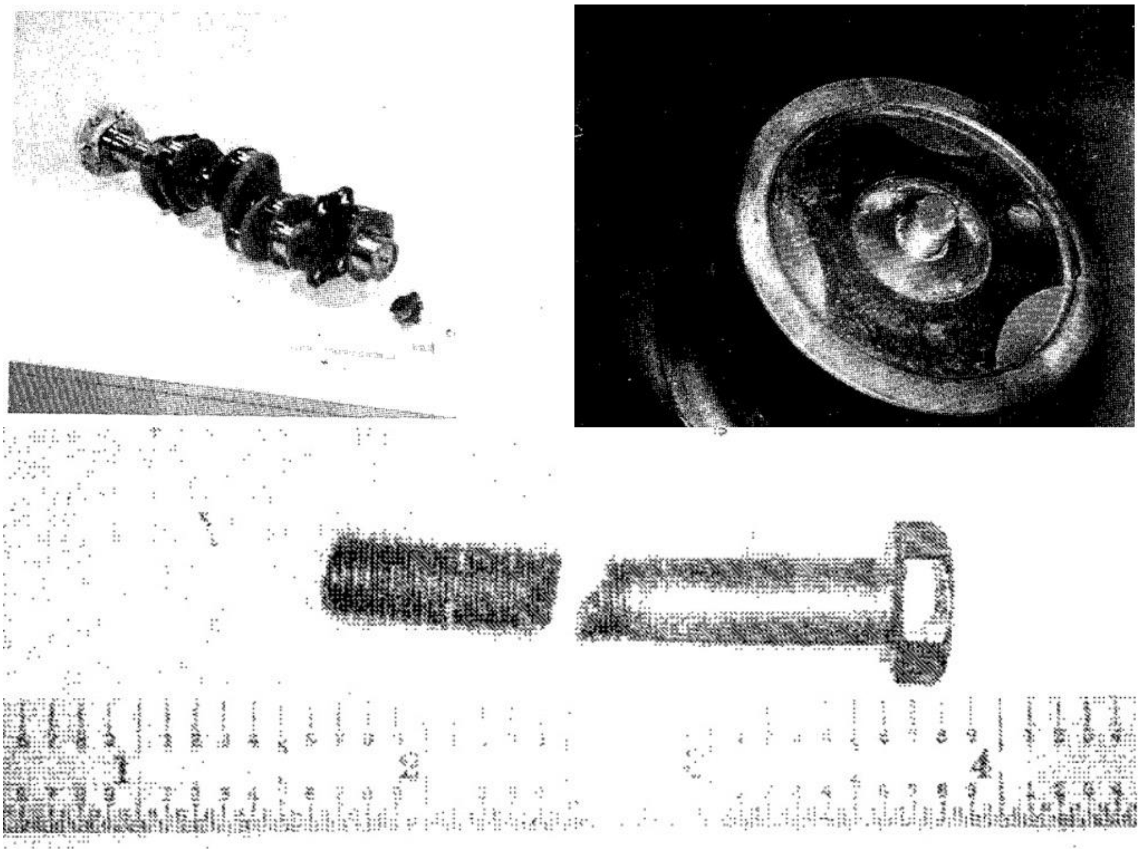

Figure 3.16 Image of the disassembled engine components, highlighting the fractured crankshaft gear bolt [213].

A thorough investigation of the crankshaft gear bolt failure by the Lycoming Materials Laboratory identified hydrogen embrittlement as the root cause. The bolt fractured primarily between the second and fifth threads from the shank, with additional cracks extending through the twelfth and thirteenth threads. These fractures exhibited intergranular separation, a distinct characteristic of hydrogen-assisted cracking. Figure 3.17 provides a detailed SEM image, highlighting the intergranular separation indicative of hydrogen embrittlement.

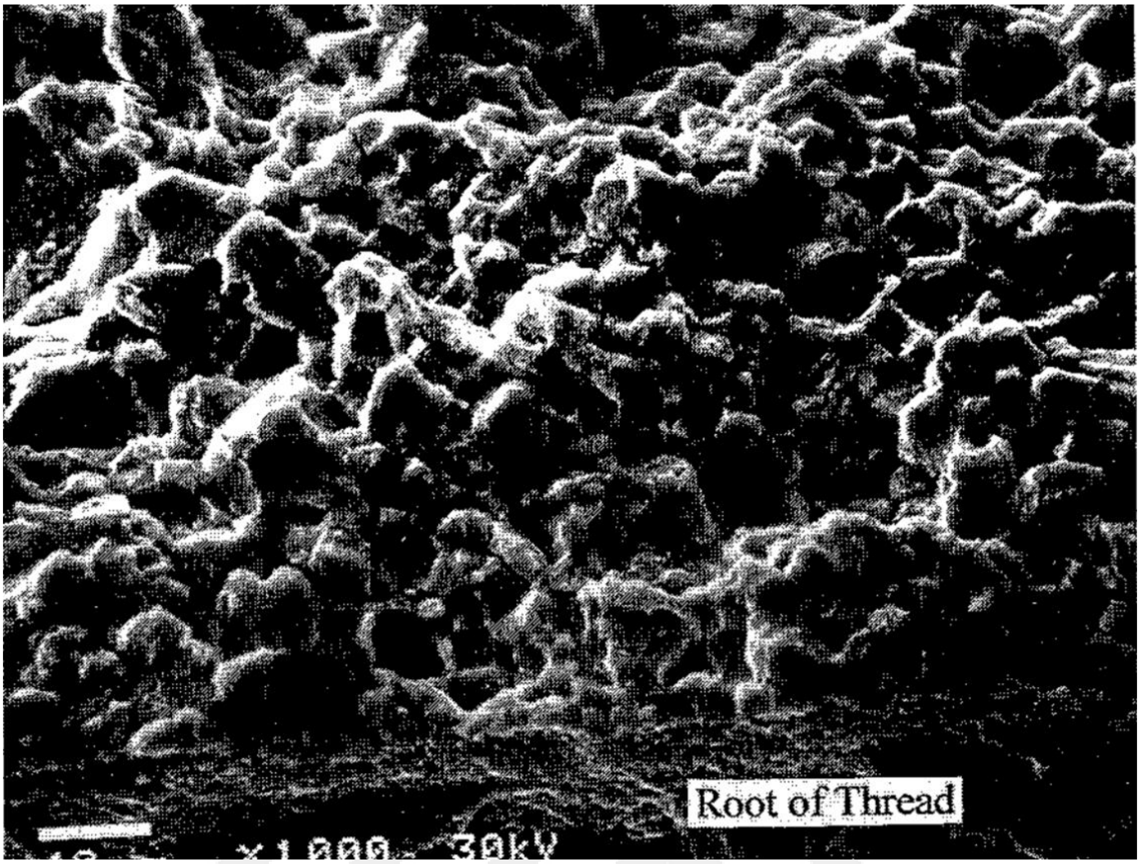

Figure 3.16 SEM image under 1000x magnification showing intergranular separation on the fractured surface of the crankshaft gear bolt, indicating hydrogen-assisted cracking [213].

The hydrogen embrittlement was traced to the zinc electroplating process, which introduced hydrogen into the bolt material. Despite conforming to specifications for hardness and coating thickness, the inadequate post-plating dehydrogenation treatments allowed residual hydrogen to remain, compromising the bolt's structural integrity. This residual hydrogen accumulated at the grain boundaries under operational stresses, leading to the initiation and propagation of cracks.

The bolt failure set off a cascade of damage, including rotational fatigue, that caused secondary damage to the gear and dowel components. This failure ultimately resulted in the separation of the crankshaft gear, leading to a complete loss of engine power. The investigation concluded that the manufacturing process lacked sufficient quality control, specifically in post-plating procedures aimed at eliminating hydrogen.

This incident underscores the critical need for stringent post-plating baking heat treatments to effectively remove hydrogen from plated components. Furthermore, it highlights the necessity of regular inspections for early detection of material degradation, particularly in components subjected to cyclic loading. The findings emphasize the importance of implementing robust quality assurance protocols and industry-standard practices for hydrogen mitigation in aviation manufacturing.

3.3.5 Failure of the Center Landing Gear on FedEx MD-11 (ENG08IA025)

On April 27, 2008, during a routine pre-flight inspection at Singapore Changi Airport (SIN), hydraulic fluid was discovered near the center landing gear (CLG) strut of a FedEx MD-11 aircraft. A detailed examination revealed a 33-inch longitudinal crack on the aft side of the CLG strut cylinder. The crack's presence prompted the removal of the CLG strut for teardown and analysis, which was carried out at the Boeing Southern California Materials Laboratory. The strut had accumulated 5,058 cycles since its last installation on February 22, 2001, with a total lifetime of 9,379 cycles. Figure 3.17 shows the initial findings, highlighting the visible crack.

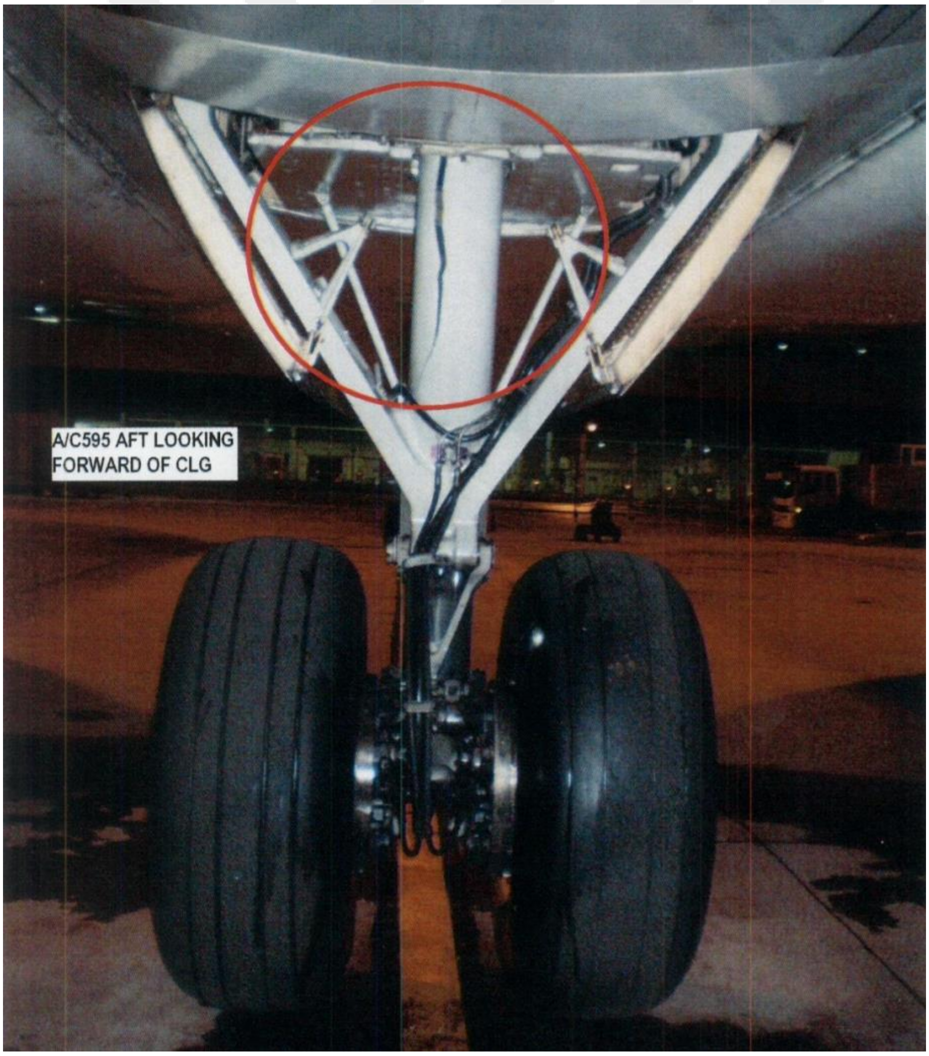

Figure 3.17 Photograph of the cracked CLG strut cylinder, showing the longitudinal crack along the aft side [214].

Metallurgical analysis confirmed that the failure was due to intergranular cracking, which originated from surface contamination introduced during a prior maintenance procedure. The contamination resulted from improper cleaning before the application of paint. Residual chemicals from paint removal solutions contributed to hydrogen embrittlement, causing the intergranular cracking to propagate through the cylinder wall and compromise its structural integrity. A cross-sectional view (Figure 3.18) of the fracture origin highlights the intergranular cracking and subsequent progression.

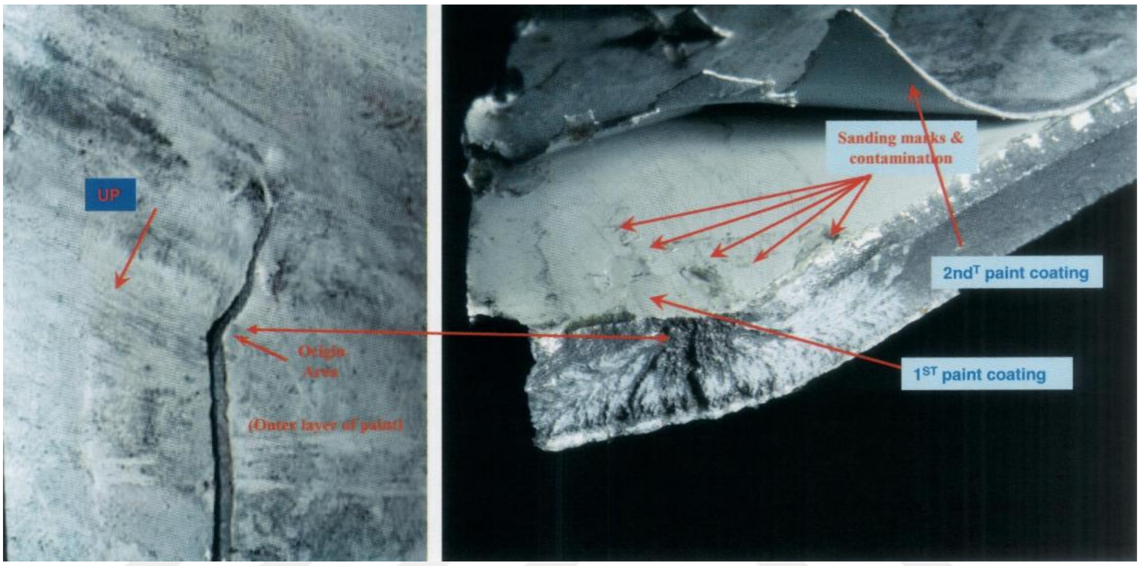

Figure 3.18 Cross-sectional view of the CLG strut cylinder, showing the intergranular cracking that initiated the failure [214].

Teardown observations indicated high residual stresses in the material. While cutting the cylinder, loud "bangs" were reported, revealing further crack propagation due to residual stresses. Scanning Electron Microscope (SEM) analysis (Figure 3.19) provided evidence of mixed-mode failure. The fracture surface exhibited intergranular separation at the origin and dimpled rupture in other areas, which is characteristic of ductile overload failure.

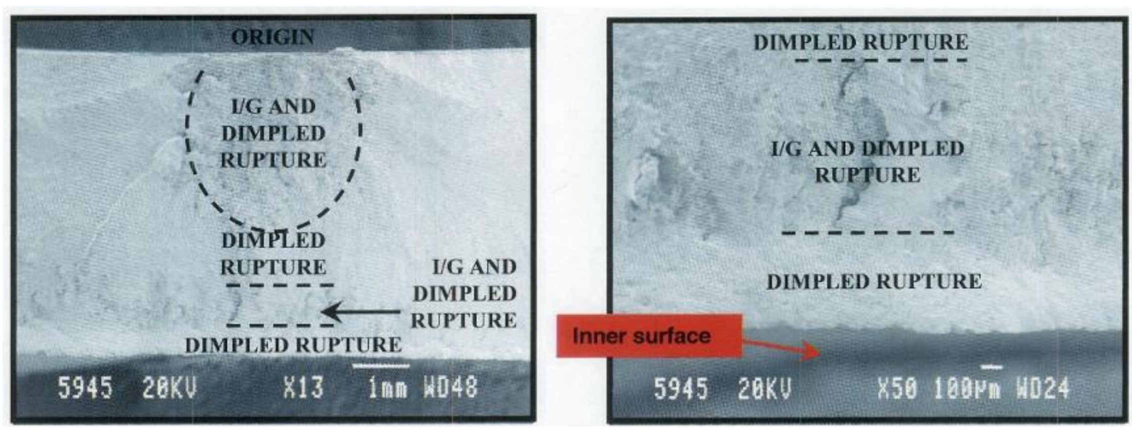

Figure 3.19 SEM image of the fracture surface, showing a combination of intergranular cracking and ductile overload [214].

Further inspection revealed sanding and paint repair marks in the region of failure. Surface sanding likely introduced contamination, and the hydrogen absorbed during the cleaning and painting process contributed to the intergranular cracking. The primary fracture was traced to this contaminated region, approximately 18.2 inches from the bottom of the cylinder. This failure underscores the critical importance of proper surface treatments and material handling during maintenance. The hydrogen embrittlement was caused by contamination from cleaning agents, combined with operational stresses.

3.4 Conclusions and Recommendations

HE presents a unique challenge in aviation, particularly in high-strength components that operate under cyclic stress and are exposed to environmental hydrogen. This review, grounded in specific incident analyses, underscores the critical need for enhanced material science solutions, improved manufacturing protocols, and proactive maintenance strategies.

To enhance safety and operational reliability in the aviation industry, it is essential to focus on the development of hydrogen-resistant alloys specifically designed for aerospace applications. These advanced materials, such as titanium and steel alloys with superior hydrogen tolerance, are crucial for reducing susceptibility to embrittlement. Innovations like nanotechnology-based coatings provide promising pathways for improving resistance to hydrogen diffusion, ensuring the durability of components exposed to high-stress conditions.

Predictive modeling and simulation technologies, such as finite element analysis (FEA) and multi-scale modeling, have proven to be invaluable tools in understanding and mitigating hydrogen embrittlement. These techniques offer a deeper insight into hydrogen diffusion patterns and their impact on material microstructures, enabling the design of next-generation aircraft components that are both lightweight and resistant to HE.

Incident reports analyzed in this study highlight the importance of stringent post-manufacturing treatments, such as baking after electroplating, to eliminate residual hydrogen and mitigate risks. The relatively small number of Airworthiness Directives (ADs) related to hydrogen embrittlement—12 out of 167,751 total ADs issued by the FAA—underscores the need for vigilant monitoring and targeted interventions. These cases, while limited in number, emphasize the disproportionate impact that hydrogen embrittlement can have on aviation safety.

Looking forward, collaboration among materials scientists, aerospace engineers, and regulatory authorities is essential for addressing HE challenges. Additive manufacturing, real-time monitoring, and hydrogen-resistant materials represent promising avenues for future research and development. As the aviation industry transitions towards hydrogen-based propulsion systems, robust storage, and transportation solutions must also be developed to prevent embrittlement risks.

In conclusion, the aviation sector must embrace a multidisciplinary approach to combat hydrogen embrittlement, combining advanced materials, state-of-the-art detection tools, and robust regulatory frameworks. These efforts will not only safeguard against HE-induced failures but also support the shift toward sustainable and resilient aviation technologies in the decades ahead.

Chapter 4

Strain Rate and Post Processing Effect on Mechanical Properties of Additively Manufactured AlSi10Mg Alloys

The mechanical properties of AlSi10Mg alloy fabricated by Selective Laser Melting (SLM) were investigated under different strain rates and post-processing conditions, including shot peening (SP) and stress relief (SR). Tensile tests were performed at quasi-static (10^{-1} s^{-1}) and dynamic ($15 \cdot 10^{-3}$ s^{-1}) strain rates on as-built and post-processed specimens. The results revealed that SP significantly increased tensile strength, reaching up to 415 MPa under dynamic loading, by inducing compressive residual stresses that enhanced surface hardness and delayed crack initiation. SR improved ductility, with elongation at break reaching 15.30%, by reducing internal stresses and stabilizing the microstructure. The combination of SP and SR exhibited a synergistic effect, achieving a balance between strength and ductility, with strain rate sensitivity (m) values confirming improved material performance under dynamic conditions. These findings underscore the potential of post-processing techniques in tailoring the mechanical behavior of SLM-produced AlSi10Mg alloys. The balanced properties achieved through combined treatments make this material particularly suitable for high-performance aerospace and automotive applications, where strength and ductility are critical under varying operational conditions.

4.1 Introduction

Additive Manufacturing (AM), particularly Selective Laser Melting (SLM), has revolutionized the production of complex and high-performance metallic components, offering unprecedented design flexibility and material efficiency [69,215,216]. Among various alloys processed through AM, AlSi10Mg has garnered significant attention due to its excellent combination of lightweight, high strength, corrosion resistance, and processability [217,218]. These attributes make AlSi10Mg a material of choice for critical applications in the automotive and aerospace industries, where structural integrity and material efficiency are paramount. The rapid cooling rates inherent in SLM processes result in ultrafine microstructures, enabling superior mechanical properties compared to traditional manufacturing methods. This fine microstructure, characterized by a cellular network of silicon particles, contributes to enhanced strength and hardness while maintaining adequate ductility, a balance critical for demanding industrial applications [219,220]. While the inherent microstructure of SLM-processed AlSi10Mg contributes to its mechanical performance, the presence of residual stresses and surface defects necessitates effective post-processing techniques to unlock its full potential [221,222].

Extensive research has explored the mechanical behavior of AM-processed AlSi10Mg, particularly under static and dynamic loading conditions, with several studies shedding light on its strain rate sensitivity and microstructural characteristics. Rosenthal et al. [223] demonstrated that strain rate significantly affects the flow stress and strain-hardening behavior of SLM AlSi10Mg, revealing unique fracture mechanisms not observed in conventionally manufactured alloys. Salandari Rabori et al. [224] observed a non-linear strain rate sensitivity in as-built LPBF AlSi10Mg, with the strain rate dependence being more pronounced in compression, linked to its fine, non-equilibrium microstructure. Ghisi et al. [225] found that while SLM AlSi10Mg exhibits low strain rate sensitivity, elongation to failure increases with strain rate, and dynamic loading induces localized microstructural changes near fracture surfaces due to adiabatic heating.

Maleki et al. [226] highlighted the effectiveness of shot peening in enhancing fatigue life by introducing compressive residual stresses and closing subsurface pores, whereas Brandl et al. [218] showed that post-build heat treatments significantly improve high-cycle fatigue resistance by reducing surface roughness and homogenizing microstructures. Zhang et al. [227] demonstrated that fatigue performance is highly dependent on defect size, location, and building direction, with 0° specimens exhibiting superior fatigue resistance compared to other orientations due to reduced defect density. Despite these findings, which primarily focus on fatigue properties after shot peening, gaps remain in understanding the strain rate sensitivity of post-processed AlSi10Mg, particularly under quasi-static (10^{-1}) and dynamic (10^{-3}) strain rate regimes.

Post-processing techniques such as shot peening (SP) and stress relief (SR) have proven to significantly enhance the mechanical properties and mitigate inherent defects in AM-processed AlSi10Mg alloys [84,89,228,229]. Maamoun et al. [91] demonstrated that SP with glass beads improved surface roughness, refined the microstructure through dynamic precipitation of nanoscale silicon particles, and introduced compressive residual stresses, resulting in increased fatigue strength and surface hardness. Uzan et al. [93] highlighted that SP not only enhanced fatigue resistance by relocating crack initiation sites deeper into the material but also increased hardness through localized plastic deformation. Similarly, Damon et al. [230] observed a 15-30% reduction in near-surface porosity post-SP, coupled with significant improvements in both low- and high-cycle fatigue performance. Stress relief, on the other hand, has been shown to complement these effects by homogenizing residual stresses and alleviating surface-induced microcracks, as noted by Wagner and Mueller, who reported substantial improvements in fatigue life when SP was followed by SR [92]. Miao et al. [139] provided further insights into optimizing SP parameters, finding that higher shot velocities enhanced the compressive residual stress profiles and material toughness. Understanding the combined effects of SP and SR on the strain rate-dependent behavior of AlSi10Mg is critical for components subjected to dynamic loading in aerospace and automotive industries, where operational conditions often involve complex strain rates. While these advancements underscore the effectiveness of SP and SR in improving static and fatigue properties, their combined impact on strain rate-dependent mechanical behavior remains largely unexplored, warranting further investigation to optimize these treatments for dynamic applications.

This study aims to bridge these gaps by systematically investigating the influence of SP and SR on the tensile and fatigue behavior of SLM AlSi10Mg under varying strain rate conditions. By correlating post-process-induced microstructural changes with mechanical performance across quasi-static and dynamic regimes, this research seeks to provide a deeper understanding of how to optimize post-processing techniques for high-performance applications. The findings of this work will contribute to advancing the adoption of AM-processed AlSi10Mg in safety-critical industries, offering insights into its behavior under complex operational conditions and paving the way for enhanced material design and process optimization.

4.2 Materials and Methods

4.2.1 Specimen Fabrication

The AlSi10Mg specimens for this study were fabricated using Selective Laser Melting (SLM) technology on an EOS M 290 machine. Key processing parameters included a laser power of 370 W, a scanning speed of 1300 mm/s, a hatch spacing of 0.19 mm, and a layer thickness of 30 µm. The energy density was set at 49.932 J/mm³ to optimize melting conditions. To enhance structural uniformity and reduce residual stresses, an X-rotated scanning strategy was employed, which is widely adopted in aerospace and automotive industries. The build platform was preheated to 35°C to improve interlayer bonding and minimize thermal gradients during fabrication.

The AlSi10Mg powder used for fabrication had a particle size range of 25–70 µm and conformed to the DIN EN 1706 (EN AC-43000) standard. The detailed chemical composition of the powder is presented in Table 4.1. This optimized setup resulted in specimens with fine microstructures, reduced porosity, and inherent residual stresses, characteristic of SLM-processed components.

Table 4.6 Powder chemical composition (wt.-%)

Element	Al	Si	Fe	Cu	Mn	Mg	Ni	Zn	Pb	Sn	Ti
Comp. (wt.-%)	87.2-89.4	9 - 11	0.55	0.05	0.45	0.25-0.45	0.05	0.10	0.05	0.05	0.05

Specimens were prepared in a flat dog-bone geometry, with dimensions as shown in Figure 4.1, designed to ensure compatibility with tensile testing according to ASTM E8/E8M standards. The gauge length was 10 mm, the width was 3 mm, and the thickness was 1.5 mm. The workflow for the production and preparation of the specimens followed a standardized protocol to ensure consistency and reproducibility across all samples.

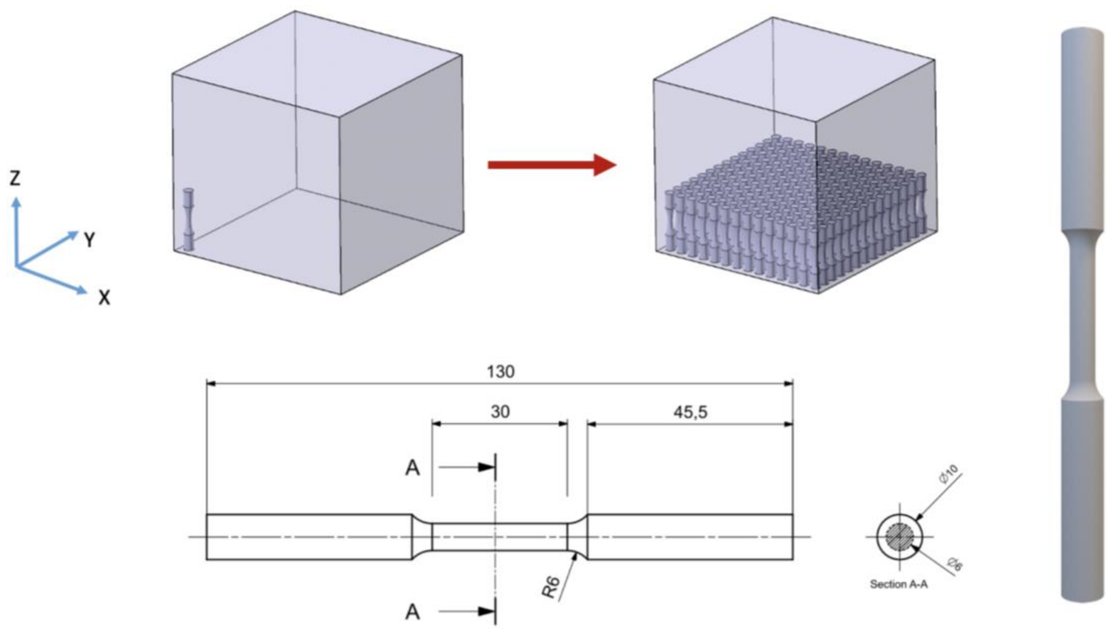

Figure 4.3 Sample Drawings and Production Workflow for Additive Manufacturing

4.2.2 Post-Process Treatments

To investigate the effects of post-processing on mechanical performance, two key techniques were applied: shot peening (SP) and stress relief (SR).

Shot Peening was performed using high-velocity steel balls (ASR170) in a Wheelabrator MP 1000 system. The process adhered to the SAE AMS2430 standard, with an intensity of 0.25 mmA. This treatment introduced a compressive residual stress layer on the surface, enhancing fatigue resistance and mitigating crack initiation tendencies.

Stress Relief heat treatment was conducted to reduce internal residual stresses induced by the SLM process. This was achieved by partially annealing the specimens at a temperature range of 333–349°C for 0.5 hours, followed by air cooling, in accordance with the AMS2770 standard. This process stabilized the microstructure and reduced stress concentration sites.

4.2.3 Mechanical Testing

Tensile tests were conducted at room temperature using an INSTRON 5985 electromechanical universal testing machine up to 300 kN load cell capacity equipped with Instron Dynamic extensometer, 25 mm gage length to ensure precise strain measurements. All tests have been carried out with a preload value of 1 kN to ensure stability of the specimen, 70 bar grip pressure applied, and load and strain values have been balanced prior to test initiation. The tests evaluated key mechanical properties, including ultimate tensile strength, yield strength, and elongation at fracture. Comparative analysis was performed on untreated, shot-peened (SP), and stress-relieved (SR) specimens under quasi-static (10^{-1} s^{-1}) and dynamic ($15 \cdot 10^{-3}$ s^{-1}) strain rate conditions. The results provided a comprehensive understanding of how post-processing techniques influence the strain rate sensitivity and fracture behavior of AlSi10Mg.

4.3 Results and Discussions

The mechanical behavior of AlSi10Mg under different strain rates (10^{-1} and $15 \cdot 10^{-3}$ s^{-1}) and post-processing conditions was systematically analyzed through force-displacement and true stress-strain curves. The results highlight a significant dependency on both the applied strain rate and post-processing treatments, such as shot peening (SP) and stress relief (SR).

Figure 4.2 illustrates the force-displacement curves for the tested specimens. The AL-SP specimens demonstrated the highest maximum force values across all strain rates, underscoring the role of shot peening in enhancing surface strength by inducing compressive residual stresses. The AL-SR specimens also exhibited higher displacement capacities, reflecting their improved ductility. Interestingly, the AL-SR-SP specimens, subjected to both SP and SR treatments, displayed a balanced performance, combining moderate strength with enhanced displacement, which aligns with the synergistic benefits of these two post-processing techniques. These trends emphasize the trade-off between maximum force and displacement capacity across the different treatments.

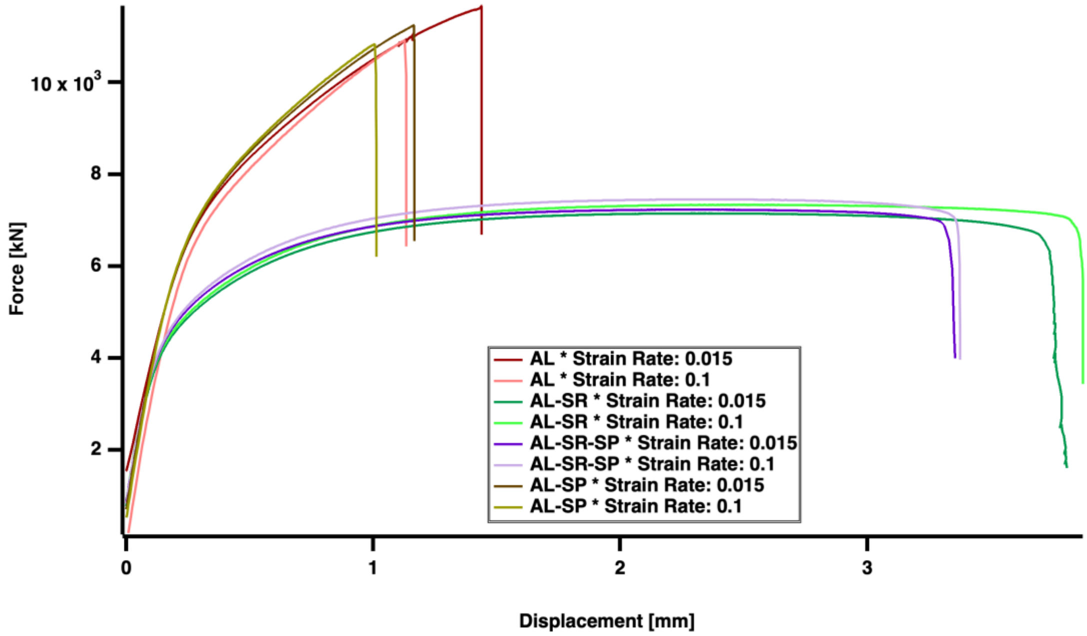

Figure 4.2 Force-Displacement curves for AlSi10Mg specimens under different post-processing treatments (AL, AL-SP, AL-SR, AL-SR-SP) and strain rates (10^{-1} and $15 \cdot 10^{-3}$ s^{-1}).

The true stress-strain curves, shown in Figure 4.2, further highlight the impact of post-processing and strain rate. AL-SP specimens exhibited the highest tensile strength (Rm), reaching up to 415 MPa under dynamic loading conditions ($15 \cdot 10^{-3}$ s^{-1}). This improvement aligns with previous studies, such as those by Maamoun et al. (2018) [91] and Damon et al. (2018) [230], which demonstrated the effectiveness of SP in improving surface hardness and mitigating subsurface defects, thereby increasing the material's overall load-bearing capacity. On the other hand, AL-SR specimens showed significantly increased ductility, with elongation at break reaching 15.30% at a quasi-static strain rate (10^{-1} s^{-1}). This behavior is attributed to the stress relief treatment, which reduces internal residual stresses and stabilizes the microstructure, as also reported by Wagner et al. (2011) [231]. The AL-SR-SP specimens offered a combination of these benefits, achieving a balance between strength and ductility, which makes them particularly suitable for dynamic applications.

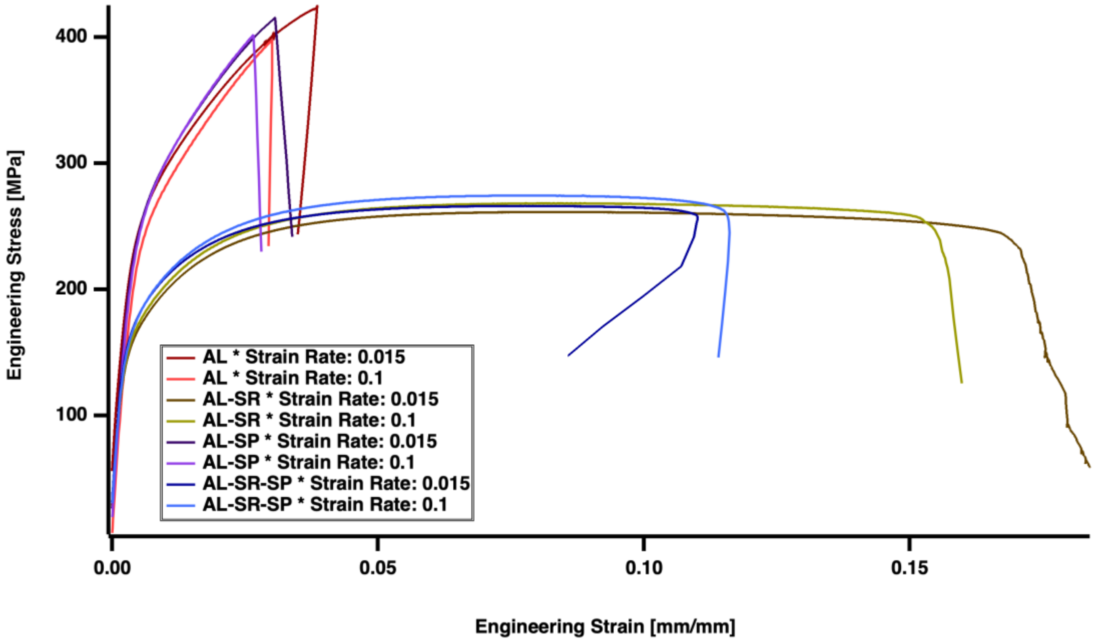

Figure 4.3 Engineering Stress-Engineering Strain curves for AlSi10Mg specimens under different post-processing treatments (AL, AL-SR, AL-SP, AL-SR-SP) and strain rates (10^{-1} and $15 \cdot 10^{-3}$ s^{-1}).

Figure 4.3 illustrates the engineering stress-engineering strain behavior of AlSi10Mg alloy specimens under different post-processing treatments and strain rates. Higher strain rates (10^{-1} s^{-1}) led to increased tensile strength but reduced elongation at break, particularly in AL-SP specimens, reflecting the strengthening effect of shot peening, which achieved stress values exceeding 400 MPa. This behavior reflects the strengthening effect of shot peening, consistent with Rosenthal et al. (2017) [223], who reported enhanced flow stress and strain hardening at higher strain rates for SLM-processed AlSi10Mg. Conversely, lower strain rates ($15 \cdot 10^{-3}$ s^{-1}) improved ductility, especially in AL-SR and AL-SR-SP specimens, where stress relief played a significant role in stabilizing the microstructure and promoting uniform deformation. Stress-relieved specimens exhibited elongation at break exceeding 0.15 mm/mm, confirming their superior ductility, while combined treatments (AL-SR-SP) demonstrated balanced properties, offering moderate strength with improved elongation. These trends emphasize the synergistic effects of SP and SR treatments in optimizing mechanical behavior for different loading conditions.

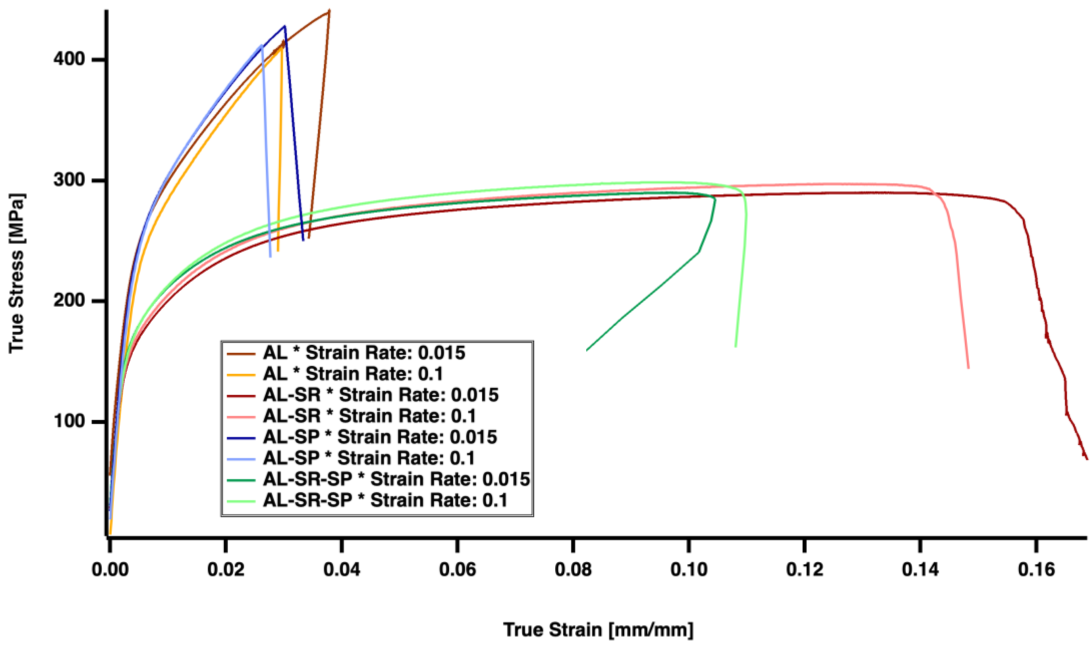

Figure 4.4 True Stress-True Strain curves for AlSi10Mg specimens under different post-processing treatments (AL, AL-SP, AL-SR, AL-SR-SP) and strain rates (10^{-1} and 15 • 10^{-3} s^{-1}).

The true stress-strain curves, shown in Figure 4.4, further highlight the impact of post-processing and strain rate. AL-SP specimens exhibited the highest tensile strength, reaching up to 415 MPa under dynamic loading conditions (15 • 10^{-3} s^{-1})., demonstrating the pronounced strain-hardening effect induced by shot peening. This improvement aligns with previous studies, such as those by Maamoun et al. (2018) [91] and Damon et al. (2018) [230], which demonstrated the effectiveness of SP in improving surface hardness and mitigating subsurface defects, thereby increasing the material's overall load-bearing capacity. However, AL-SP specimens showed reduced elongation at break, reflecting embrittlement from surface hardening. On the other hand, AL-SR specimens showed significantly increased ductility, with elongation at break reaching 15.30% at a quasi-static strain rate (10^{-1}), attributed to the stress relief treatment, which reduces internal residual stresses and stabilizes the microstructure. These specimens exhibited more uniform deformation, with extended strain values and reduced strain hardening. The AL-SR-SP specimens offered a combination of these benefits, achieving a balance between strength and ductility, which makes them particularly suitable for dynamic applications. Notably, strain rate influenced all specimens, with higher rates increasing tensile strength but reducing true strain at failure, while lower rates promoted more uniform deformation.

Table 4.2 summarizes the key mechanical properties of the tested specimens, including Young's modulus, tensile strength, and elongation at break. AL-SP specimens exhibited superior tensile strength values, consistent with the strengthening effect of shot peening. Stress-relieved samples, on the other hand, showed the highest elongation at break, highlighting their ductility-enhancing effects. The combined AL-SR-SP specimens achieved intermediate values, reflecting the complementary effects of SP and SR in optimizing the mechanical properties of AlSi10Mg alloys.

Table 4.7 Specimens' tensile test results

Specimen	Strain Rate [s^{-1}]	Maximum Force [kN]	Tensile stress at Yield (Offset 0.2 %) [MPa]	Ultimate Tensile Strength (Rm) [MPa]	Young's Modulus [GPa]	% Non-proportional elongation (at break) [%]	Plasticity Index [%]
AL	10^{-1}	11	233.04	401	62.39	2.27	2.07
AL	$15 \cdot 10^{-3}$	12	246.48	418	58.78	2.94	2.74
AL-SR	10^{-1}	7	163.94	268	65.68	15.30	15.1
AL-SR	$15 \cdot 10^{-3}$	7	161.26	260	66.73	13.25	13.05
AL-SP	10^{-1}	11	249.59	402	66.66	1.86	1.66
AL-SP	$15 \cdot 10^{-3}$	11	251.06	415	66.04	2.26	2.06
AL-SR-SP	10^{-1}	7	170.93	274	65.20	11.11	10.91
AL-SR-SP	$15 \cdot 10^{-3}$	7	171.12	266	66.27	10.46	10.26

Shot peening (AL-SP specimens) significantly enhanced the tensile strength of AlSi10Mg alloys, achieving the highest values among all conditions, with ultimate tensile strengths of 402 MPa at 0.1 strain rate and 415 MPa at 0.015 strain rate. This improvement is attributed to the surface compressive stresses induced during the peening process, which inhibit crack initiation and propagation, particularly under dynamic loading conditions. The localized strengthening effect is most pronounced in the surface layers, where residual compressive stresses dominate, leading to improved resistance to tensile forces. However, the strengthening comes at a cost: ductility is notably reduced. The elongation at break for AL-SP specimens was the lowest, ranging between 1.86% and 2.26%, indicating embrittlement due to the localized hardening effects of shot peening. The plasticity index, also lower in these specimens (1.66%-2.06%), reflects the limited capacity for plastic deformation before failure. This trade-off makes shot peening ideal for applications requiring high strength and fatigue resistance, albeit with reduced ductility.

Stress relief (AL-SR specimens) primarily improved the ductility of the alloy, with elongation at break reaching 15.30% at 0.1 strain rate and 13.25% at 0.015 strain rate. These values represent the highest ductility among all conditions, showcasing the effectiveness of stress relief in reducing internal residual stresses and stabilizing the microstructure. This treatment promotes uniform deformation and minimizes strain localization, allowing the material to sustain greater plastic deformation without premature failure. However, stress relief reduces tensile strength, with ultimate tensile strength values of 268 MPa at 0.1 and 260 MPa at 0.015. This reduction is attributed to the absence of hardening mechanisms such as surface compressive stresses, which are present in shot-peened specimens. Despite the decrease in strength, stress-relieved specimens maintained the highest plasticity index (15.10%-13.05%), underscoring their capacity for extensive plastic deformation. This makes stress relief suitable for applications where ductility and stability under slow deformation are prioritized, such as structural components subjected to quasi-static loading.

The combined AL-SR-SP treatment provided a balanced outcome, leveraging the benefits of both shot peening and stress relief. While tensile strength (274 MPa at 0.1 and 266 MPa at 0.015) and elongation at break (11.11%-10.46%) were intermediate compared to AL-SP and AL-SR, the treatment effectively optimized the trade-off between strength and ductility. This balance makes the combined treatment particularly attractive for applications requiring both fatigue resistance and plastic deformation capability, such as in dynamic and load-bearing components.

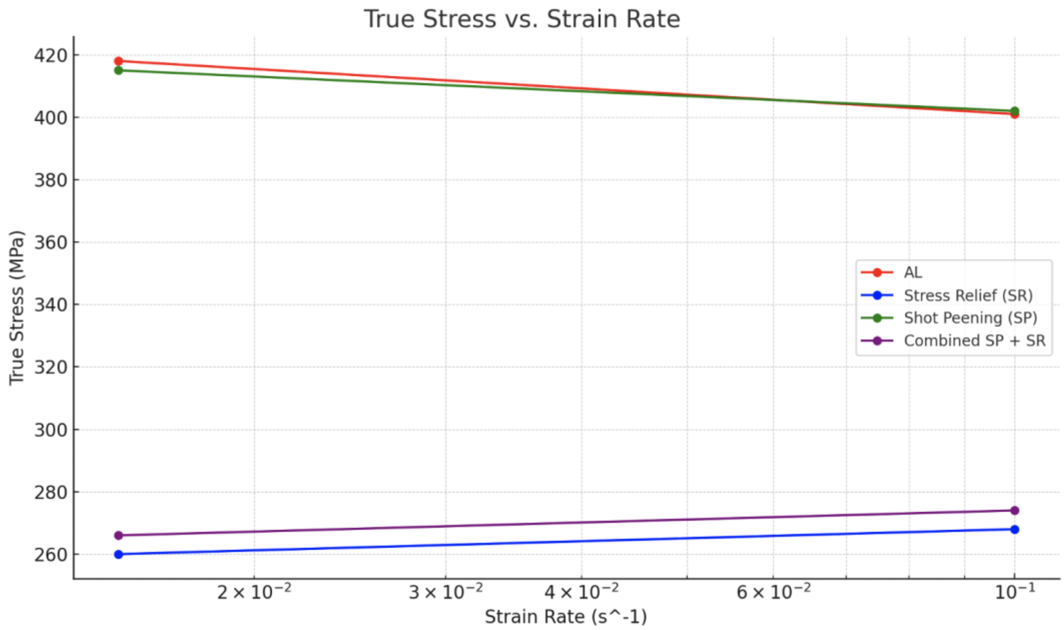

Figure 4.4 Strain rate effect on true stress values on samples

The strain rate effect on true stress values in Figure 4.4 and the strain rate sensitivity (m) values in Table 4.2 provide insight into how the mechanical behavior of AlSi10Mg alloy responds to changes in strain rate. The sensitivity is calculated using the Equation 4.1:

$$m = \frac{\ln(\sigma_2/\sigma_1)}{\ln(\dot{\epsilon}_2/\dot{\epsilon}_1)} \tag{4.1}$$

Where σ_1 and σ_2 true stresses at upper and lower strain rates $\dot{\epsilon}_1$ and $\dot{\epsilon}_2$, respectively.

Table 4.8 Strain rate sensitivity

Specimen	Strain Rate 1 $(\dot{\epsilon}_1)$, [s^{-1}]	Strain Rate 2 $(\dot{\epsilon}_2)$, [s^{-1}]	True Stress 1 (σ_1), [MPa]	True Stress 2 (σ_2), [MPa]	Strain Rate Sensitivity (m)
AL	10^{-1}	$15 \cdot 10^{-3}$	401	418	-0.0219
AL-SR	10^{-1}	$15 \cdot 10^{-3}$	268	260	0.0160
AL-SP	10^{-1}	$15 \cdot 10^{-3}$	402	415	-0.0168

AL-SR-SP (combined)	10^{-1}	$15 \cdot 10^{-3}$	274	266	0.0156

The strain rate sensitivity (m) values highlight the influence of strain rate on the mechanical behavior of AlSi10Mg alloys under different conditions. Positive m values observed in stress-relieved (AL-SR, m =0.0160) and combined (AL-SR-SP, m =0.0156) specimens indicate improved material performance at higher strain rates, attributed to stabilized microstructures and reduced residual stresses. Conversely, negative m values in baseline (AL, m =−0.0219) and shot-peened (AL-SP, m =−0.0168) specimens suggest diminished strain rate sensitivity, likely due to unrelieved residual stresses and dominant surface compressive effects. This behavior may arise from microstructural limitations in the baseline material, where residual stresses and inhomogeneities remain unaddressed, reducing the material's ability to strengthen dynamically. In shot-peened specimens, surface compressive stresses dominate the mechanical response, overshadowing bulk strain-hardening mechanisms. Furthermore, the absence of dynamic strain aging (DSA), as evidenced by the lack of serrated flow in the stress-strain curves, limits the strain rate hardening effect. Instead, the eutectic Si phase facilitates dislocation mobility, further reducing sensitivity. These findings underscore the potential limitations of untreated and surface-hardened conditions for dynamic applications, highlighting the critical role of combined treatments like stress relief and shot peening in achieving balanced and positive strain rate sensitivity suitable for high-performance and dynamic loading scenarios.

These findings are consistent with the existing literature. Studies by Brandl et al. (2012) [218] and Maleki et al. (2023) [226] have shown that shot peening enhances surface hardness and fatigue resistance, while stress relief treatments improve ductility and stabilize mechanical behavior. Furthermore, the strain rate sensitivity observed in this study corroborates the results of Rosenthal et al. (2017) [223] and Salandari Rabori et al. (2022) [224], who reported significant strain rate-dependent behavior for SLM-processed AlSi10Mg alloys, particularly under dynamic loading conditions. These comparisons validate the observed trends and demonstrate the effectiveness of combined SP and SR treatments in tailoring the mechanical properties of AlSi10Mg for high-performance applications.

In conclusion, the mechanical properties of AlSi10Mg alloys are significantly influenced by strain rate and post-processing treatments. Shot peening enhances strength and surface hardness, while stress relief improves ductility and stabilizes the microstructure. The combined SP and SR treatment provides a balanced approach, with positive strain rate sensitivity, making it suitable for demanding applications in the aerospace and automotive industries. These findings offer valuable insights for optimizing post-processing strategies to enhance the performance of additively manufactured AlSi10Mg alloys.

4.4 Conclusions

This study systematically investigated the mechanical behavior of additively manufactured AlSi10Mg alloys under varying strain rates and post-processing treatments, including shot peening (SP), stress relief (SR), and their combination (SP+SR). The results provide key insights into how post-processing and strain rate influence the tensile properties of SLM-fabricated AlSi10Mg, making it suitable for high-performance applications.

The SP treatment enhanced surface strength by inducing compressive residual stresses, leading to the highest tensile strength (up to 415 MPa) under high strain rates ($15 \cdot 10^{-3}$ s^{-1}). Conversely, SR treatments improved ductility, with elongation at break exceeding 15%, attributed to the reduction of internal residual stresses and stabilization of the microstructure. The combination of SP and SR treatments resulted in a balanced mechanical profile, offering moderate tensile performance alongside enhanced ductility—making it advantageous for applications that demand both strength and plastic deformation capacity.

Strain rate sensitivity (m) values highlighted material responsiveness to dynamic loading. Positive m values in stress-relieved and combined treatments indicate improved performance under higher strain rates, while negative m values in untreated and SP-only specimens reflect localized hardening and microstructural limitations. These observations emphasize the synergistic potential of SP and SR to mitigate surface defects and stabilize the bulk microstructure, achieving superior mechanical properties for demanding applications.

These results align with existing literature, corroborating the effectiveness of SP in enhancing surface hardness and fatigue resistance and the role of SR in stabilizing ductility. The outcomes reinforce the applicability of combined treatments for AlSi10Mg in safety-critical sectors, such as aerospace and automotive industries, where high performance under variable loading is crucial. Future investigations should explore cyclic and fatigue behavior to further validate these post-processing strategies under operational conditions.

Chapter 5

Mitigating Hydrogen Embrittlement in Additively Manufactured AlSi10Mg Alloys: The Role of Post-Processing Treatments

Hydrogen embrittlement (HE) poses a critical challenge in high-strength alloys, where hydrogen absorption can significantly reduce ductility and fracture toughness, leading to premature failure. This study investigates the effects of post-processing treatments—specifically, shot peening and stress relief—on the hydrogen embrittlement resistance of AlSi10Mg alloy produced through Selective Laser Melting (SLM). The unique microstructure resulting from SLM, characterized by fine grains, porosity, and residual stresses, renders $AlSi_{10}Mg$ particularly susceptible to hydrogen-induced degradation. Mechanical testing was conducted at two distinct strain rates ($15 \bullet 10^{-3} \times s^{-1}$ and $10^{-1} \times s^{-1}$) to evaluate the material's behavior under both slow and rapid deformation conditions. The results indicate that shot peening effectively enhances the alloy's surface resistance to crack initiation by introducing beneficial compressive residual stresses, while stress relief treatment reduces internal stresses, stabilizing the microstructure and improving overall hydrogen embrittlement resistance. The combined application of shot peening and stress relief demonstrated a significant improvement in mechanical integrity across both strain rates. This study provides insights into optimizing post-processing techniques to enhance the durability of additively manufactured $AlSi_{10}Mg$ alloys in hydrogen-sensitive environments, contributing to the advancement of hydrogen-resistant materials for critical applications in aerospace, automotive, and energy industries.

5.1 Introduction

Hydrogen embrittlement (HE) is a critical failure mechanism in metallic materials, where the diffusion and accumulation of hydrogen atoms within the metal matrix lead to a marked reduction in ductility and fracture toughness [95]. This process is particularly detrimental to high-strength alloys exposed to hydrogen-rich environments, as even minimal hydrogen presence can trigger premature and catastrophic failures under tensile stress [232]. HE arises due to hydrogen atoms gathering at microstructural imperfections like as grain boundaries, voids, and dislocations, which facilitate localized plastic deformation and crack initiation [233–235]. This phenomenon poses substantial risks in industries such as aerospace, automotive, energy, and chemical processing, where high-performance metals are often used in hydrogen-prone environments [168].

With the rising adoption of additive manufacturing (AM), particularly Selective Laser Melting (SLM), for producing complex components from high-performance alloys like AlSi10Mg, Ti6AlV4, 316 L stainless steel, etc., there is an increased need to understand how these processes influence the susceptibility to hydrogen embrittlement [104,236,237]. SLM allows to produce intricate geometries and high-precision parts, but the rapid solidification and cooling rates inherent in SLM create unique microstructures that differ significantly from those of conventionally manufactured alloys. These microstructural features, including fine grains, porosity, and residual stresses, can exacerbate hydrogen embrittlement by providing pathways for hydrogen diffusion and accumulation [238]. $AlSi_{10}Mg$, a widely used aluminum-silicon-magnesium alloy, is particularly valued for its high strength-to-weight ratio and corrosion resistance [239,240]. However, its performance under hydrogen exposure, especially in cyclic or sustained loading conditions, remains underexplored.

To address the heightened risk of hydrogen embrittlement in additively manufactured alloys, several post-processing treatments have been proposed, including shot peening and stress relief. Shot peening, a mechanical surface treatment, introduces compressive residual stresses on the surface by bombarding it with high-velocity steel or ceramic media [92,139]. This treatment has been shown to counteract tensile stresses, which are the primary drivers of crack initiation, and can create hydrogen traps that impede hydrogen diffusion, thus enhancing the material's resistance to fatigue and embrittlement [102,241,242]. While shot peening introduces beneficial compressive stresses on the surface, stress relief reduces internal residual stresses formed during the SLM process, as highlighted by Wilde and Chattoraj (1992) and Lee et al. (2021) [234]. However, the combined effects of these treatments under varying strain rates remain underexplored, particularly for AlSi10Mg alloys exposed to hydrogen-rich environments.

Stress relief, commonly achieved through thermal treatment, is another effective method for mitigating hydrogen embrittlement by addressing internal residual stresses [243]. During the rapid cooling of the SLM process, residual stresses can accumulate within the material, making it more prone to cracking under hydrogen exposure. Stress relief helps to stabilize the microstructure and diminish the driving force for hydrogen-induced cracking by reducing these internal stresses [243–245]. Studies by Lee et al. (2021) have shown that stress relief significantly reduces hydrogen embrittlement susceptibility in additively manufactured alloys, promoting a more homogeneous microstructure and enhancing overall material stability [246].

Despite advances in post-processing techniques, there remains a critical knowledge gap regarding the effects of shot peening and stress relief on hydrogen embrittlement resistance in additively manufactured AlSi10Mg alloys, particularly under varying mechanical loading conditions. A key factor influencing hydrogen embrittlement is strain rate, which affects the interaction between hydrogen diffusion and crack propagation. At lower strain rates (e.g., $15 \cdot 10^{-3}$ s^{-1}), hydrogen atoms have more time to diffuse into the microstructure, leading to a higher risk of embrittlement [121]. Conversely, at higher strain rates (e.g., 10^{-1} s^{-1}), hydrogen diffusion is limited by the rapid deformation rate, but residual stresses from the SLM process can still facilitate crack initiation and propagation [247].

The aim of this study is to investigate the effects of shot peening and stress relief on the hydrogen embrittlement resistance of SLM-produced AlSi10Mg alloys. Mechanical testing was conducted at two distinct strain rates to simulate both slow and rapid deformation, allowing for a comprehensive evaluation of the material's performance under various loading conditions. Our findings demonstrate that shot peening significantly enhances surface resistance to crack initiation through compressive residual stresses, while stress relief reduces internal stresses, thus improving the material's overall stability against hydrogen embrittlement. This research aims to bridge the existing knowledge gap by providing critical insights into optimizing post-processing treatments for additively manufactured components exposed to hydrogen-rich environments, contributing to the development of more robust and durable materials for high-performance applications. This study bridges the gap by exploring the combined application of shot peening and stress relief under varied strain rates, aiming to optimize post-processing treatments for hydrogen-sensitive, additively manufactured components.

5.2 Materials and Methods

This research investigates the hydrogen embrittlement resistance of AlSi10Mg —fabricated through Selective Laser Melting (SLM)—to hydrogen embrittlement. SLM, a high-precision additive manufacturing method, is particularly advantageous for creating geometrically intricate parts. The AlSi10Mg alloy was chosen due to its favorable strength-to-weight characteristics and its prevalent use in aerospace and automotive engineering. The test samples were manufactured using an EOS M 290 SLM machine under carefully controlled parameters: a laser power of 370 W, a scan speed of 1300 mm/s, a hatch distance of 0.19 mm, a layer thickness of 30 microns, and a beam offset of 0.02 mm. An energy density of 49.932 J/mm³ was applied to achieve optimal melting conditions. Furthermore, an X-rotated scanning strategy was employed to enhance structural uniformity, a method widely adopted in industries such as aerospace and medical implants.

The AlSi10Mg powder used in the process had a particle size range of 25–70 µm, with its chemical composition complying with the DIN EN 1706 (EN AC—43000) standard. The detailed powder composition is provided in Table 5.1. To further improve layer bonding and reduce residual stresses, the build platform was preheated to 35°C. These optimized process parameters resulted in specimens exhibiting typical SLM microstructural characteristics, including fine grains, controlled porosity, and inherent residual stresses, all of which play a crucial role in determining the alloy's susceptibility to hydrogen embrittlement.

Table 5.9 Powder chemical composition (wt.-%)

Element	Al	Si	Fe	Cu	Mn	Mg	Ni	Zn	Pb	Sn	Ti
Comp. (wt.-%)	87.2-89.4	9 - 11	0.55	0.05	0.45	0.25-0.45	0.05	0.10	0.05	0.05	0.05

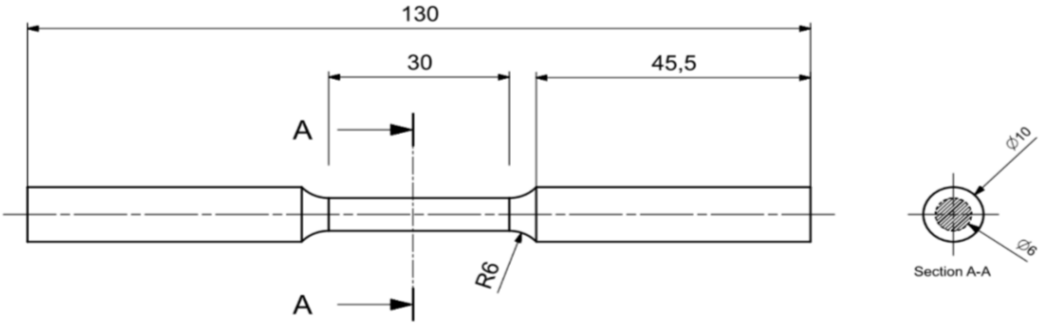

Figure 5.4 Sample Drawings

The produced samples, as shown in the Figure 5.1, exhibit a standardized geometry that ensures compatibility with tensile tests conducted according to ASTM standards. The geometries were designed to meet the requirements for tensile evaluation, ensuring reliable and consistent results. Tensile properties such as tensile strength, yield strength, and elongation were assessed in compliance with ASTM E8/E8M standards. The detailed drawings and specimen design, combined with optimized SLM parameters, contribute to a better understanding of the mechanical performance and hydrogen embrittlement resistance of AlSi10Mg alloy in industrial applications.

To enhance the hydrogen embrittlement resistance of SLM-produced AlSi10Mg samples, a combination of post-processing treatments and hydrogen exposure simulations was employed, as summarized in Table 5.2. The table outlines the treatment combinations applied to the samples, including stress relief, shot peening, and hydrogen charging, to evaluate their individual and combined effects on material properties. This systematic approach allowed for a detailed analysis of how these processes interact to improve the resistance of AlSi10Mg alloy to hydrogen-induced degradation and mechanical stresses.

Table 5.10 Summary of Post-Processing and Testing Combinations for SLM-Produced AlSi10Mg Samples

CODE	STRESS RELIEF	HYDROGEN CHARGING	SHOT PEENING
AL-SR-HC-SP	*	*	*
AL-HC-SP		*	*
AL-SR-SP-HC	*	*	*
AL-SP-HC		*	*
AL-SR-SP	*		*
AL-SP			*
AL-SR-HE	*	*	
AL-HE		*	
AL-SR	*		
AL			

To improve the performance of the samples, shot peening and stress relief treatments were applied as key post-processing techniques. Shot peening involved bombarding the surface of the samples with high-velocity steel balls, creating a compressive residual stress layer that counteracts tensile stresses contributing to crack initiation. ASR170 shot peening media is used in Wheelabrator MP 1000. The process was performed following the SAE AMS2430 standard with an intensity of 0.25 mmA, ensuring a consistent and controlled treatment across all samples.

In addition, stress relief treatments were conducted to mitigate internal residual stresses induced by the SLM process. This was achieved by partially annealing the samples in line with the AMS2770 standard, maintaining a temperature range of 333–349°C for 0.5 hours, followed by air cooling to stabilize the microstructure. This thermal treatment reduced stress concentration sites that could act as diffusion pathways for hydrogen.

To simulate hydrogen exposure, all samples underwent an electrochemical hydrogen charging process. The samples were immersed in a solution containing 3 wt.% NaCl and 3 g/L NH_4SCN A constant current density of 10 mA/cm^2 was applied for 24 hours to promote hydrogen diffusion into the microstructure. This charging method created a controlled hydrogen environment within the samples, enabling a realistic assessment of hydrogen embrittlement susceptibility.

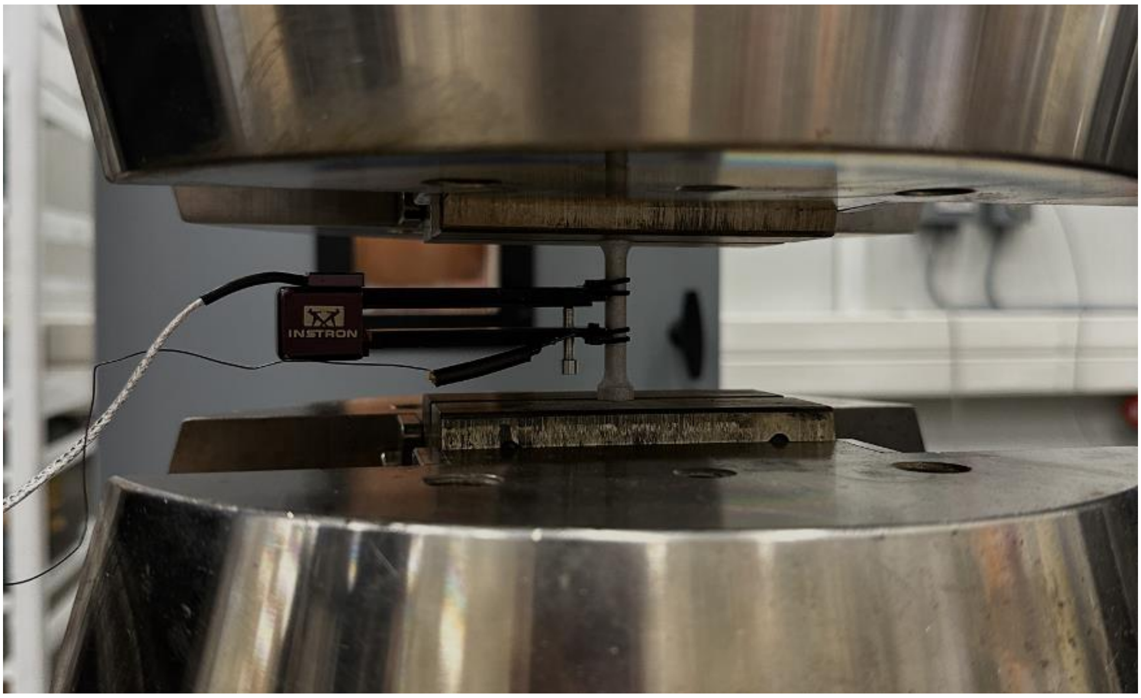

Figure 5.2 Tensile test of samples with extensometer

Tensile tests were conducted at room temperature using an INSTRON 5985 electromechanical universal testing machine up to 300 kN load cell capacity equipped with Instron Dynamic extensometer, 25 mm gage length, as shown in Figure 5.2, to ensure precise strain measurements. All tests have been carried out with a preload value of 1 kN to ensure stability of the specimen, 70 bar grip pressure applied, and load and strain values have been balanced prior to test initiation. The tests evaluated key mechanical properties, including ultimate tensile strength, yield strength, and elongation at fracture. Comparative analysis was performed on untreated, shot-peened (SP), and stress-relieved (SR) specimens under quasi-static (10^{-1} s^{-1}) and dynamic ($15 \cdot 10^{-3}$ s^{-1}) strain rate conditions. The results provided a comprehensive understanding of how post-processing techniques influence the strain rate sensitivity and fracture behavior of AlSi10Mg.

These combined methods offered a robust framework to analyze the impact of post-processing treatments on the hydrogen embrittlement resistance of AlSi10Mg alloys, enabling a comprehensive understanding of their mechanical behavior and microstructural characteristics in hydrogen-sensitive applications.

5.3 Results

The study investigates the mechanical and hydrogen embrittlement (HE) behaviors of SLM-manufactured AlSi10Mg alloy under various post-processing treatments and strain rates. The focus was on the influence of stress relief (SR), shot peening (SP), and their combination (SR + SP) on tensile strength, elongation, toughness, and resistance to hydrogen embrittlement. True stress-strain behavior and HE indices were examined to evaluate the role of post-processing in mitigating hydrogen-induced degradation. The comprehensive results provide insights into the mechanical performance of hydrogen-charged and non-hydrogen-charged specimens, highlighting the effectiveness of these treatments.

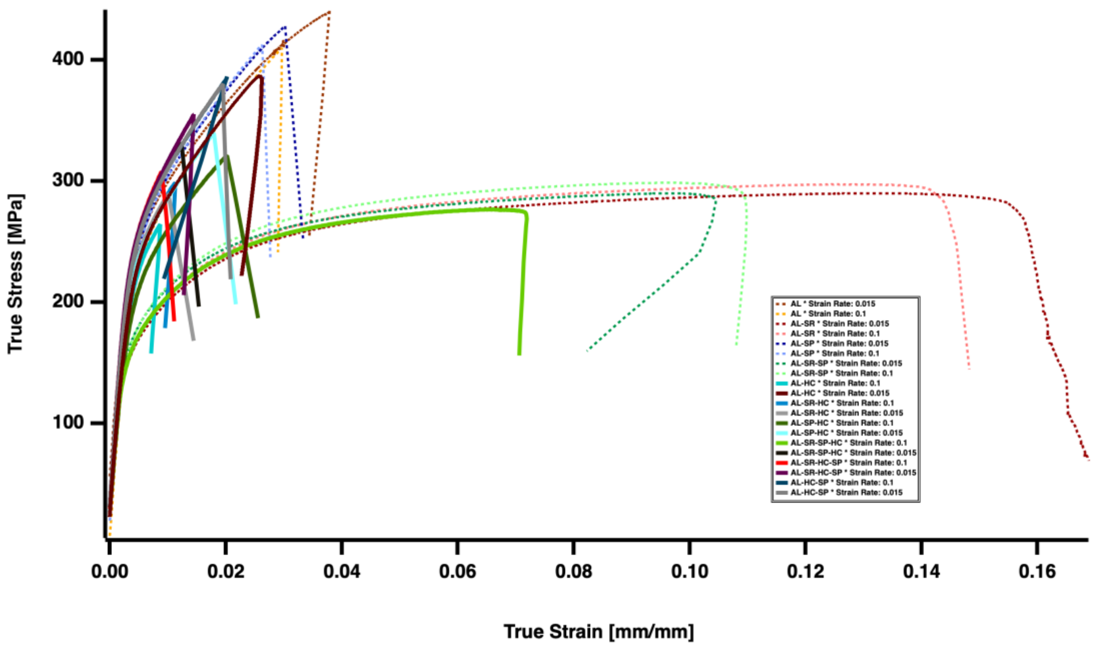

Figure 5.3 True Stress strain values of all samples with 0.1 and 0.015 s^{-1} strain rates.

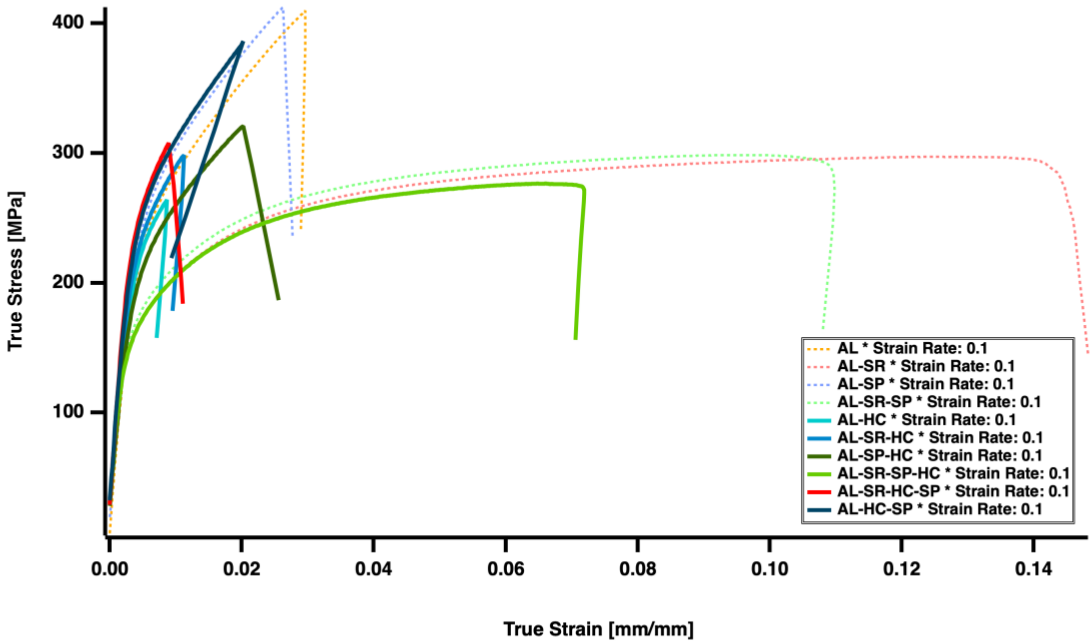

Figure 5.4 True Stress strain values of all samples with 0.1 s^{-1} strain rate.

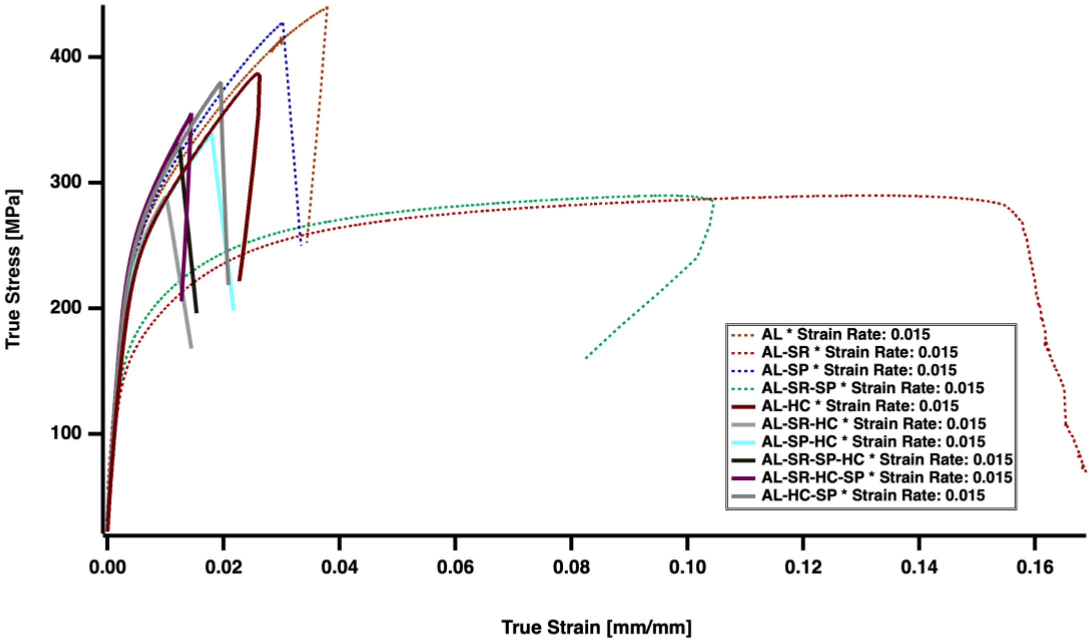

Figure 5.5 True Stress strain values of all samples with 0.015 s^{-1} strain rate.

Figures 5.3, 5.4, and 5.5 show the true stress-strain curves for all tested specimens at strain rates of 0.1 s^{-1} and 0.015 s^{-1}. Figure 5.3 combines all specimens to compare their overall mechanical behavior, while Figures 5.4 and 5.5 isolate the results for strain rates 0.1 s^{-1} and 0.015 s^{-1}, respectively. The results demonstrate significant differences in stress-strain responses between hydrogen-charged (HC) and non-hydrogen-charged (No HC) specimens. At 0.1 s^{-1} strain rate, non-hydrogen-charged specimens consistently exhibit higher ductility and ultimate tensile strength (UTS) compared to their hydrogen-charged counterparts. The AL-SP and AL-SR-SP specimens show resilience, maintaining relatively high strength and elongation, with SP treatments significantly delaying crack initiation. At 0.015 s^{-1}, the impact of hydrogen is more pronounced due to the increased hydrogen diffusion time. The AL-HC specimens exhibit brittle failure, characterized by a sudden drop in stress after reaching the yield point. However, combined SR + SP treatments further improve resistance by stabilizing the microstructure and reducing hydrogen diffusion pathways.

Table 5.11 Specimens' tensile test results

Specimen	Strain Rate	Tensile stress at Yield (Offset 0.2 %)	Ultimate Tensile	Young's Modulus [GPa]	Non-proportional elongatio	Toughness (MJ/m^3)

	[s^{-1}]	[MPa]	Strength (Rm) [MPa]		n (at break) [%]	
AL	10^{-1}	233.04	401	62.39	2.27	8.67
AL	$15 \cdot 10^{-3}$	246.48	418	58.78	2.94	11.64
AL-SR	10^{-1}	163.94	268	65.68	15.30	40.30
AL-SR	$15 \cdot 10^{-3}$	161.26	260	66.73	13.25	44.06
AL-SP	10^{-1}	249.59	402	66.66	1.86	8.51
AL-SP	$15 \cdot 10^{-3}$	251.06	415	66.04	2.26	10.78
AL-SR-SP	10^{-1}	170.93	274	65.20	11.11	29.40
AL-SR-SP	$15 \cdot 10^{-3}$	171.12	266	66.27	10.46	22.87
AL-HC	10^{-1}	225.92	262	64.19	0.32	1.33
AL-HC	$15 \cdot 10^{-3}$	233.38	377	67.16	1.87	6.61
AL-SR-HC	10^{-1}	238.92	295	63.91	0.57	2.08
AL-SR-HC	$15 \cdot 10^{-3}$	238.50	286	68.84	0.51	3.18
AL-SP-HC	10^{-1}	212.99	315	57.04	1.53	6.25
AL-SP-HC	$15 \cdot 10^{-3}$	231.82	333	73.88	1.29	5.64
AL-SR-SP-HC	10^{-1}	162.15	260	66.24	6.94	17.37
AL-SR-SP-HC	$15 \cdot 10^{-3}$	252.89	327	72.78	0.82	3.83

AL-SR-HC-SP	10^{-1}	261.22	305	72.66	0.39	2.54
AL-SR-HC-SP	$15 \cdot 10^{-3}$	259.45	350	72.60	0.89	3.36
AL-HC-SP	10^{-1}	255.32	379	69.38	1.37	2.54
AL-HC-SP	$15 \cdot 10^{-3}$	252.80	373	72.64	1.30	5.96

Table 5.3 summarizes the mechanical properties, including yield strength, ultimate tensile strength, Young's modulus, elongation, and toughness, for all specimens. Non-hydrogen-charged specimens (e.g., AL, AL-SR, AL-SP) show superior toughness and elongation compared to hydrogen-charged specimens, confirming the detrimental effects of hydrogen on ductility and toughness. The AL-SR and AL-SR-SP specimens benefit from stress relief treatments, which reduce residual stresses and stabilize the microstructure, significantly improving toughness (e.g., AL-SR toughness: 44.06 MJ/m^3). Shot peening treatments (e.g., AL-SP) introduce beneficial compressive residual stresses, enhancing yield and ultimate tensile strength while partially mitigating hydrogen effects.

5.3.1 Secondary Process effects on hydrogen embrittlement

Figure 5.6 and Table 5.4 collectively present the effects of hydrogen embrittlement (HE) on the mechanical properties of as-built (AL), stress-relieved (SR), shot-peened (SP), and combined SR + SP specimens under two different strain rates (0.1 s^{-1} and 0.015 s^{-1}). The results show that stress relief enhances the mechanical strength of non-hydrogen charged specimens compared to as-built conditions by reducing internal residual stresses, with SR-treated specimens achieving a higher ultimate tensile strength (UTS). For instance, at 0.1 s^{-1}, SR specimens reach approximately 400 MPa compared to 370 MPa for as-built specimens. However, ductility remains similar between these two conditions, indicating that SR primarily influences strength rather than elongation in non-hydrogen charged environments.

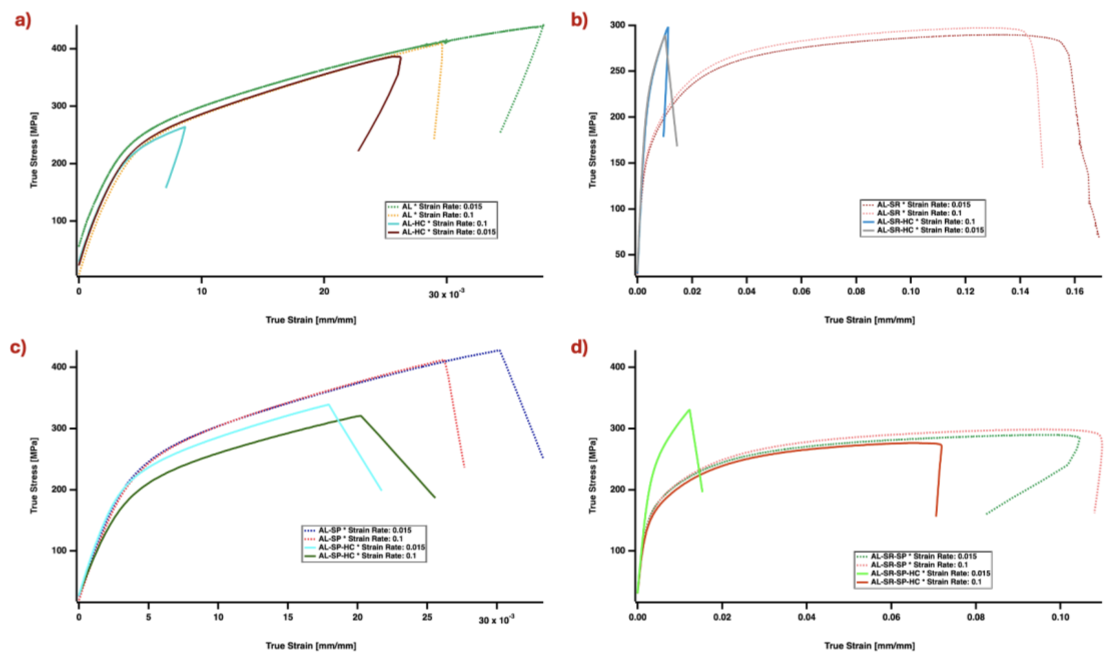

Figure 5.6 Secondary Process (as-built, SP, SR, SP and SR+SP) effects on hydrogen embrittlement at different strain rates

Subfigure 5.6a illustrates the effect of hydrogen embrittlement on as-built (AL) specimens at strain rates of 0.1 s^{-1} and 0.015 s^{-1}. In the non-hydrogen charged condition, the as-built specimen exhibits a UTS of approximately 401 MPa at 0.1 s^{-1}, but under hydrogen charging, this value drops significantly to 262 MPa, corresponding to an HE index of 84.66%. At the lower strain rate of 0.015 s^{-1}, the UTS for hydrogen-charged as-built specimens improves to 377 MPa, reducing the HE index to 43.18%. This behavior indicates that strain rate significantly affects hydrogen diffusion and accumulation, with higher strain rates limiting hydrogen effects more effectively.

Subfigure 5.6b focuses on stress-relieved (SR) specimens under similar conditions. Stress relief reduces internal residual stresses, resulting in improved toughness for non-hydrogen charged specimens, reaching 40.30 MJ/m^3 at 0.1 s^{-1}. However, under hydrogen charging, SR specimens exhibit severe embrittlement. The UTS drops from 268 MPa in the non-hydrogen condition to 260 MPa at 0.1 s^{-1} and remains almost unchanged at 286 MPa at 0.015 s^{-1}. The consistently high HE indices of 94.84% and 92.77% at these strain rates highlight that stress relief alone does not effectively mitigate hydrogen-induced degradation. Additionally, the non-proportional elongation of SR specimens under hydrogen-charged conditions reduces drastically compared to non-hydrogen charged specimens, with values dropping to as low as 0.51% at 0.015 s^{-1}, reflecting severe brittleness. Young's modulus values remain relatively stable across conditions, with minor increases to 66.73 GPa at the lower strain rate, but this does not compensate for the loss in ductility.

Subfigure 5.6c highlights the performance of shot-peened (SP) and combined SR + SP specimens in non-hydrogen charged conditions. SP-treated specimens demonstrate enhanced mechanical properties, achieving a UTS of approximately 402 MPa at 0.1 s^{-1}, with toughness values of 8.51 MJ/m^3. Combined SR + SP treatments further increase UTS to around 430 MPa at 0.1 s^{-1}, with toughness reaching 29.40 MJ/m^3, indicating the beneficial synergy of these treatments in enhancing strength and delaying crack initiation. Both treatments significantly outperform as-built and SR-only specimens in non-hydrogen charged environments.

Subfigure 5.6d examines SP-treated and SR + SP specimens under hydrogen charging. SP-treated specimens retain the best resistance to hydrogen embrittlement, with a UTS of approximately 315 MPa at 0.1 s^{-1} and an HE index of 26.58%. Combined SR + SP specimens, while less effective, achieve intermediate performance with a UTS of around 260 MPa and an HE index of 40.92%. At 0.015 s^{-1}, the HE indices for SP-treated and SR + SP specimens increase to 47.72% and 83.24%, respectively, reflecting the impact of prolonged hydrogen exposure on these treatments.

Table 5.12 HE Index of Specimens

Strain Rate [s^{-1}]	Non-Hydrogen Charged Specimens	Hydrogen Charged Specimens	HE Index (%)
10^{-1}	AL	AL-HC	84.66
$15 \cdot 10^{-3}$	AL	AL-HC	43.18
10^{-1}	AL-SR	AL-SR-HC	94.84
$15 \cdot 10^{-3}$	AL-SR	AL-SR-HC	92.77
10^{-1}	AL-SP	AL-SP-HC	26.58
$15 \cdot 10^{-3}$	AL-SP	AL-SP-HC	47.72

10^{-1}	AL-SR-SP	AL-SR-SP-HC	40.92
$15 \cdot 10^{-3}$	AL-SR-SP	AL-SR-SP-HC	83.24

The increase in HE index, shown in Table 5.4, for SP-treated and SR + SP specimens at lower strain rates is attributed to the saturation of hydrogen traps created by compressive residual stresses. At higher strain rates, these traps effectively limit hydrogen diffusion, reducing embrittlement. However, at slower strain rates, prolonged exposure allows hydrogen to accumulate, diminishing the effectiveness of these mechanisms. In contrast, the relatively unchanged HE indices for SR-treated specimens indicate that internal stress reduction alone does not sufficiently mitigate hydrogen diffusion.

Overall, the data presented in Figure 5.5, and Table 14 emphasize the critical role of post-processing treatments in enhancing the hydrogen embrittlement resistance of additively manufactured AlSi10Mg alloys. Shot peening emerges as the most effective treatment, significantly reducing the HE index and improving mechanical properties under hydrogen-charged conditions. Combined SR + SP treatments provide a balanced solution but remain less effective than SP alone, particularly at lower strain rates. These findings underscore the importance of tailored strategies that address both surface and internal microstructural factors to optimize material performance in hydrogen-sensitive environments.

5.3.2 Shot Peening effects on hydrogen embrittlement

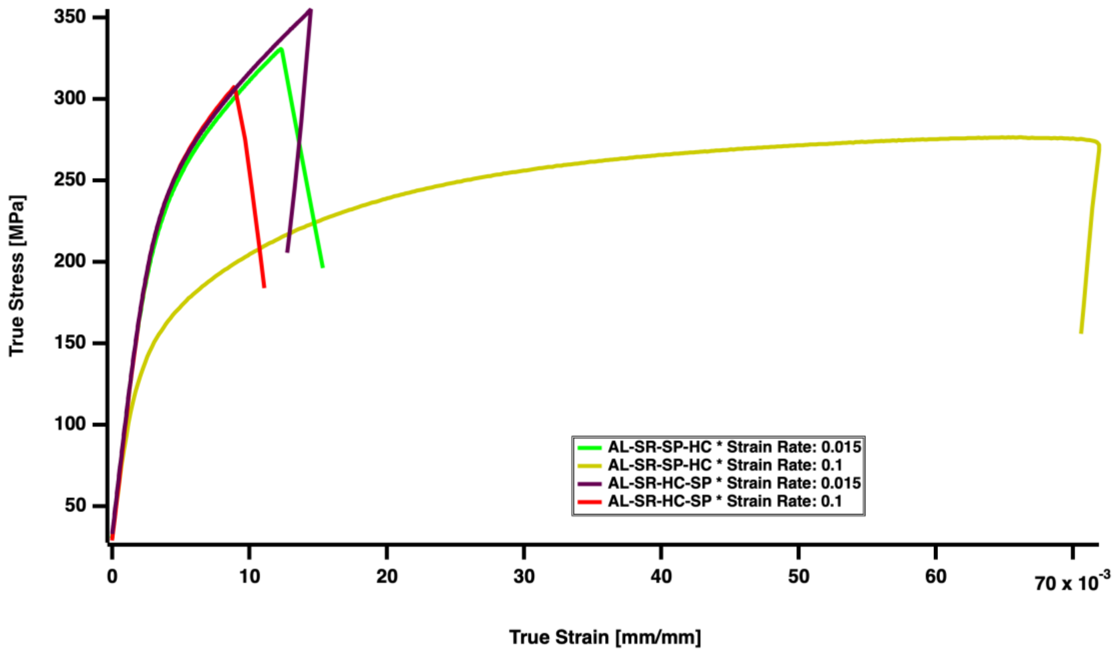

Figure 5.7 Effect of HC before and after SP

Figure 5.7 provides a detailed comparison of the effects of hydrogen charging before and after shot peening (SP) treatment. The key comparison is between AL-SR-HC-SP (hydrogen charging before SP) and AL-SR-SP-HC (hydrogen charging after SP).

In AL-SR-HC-SP specimens, the introduction of SP after hydrogen charging does improve resistance to embrittlement, with a UTS of 305 MPa at 0.1 s^{-1} and 350 MPa at 0.015 s^{-1}, but the effectiveness is limited due to pre-existing hydrogen within the microstructure. This hydrogen has already diffused into critical regions, weakening the material despite the introduction of compressive residual stresses.

Conversely, AL-SR-SP-HC specimens, where SP is performed prior to hydrogen charging, exhibit a UTS of 260 MPa at 0.1 s^{-1} and 327 MPa at 0.015 s^{-1}, reflecting better resistance to hydrogen embrittlement. The compressive residual stresses from SP create barriers that impede hydrogen diffusion, demonstrating the importance of the sequence of treatments.

When compared with other hydrogen-charged samples, AL-SR-HC-SP performs better than AL-SR-HC and AL-HC specimens, which exhibit UTS values of 295 MPa and 262 MPa, respectively, at 0.1 s^{-1}. At 0.015 s^{-1}, AL-SR-HC-SP also outperforms AL-SR-HC and AL-HC, which achieve UTS values of 286 MPa and 233 MPa, respectively. This improvement underscores the beneficial role of SP even when applied after hydrogen charging. However, the performance of AL-SR-HC-SP is still inferior to AL-SP-HC (315

MPa at 0.1 s^{-1} and 333 MPa at 0.015 s^{-1}) and AL-SR-SP-HC (350 MPa at 0.1 s^{-1} and 327 MPa at 0.015 s^{-1}), confirming that the timing of SP treatment is crucial for maximizing resistance to hydrogen embrittlement. The results emphasize that while SP can mitigate some effects of pre-existing hydrogen, its full potential is realized when applied before hydrogen exposure.

The results underscore that shot peening's effectiveness in mitigating hydrogen embrittlement is significantly influenced by whether hydrogen charging occurs before or after the treatment. Hydrogen introduced into the material prior to SP creates irreversible microstructural changes that cannot be fully mitigated by subsequent compressive residual stresses. This highlights the critical need to optimize the sequence of post-processing treatments for additively manufactured alloys to achieve maximum hydrogen embrittlement resistance. Future research should explore advanced methods to remove pre-existing hydrogen or prevent its diffusion before applying surface treatments like shot peening.

5.3.3 Strain Rate effects on hydrogen embrittlement

The strain rate sensitivity (m) of the tested materials was evaluated to determine the effects of strain rate and hydrogen charging on their mechanical behavior. As shown in Figure 5.8, true stress values generally decreased as the strain rate increased across all specimens. For uncharged materials, strain rate sensitivity remained relatively low. For example, AL and AL-SP exhibited m values of 0.0219 and 0.0168, respectively. This indicates that these materials maintain stable mechanical properties over varying deformation rates, making them suitable for applications where strain rate changes are common.

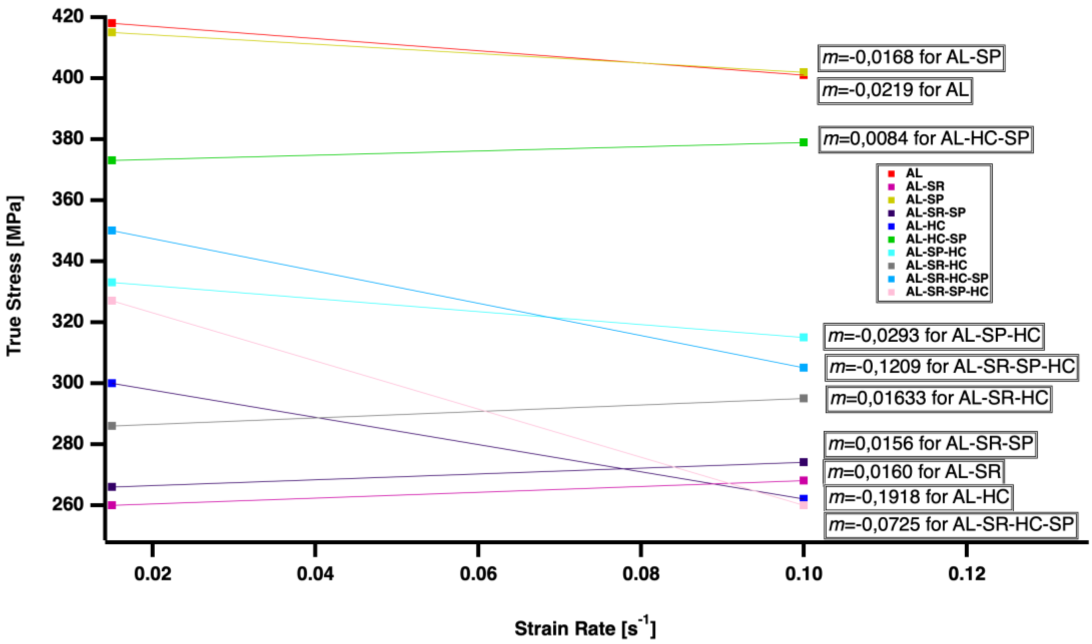

Figure 5.8 Strain rate effect on true stress values on samples and strain rate sensitivity (*m*) values

In contrast, the hydrogen-charged specimens displayed significantly higher strain rate sensitivities. AL-SP-HC and AL-SR-HC showed *m* values of 0.0263 and 0.1290, respectively, indicating a notable increase compared to their uncharged counterparts. Similarly, AL-SR-SP, a hydrogen-charged specimen, exhibited the highest *m* value of 0.1918. This substantial difference highlights the critical role of hydrogen in altering the mechanical response of materials under varying strain rates. The higher *m* values in hydrogen-charged specimens suggest that the presence of hydrogen enhances strain rate sensitivity, likely due to its interactions with dislocations and microstructural features.

The data also reveal that hydrogen affects the mechanical stability of materials, particularly at higher strain rates. Uncharged specimens exhibit relatively stable behavior across different strain rates, with only slight decreases in true stress. In contrast, hydrogen-charged specimens exhibit greater reductions in true stress as the strain rate increases. This behavior suggests that hydrogen-charged materials are more sensitive to dynamic deformation, which could result in earlier failure under high-strain-rate conditions. Hydrogen's interaction with internal microstructural features can promote a shift in fracture mode from ductile to brittle, intensifying the material's susceptibility to embrittlement.

These observations underscore hydrogen's bifunctional influence: it enhances sensitivity to strain rates, which may be advantageous under dynamic loading, but concurrently poses a threat by promoting embrittlement mechanisms. This is particularly relevant for applications involving dynamic or high-strain-rate environments, where the material's performance could be compromised. The differences in mmm values between hydrogen-charged and uncharged specimens underscore the importance of considering hydrogen's effects during the material selection and design process.

In summary, hydrogen charging significantly influences the strain rate sensitivity of materials, as evidenced by the elevated *m* values and increased reductions in true stress under dynamic conditions. While uncharged specimens maintain relatively consistent mechanical properties across varying strain rates, hydrogen-charged materials demonstrate heightened sensitivity, which may limit their reliability in certain applications. These results highlight the need for further investigations into the mechanisms driving hydrogen-induced changes in material behavior.

5.4 Discussions

This study investigates the effects of post-processing treatments—shot peening (SP), stress relief (SR), and their combination (SP+SR)—on the hydrogen embrittlement (HE) resistance of AlSi10Mg specimens produced via Selective Laser Melting (SLM). The findings reveal significant interactions between hydrogen charging, strain rates, and post-processing techniques, providing valuable insights for mitigating HE in additively manufactured components.

Hydrogen embrittlement (HE) is strongly influenced by the interaction of hydrogen atoms with microstructural defects such as dislocations, voids, and grain boundaries [170,248]. The unique microstructure of AlSi10Mg, characterized by fine Si particles distributed within the Al matrix, plays a pivotal role in determining its mechanical properties and susceptibility to hydrogen charging [249–251]. While silicon contributes to strength and thermal stability, Si-rich phases may act as hydrogen traps or stress concentrators, exacerbating localized plasticity and influencing hydrogen diffusion and accumulation [252–255]. These observations, particularly the role of Si-rich phases in stress concentration and hydrogen trapping, align with Hydrogen-Enhanced Localized Plasticity (HELP) and Hydrogen-Enhanced Decohesion (HEDE), mechanisms that were evident in this study.

Strain rate sensitivity ("*m*" values) was a key focus, as it provides an indication of the material's susceptibility to dynamic deformation in hydrogen-rich environments [223]. Hydrogen-charged specimens exhibited markedly higher "*m*" values compared to uncharged ones, consistent with the HELP mechanism. For instance, AL-SP-HC and AL-SR-HC had "*m*" values of 0.0263 and 0.1290, respectively, while AL-SR-SP showed the highest sensitivity at 0.1918. These findings align with Wagner and Mueller [92], who observed similar enhancements in strain rate sensitivity in aluminum alloys subjected to shot peening.

Shot peening (SP) significantly improved resistance to HE by introducing compressive residual stresses and reducing pore size, enhancing fatigue resistance and delaying crack initiation in hydrogen-charged environments [91,93,230]. SP-treated samples, such as AL-SP-HC, exhibited improved mechanical stability, emphasizing the importance of surface treatments in mitigating hydrogen diffusion. Uzan et al. [93] reported that SP-induced compressive stresses significantly enhance fatigue life, findings corroborated by Maamoun et al. [91] who highlighted stress redistribution and microstructure refinement through SP.

Stress relief treatments effectively reduced internal residual stresses and stabilized the microstructure. AL-SR specimens showed significant improvements in toughness and elongation compared to as-built samples, as noted in Fernandes et al. (2025) [251], who highlighted stress relief's role in homogenizing the microstructure and reducing fatigue scatter under low-cycle conditions. Similarly, stress-relieved specimens exhibited more evenly distributed Si particles and fewer stress concentration sites, contributing to enhanced elongation and resistance to crack initiation. However, stress relief alone was insufficient to fully mitigate the effects of hydrogen. Hydrogen-charged AL-SR specimens displayed significant reductions in ultimate tensile strength (UTS) and elongation, emphasizing the necessity of combining stress relief with other treatments. Similar findings were reported by Chen et al. (2020) [254], who observed that while stress relief improved residual stress conditions, its sole application could not counteract the effects of hydrogen embrittlement.

The combination of SP and SR provided optimal performance, particularly at lower strain rates where hydrogen diffusion is more pronounced. AL-SR-SP specimens exhibited notable improvements in UTS, toughness, and ductility compared to individually treated specimens. Wagner and Mueller [92] demonstrated the synergistic benefits of combining surface and thermal treatments in enhancing fatigue life. However, the efficacy of SP+SR diminished under prolonged hydrogen exposure, suggesting the need for additional protective measures such as coatings or hydrogen barriers.

Microstructural analysis further highlighted the role of Si-rich phases and melting pool characteristics in influencing HE behavior. The unique microstructure of the melting pool, characterized by fine cellular dendrites and Si-rich boundaries formed due to rapid solidification in SLM, significantly impacts hydrogen trapping and diffusion. Variations in grain size and porosity within the melting pool can exacerbate localized plasticity and act as hydrogen traps, as observed in previous studies. SP-treated specimens showed improved resistance to crack initiation near Si-rich zones, providing strong evidence that hydrogen-induced localized plasticity and decohesion are key contributors to embrittlement in SLM materials.

While rapid deformation rates typically limit hydrogen diffusion, this study observed significant embrittlement even at higher strain rates in hydrogen-charged specimens, likely due to residual stress concentrations introduced during the SLM process and the anisotropic nature of the molten pool structure [256]. These findings underscore the interplay between manufacturing-induced defects, Si content, molten pool morphology, and hydrogen embrittlement, necessitating further investigation into optimized process parameters and post-treatment strategies. Studies have shown that SP-induced hardening enhances fatigue performance in aluminum alloys by refining grain boundaries and increasing dislocation density [257]. Similarly, this study noted that SP-treated specimens exhibited improved resistance to crack initiation near Si-rich zones, emphasizing the critical role of the melting pool microstructure in determining HE resistance.

Interestingly, deviations were noted in ductility reductions at higher strain rates. While prior work suggested that rapid deformation rates limit hydrogen diffusion, this study observed significant embrittlement even at higher strain rates in hydrogen-charged specimens [254]. This discrepancy is likely due to residual stress concentrations introduced during the SLM process, which exacerbate the effects of hydrogen under dynamic loading. This highlights the interplay between manufacturing-induced defects, Si content, and hydrogen embrittlement, necessitating further investigation into optimized process parameters and post-treatment strategies.

In summary, this study demonstrates that post-processing treatments significantly influence the mechanical behavior and HE resistance of SLM-produced AlSi10Mg specimens. Shot peening emerged as the most effective single treatment, enhancing surface properties and delaying crack propagation. The combination of SP and SR provided superior performance under varied strain rates, reinforcing the importance of integrated treatment strategies. Furthermore, the role of Si-rich phases in influencing hydrogen diffusion and microstructural stability was highlighted, emphasizing the need for tailored post-processing approaches. These findings contribute to the growing body of knowledge on mitigating HE in additively manufactured components and underscore the necessity of combining surface, thermal, and protective measures to ensure long-term durability in hydrogen-sensitive applications.

5.5 Conclusions

This study comprehensively examined the effects of shot peening and stress relief treatments on the hydrogen embrittlement (HE) resistance of AlSi10Mg alloy produced through Selective Laser Melting (SLM). The results demonstrate that:

This study systematically explored the effects of shot peening (SP), stress relief (SR), and their combination (SP+SR) on the hydrogen embrittlement (HE) resistance of AlSi10Mg alloy manufactured via Selective Laser Melting (SLM). The findings emphasize the importance of post-processing strategies in mitigating HE and enhancing the mechanical performance of SLM-produced alloys under hydrogen-rich environments.

Shot peening emerged as the most effective single treatment, significantly improving HE resistance by introducing compressive residual stresses and reducing surface porosity. This was particularly evident at higher strain rates, where the HE index was reduced to 26.58%, demonstrating SP's ability to delay crack initiation and propagation.

Stress relief treatments effectively stabilized the microstructure by reducing internal residual stresses, resulting in improved toughness and elongation. However, SR alone was insufficient to fully mitigate hydrogen-induced degradation, particularly at lower strain rates where hydrogen diffusion is more pronounced.

The integration of SP and SR provided a balanced improvement in HE resistance, with an intermediate HE index of 40.92%. This dual treatment reduced hydrogen diffusion pathways and stabilized the microstructure but showed diminished efficacy under prolonged hydrogen exposure, suggesting the necessity of additional protective measures.

The susceptibility to HE was strongly strain rate-dependent. Higher strain rates limited hydrogen diffusion but retained the influence of residual stresses, while lower strain rates exacerbated embrittlement effects due to prolonged hydrogen exposure.

Overall, This study highlights the critical interplay between post-processing treatments, microstructural characteristics, and strain rates in mitigating HE in SLM-produced AlSi10Mg alloys. The results contribute to the growing body of knowledge on hydrogen-resistant materials and offer a foundation for optimizing post-processing strategies for high-performance applications in hydrogen-sensitive industries such as aerospace, automotive, and energy. Future research should focus on integrating advanced coatings and protective barriers to further enhance resistance to hydrogen-induced degradation.

Chapter 6

Conclusions and Future Prospects

6.1 Conclusions

This study presents a comprehensive exploration into the optimization of shot peening processes and the mitigation of hydrogen embrittlement in Selective Laser Melting (SLM)-manufactured AlSi10Mg alloys. The findings significantly contribute to addressing critical challenges in advanced manufacturing technologies, particularly in industries demanding high-performance and reliable materials.

The first major conclusion of this study is the effectiveness of integrating Artificial Intelligence (AI)-based optimization into shot peening processes. By employing a hybrid approach combining advanced algorithms such as Differential Evolution, Simulated Annealing, Nelder-Mead, and Random Search, the research successfully optimized key parameters of shot peening. This innovative methodology not only enhanced process efficiency but also demonstrated a significant reduction in mechanical defects, such as surface roughness and porosity, which are prevalent in additively manufactured components.

A key outcome of the research was the establishment of reliable correlations between shot peening intensity and improvements in mechanical performance, particularly in fatigue resistance. By precisely controlling parameters such as air pressure, shot velocity, and coverage, the optimized process induced compressive residual stresses that effectively enhanced the fatigue life of AlSi10Mg components. This highlights the critical role of post-processing techniques in overcoming inherent limitations of the SLM process, such as microstructural anisotropy and residual tensile stresses.

The study also provided valuable insights into the mechanisms of hydrogen embrittlement (HE) in lightweight alloys, elucidating the role of hydrogen-enhanced decohesion (HEDE) and hydrogen-enhanced localized plasticity (HELP). The findings emphasized the detrimental effects of hydrogen diffusion in SLM-produced alloys, which significantly compromise their ductility and fracture toughness. By employing post-processing techniques, particularly shot peening and heat treatment, the research demonstrated effective mitigation strategies that reduce hydrogen susceptibility and enhance material resilience in hydrogen-rich environments.

Additionally, real-world case studies involving aviation components underscored the critical implications of hydrogen embrittlement in safety-critical applications. The analysis of failures in aircraft systems provided a strong justification for the adoption of optimized post-processing methods, both as preventive measures and as corrective strategies to improve material reliability.

From a broader perspective, the study emphasizes the transformative potential of combining additive manufacturing with advanced post-processing techniques and AI-driven optimization. The findings support the broader adoption of SLM in high-performance applications, particularly in aerospace and defense sectors, where material reliability and performance are non-negotiable. Furthermore, the integration of AI into manufacturing workflows highlights the importance of computational tools in achieving precision and efficiency in modern production systems.

In conclusion, this research bridges critical gaps in understanding and optimizing the interplay between additive manufacturing, post-processing, and material behavior. By addressing challenges such as residual stresses, surface imperfections, and hydrogen embrittlement, the study offers a robust framework for improving the mechanical performance and reliability of additively manufactured components. The methodologies and insights developed in this thesis pave the way for future advancements in manufacturing technologies, contributing to safer, more efficient, and sustainable industrial practices.

6.2 Societal Impact and Contribution to Global Sustainability

The findings of this research contribute profoundly to addressing contemporary societal challenges and advancing global sustainability goals. Additive Manufacturing (AM), particularly Selective Laser Melting (SLM), represents a significant leap forward in reducing waste and energy consumption while enhancing production efficiency. By enabling the creation of highly complex and durable components with minimal material usage, AM directly supports the principles of a circular economy. This reduction in material waste not only minimizes the environmental impact of manufacturing but also ensures the efficient use of resources, which is crucial in today's resource-constrained world.

One of the key societal impacts of this research is its focus on extending the lifespan of critical components in sectors such as aerospace, automotive, and defense. The optimization of shot peening processes, as demonstrated in this study, significantly enhances the fatigue resistance and mechanical performance of materials like AlSi10Mg alloys. Longer-lasting materials reduce the need for frequent replacements, leading to decreased resource consumption and less environmental pollution. This is particularly critical in industries where material reliability is paramount, such as aviation, where failures can result in both human casualties and severe environmental damage.

Furthermore, this research highlights methods to mitigate hydrogen embrittlement, a phenomenon that threatens the structural integrity of lightweight materials in hydrogen-rich environments. With the global shift toward clean energy technologies like hydrogen fuel cells, the strategies developed in this study ensure the safety and reliability of materials used in sustainable energy systems. By addressing this challenge, the research supports the broader adoption of hydrogen as a clean energy source, contributing to the reduction of carbon emissions and combating climate change.

The integration of artificial intelligence (AI) in process optimization also offers significant sustainability benefits. AI-driven optimization reduces the number of experimental trials needed, thereby minimizing the consumption of energy and raw materials during the development phase. Additionally, AI facilitates precise control over manufacturing processes, ensuring that resources are used efficiently, and waste is kept to a minimum. These advancements align with international sustainability frameworks such as the United Nations' Sustainable Development Goals (SDGs), particularly Goal 12, which focuses on responsible consumption and production.

On a societal level, this research also addresses safety concerns associated with material failures. The application of optimized shot peening and post-processing techniques in industries like aviation prevents catastrophic accidents, which not only saves lives but also avoids the environmental and economic consequences of such failures. By enhancing material reliability, this study contributes to building safer and more resilient infrastructures, which are vital for sustainable development.

In conclusion, this research not only advances the technological capabilities of manufacturing but also aligns with broader sustainability objectives. By improving resource efficiency, supporting clean energy initiatives, and enhancing the safety and durability of critical materials, it addresses key challenges faced by society today. These contributions position the findings of this study as a cornerstone for future developments in sustainable manufacturing and material science.

6.3 Future Prospects

The findings and methodologies developed in this research open numerous pathways for future exploration and innovation in additive manufacturing and material science. One of the most promising directions is the integration of real-time monitoring systems with artificial intelligence (AI). By combining sensor-based data acquisition with AI algorithms, future studies could enable dynamic process adjustments, ensuring consistent quality and performance in complex manufacturing workflows.

Another area of potential research lies in expanding the application of optimized shot peening processes to other materials and industries. While this study focuses on AlSi10Mg alloys, the methodologies could be adapted to enhance the performance of other advanced alloys or composites used in sectors such as biomedical engineering, renewable energy, and construction. For example, similar approaches could improve the durability of materials in wind turbine blades or the corrosion resistance of medical implants.

Further investigations could also explore novel post-processing techniques that complement shot peening, such as laser surface treatment or advanced heat treatments, to address challenges like residual stresses and surface imperfections more effectively. Exploring combinations of post-processing methods might yield synergetic effects that enhance material properties beyond the current benchmarks.

From a broader perspective, the application of AI optimization could be extended to multi-objective scenarios where multiple parameters, such as cost, environmental impact, and performance, are simultaneously considered. This would allow industries to balance efficiency with sustainability goals more effectively.

Lastly, as global industries increasingly adopt hydrogen-based technologies, such as hydrogen fuel cells, the mitigation strategies for hydrogen embrittlement developed in this study could play a pivotal role in ensuring the reliability of materials used in these systems. Research into scalable and cost-effective solutions for hydrogen embrittlement will become increasingly critical as the world transitions toward cleaner energy alternatives.

By addressing these future opportunities, this research lays a strong foundation for continued advancements in additive manufacturing, post-processing techniques, and material durability, fostering a sustainable and technologically advanced future.

BIBLIOGRAPHY

[1] SrinivasN. and DebKalyanmoy, Muiltiobjective optimization using nondominated sorting in genetic algorithms, Evol Comput 2, 221 (1994).

[2] S. Wang, J. Wan, D. Li, and C. Zhang, Implementing Smart Factory of Industrie 4.0: An Outlook, Http://Dx.Doi.Org/10.1155/2016/3159805 2016, (2016).

[3] I. Boussaïd, J. Lepagnot, and P. Siarry, A survey on optimization metaheuristics, Inf Sci (N Y) 237, 82 (2013).

[4] M. C. D. & A.-C. C. C. Myers H Raymond, Response Surface Methodology: Process and Product Optimization Using ... -, Wiley Series in Probability and Statistics, 4th Ed., John Wiley & Sons Inc., New Jersey 894 (2016).

[5] A. R. Yildiz, Optimal structural design of vehicle components using topology design and optimization, Materialpruefung/Materials Testing 50, 224 (2008).

[6] H. S. Park, D. S. Nguyen, T. Le-Hong, and X. Van Tran, Machine learning-based optimization of process parameters in selective laser melting for biomedical applications, J Intell Manuf 33, 1843 (2022).

[7] İ. Polatoğlu and L. Aydin, A new design strategy with stochastic optimization on the preparation of magnetite cross-linked tyrosinase aggregates (MCLTA), Process Biochemistry 99, 131 (2020).

[8] Energy and Process Optimization for the Process Industries, Energy and Process Optimization for the Process Industries (2013).

[9] M. F. R. Lee, A Review on Intelligent Control Theory and Applications in Process Optimization and Smart Manufacturing, Processes 2023, Vol. 11, Page 3171 11, 3171 (2023).

[10] H. Gröning, J. Zenisek, N. Wild, A. Huskic, and M. Affenzeller, Method of Process Optimization for LMD-Processes using Machine Learning Algorithms, Procedia Comput Sci 217, 1506 (2023).

[11] J. Antoy, Design of Experiments for Engineers and Scientists: Second Edition, Design of Experiments for Engineers and Scientists: Second Edition 1 (2014).

[12] R. Fontana, A. Molena, L. Pegoraro, and L. Salmaso, Design of experiments and machine learning with application to industrial experiments, Statistical Papers 64, 1251 (2023).

[13] A. van Aartsengel and S. Kurtoglu, Experimental Study: Design of Experiments, Handbook on Continuous Improvement Transformation 247 (2013).

[14] P. M. Murray, F. Bellany, L. Benhamou, D. K. Bučar, A. B. Tabor, and T. D. Sheppard, The application of design of experiments (DoE) reaction optimisation and solvent selection in the development of new synthetic chemistry, Org Biomol Chem 14, 2373 (2016).

[15] R. Tanious, R. Manolov, P. Onghena, and J. W. S. Vlaeyen, Single-case experimental designs: the importance of randomization and replication, Nature Reviews. Methods Primers 4, 27 (2024).

[16] M. F. Kahraman, H. Bilge, and S. Öztürk, Uncertainty analysis of milling parameters using monte carlo simulation, the taguchi optimization method and data-driven modeling, Materialpruefung/Materials Testing 61, 477 (2019).

[17] G. Box, S. Bisgaard, and C. Fung, An explanation and critique of taguchi's contributions to quality engineering, Qual Reliab Eng Int 4, 123 (1988).

[18] A. M. Khorasani, I. Gibson, U. S. Awan, and A. Ghaderi, The effect of SLM process parameters on density, hardness, tensile strength and surface quality of Ti-6Al-4V, Addit Manuf 25, 176 (2019).

[19] J. Liu, J. Ye, D. Silva Izquierdo, A. Vinel, N. Shamsaei, and S. Shao, A review of machine learning techniques for process and performance optimization in laser beam powder bed fusion additive manufacturing, J Intell Manuf 34, 3249 (2023).

[20] H. M. Khan, T. B. Sirin, G. Tarakci, M. E. Bulduk, M. Coskun, E. Koc, and Y. Kaynak, Improving the surface quality and mechanical properties of selective laser sintered PA2200 components by the vibratory surface finishing process, SN Applied Sciences 2021 3:3 3, 1 (2021).

[21] D. S. Nguyen, H. S. Park, and C. M. Lee, Optimization of selective laser melting process parameters for Ti-6Al-4V alloy manufacturing using deep learning, J Manuf Process 55, 230 (2020).

[22] H. S. Park, D. S. Nguyen, T. Le-Hong, and X. Van Tran, Machine learning-based optimization of process parameters in selective laser melting for biomedical applications, J Intell Manuf 33, 1843 (2022).

[23] M. Marrey, E. Malekipour, H. El-Mounayri, and E. J. Faierson, A Framework for Optimizing Process Parameters in Powder Bed Fusion (PBF) Process Using Artificial Neural Network (ANN), Procedia Manuf 34, 505 (2019).

[24] D. S. Nguyen, H. S. Park, and C. M. Lee, Optimization of selective laser melting process parameters for Ti-6Al-4V alloy manufacturing using deep learning, J Manuf Process 55, 230 (2020).

[25] M. Marrey, E. Malekipour, H. El-Mounayri, and E. J. Faierson, A Framework for Optimizing Process Parameters in Powder Bed Fusion (PBF) Process Using Artificial Neural Network (ANN), Procedia Manuf 34, 505 (2019).

[26] S. L. C. Ferreira et al., Box-Behnken design: An alternative for the optimization of analytical methods, Anal Chim Acta 597, 179 (2007).

[27] X. Shen, G. Zhang, and B. Bjerg, Assessments of experimental designs in response surface modelling process: Estimating ventilation rate in naturally ventilated livestock buildings, Energy Build 62, 570 (2013).

[28] S. L. C. Ferreira et al., Box-Behnken design: An alternative for the optimization of analytical methods, Anal Chim Acta 597, 179 (2007).

[29] S. Beg and S. Akhter, Box–Behnken Designs and Their Applications in Pharmaceutical Product Development, Design of Experiments for Pharmaceutical Product Development Volume I: Basics and Fundamental Principles 1, 77 (2021).

[30] C.-S. Cheng, Theory of Factorial Design : Single- and Multi-Stratum Experiments, Theory of Factorial Design (2016).

[31] D. A. Colette, A. K. D. Martial, A. Y. Joseph, Y. K. Benjamin, and D. A. Patrick, Optimization of the compressive strength of used tire/cement phase composite concretes using a full factorial design, Constr Build Mater 404, 133252 (2023).

[32] S. Karimifard and M. R. Alavi Moghaddam, Application of response surface methodology in physicochemical removal of dyes from wastewater: A critical review, Science of The Total Environment 640–641, 772 (2018).

[33] S. Hmamouchi, Y. Abbad, A. El Yacoubi, A. Boulouiz, B. Sallek, and B. C. El Idrissi, Optimization study of methylene blue dye adsorption on Chamaerops humilis fibers biosorption using a central composite design, Desalination Water Treat 320, 100824 (2024).

[34] X. Liu, L. Wang, and Z. L. Xue, Parameter optimization of ultrafine molybdenum powder during hydrogen reduction of MoO2 based on central composite design method, Int J Refract Metals Hard Mater 124, 106845 (2024).

[35] V. Czitrom, One-factor-at-a-time versus designed experiments, American Statistician 53, 126 (1999).

[36] N. Delgarm, B. Sajadi, K. Azarbad, and S. Delgarm, Sensitivity analysis of building energy performance: A simulation-based approach using OFAT and variance-based sensitivity analysis methods, Journal of Building Engineering 15, 181 (2018).

[37] A. Nighojkar, K. Zimmermann, M. Ateia, B. Barbeau, M. Mohseni, S. Krishnamurthy, F. Dixit, and B. Kandasubramanian, Application of neural network in metal adsorption using biomaterials (BMs): a review, Environmental Science Advances 2, 11 (2023).

[38] L. Aydın, H. S. Artem, and S. Oterkus, Designing Engineering Structures Using Stochastic Optimization Methods (CRC Press, 2020).

[39] P. Goos and B. Jones, Optimal Design of Experiments: A Case Study Approach, Optimal Design of Experiments: A Case Study Approach (2011).

[40] S. Narukulla et al., Comparative study between the Full Factorial, Box–Behnken, and Central Composite Designs in the optimization of metronidazole immediate release tablet, Microchemical Journal 207, 111875 (2024).

[41] A. Jankovic, G. Chaudhary, and F. Goia, Designing the design of experiments (DOE) – An investigation on the influence of different factorial designs on the characterization of complex systems, Energy Build 250, 111298 (2021).

[42] M. Tanco, E. Viles, and L. Pozueta, Comparing Different Approaches for Design of Experiments (DoE), Lecture Notes in Electrical Engineering 39 LNEE, 611 (2009).

[43] M. Ohue, K. Sasayama, and M. Takata, Mathematical modeling and problem solving: from fundamentals to applications, Journal of Supercomputing 80, 14116 (2024).

[44] N. Yazdanpanah, Process development and integration by mathematical modeling and simulation tools, Integration and Optimization of Unit Operations: Review of Unit Operations from R&D to Production: Impacts of Upstream and Downstream Process Decisions 273 (2022).

[45] N. Nwulu and S. L. Gbadamosi, Mathematical Optimization Modeling and Solution Approaches, Green Energy and Technology 37 (2021).

[46] L. Aydın, H. S. Artem, and S. Oterkus, Designing Engineering Structures Using Stochastic Optimization Methods (CRC Press, 2020).

[47] C. Bruni, A. Forcellese, F. Gabrielli, and M. Simoncini, Modelling of the rheological behaviour of aluminium alloys in multistep hot deformation using the multiple regression analysis and artificial neural network techniques, J Mater Process Technol 177, 323 (2006).

[48] S. Tanrıverdi and L. Aydın, Optimization of Process Parameters for Green Composites in Abrasive Water Jet Machining Process Using Neuro-Regression Analysis, Journal of Artificial Intelligence and Data Science 1, 71 (2021).

[49] E. S. Koksal and E. Aydin, Physics Informed Piecewise Linear Neural Networks for Process Optimization, Comput Chem Eng 174, 108244 (2023).

[50] W. A. Poe and S. Mokhatab, Process Optimization, Modeling, Control, and Optimization of Natural Gas Processing Plants 173 (2017).

[51] A. K. Qin, V. L. Huang, and P. N. Suganthan, Differential evolution algorithm with strategy adaptation for global numerical optimization, IEEE Transactions on Evolutionary Computation 13, 398 (2009).

[52] R. Storn and K. Price, Differential Evolution - A Simple and Efficient Heuristic for Global Optimization over Continuous Spaces, Journal of Global Optimization 11, 341 (1997).

[53] S. Kirkpatrick, C. D. Gelatt, and M. P. Vecchi, Optimization by Simulated Annealing, Science (1979) 220, 671 (1983).

[54] L. Ingber, Simulated annealing: Practice versus theory, Math Comput Model 18, 29 (1993).

[55] J. A. Nelder and R. Mead, A Simplex Method for Function Minimization, Comput J 7, 308 (1965).

[56] P. Mehta, B. S. Yildiz, S. Kumar, N. Pholdee, S. M. Sait, N. Panagant, S. Bureerat, and A. R. Yildiz, A Nelder Mead-infused INFO algorithm for optimization of mechanical design problems, Materialpruefung/Materials Testing 64, 1172 (2022).

[57] J. Bergstra and Y. Bengio, Random search for hyper-parameter optimization, The Journal of Machine Learning Research 13, 281 (2012).

[58] Z. B. Zabinsky, Random Search Algorithms, Wiley Encyclopedia of Operations Research and Management Science (2011).

[59] C. J. Bae, A. B. Diggs, and A. Ramachandran, Quantification and certification of additive manufacturing materials and processes, Additive Manufacturing: Materials, Processes, Quantifications and Applications 181 (2018).

[60] J. Parthasarathy, B. Starly, and S. Raman, A design for the additive manufacture of functionally graded porous structures with tailored mechanical properties for biomedical applications, J Manuf Process 13, 160 (2011).

[61] T. D. Ngo, A. Kashani, G. Imbalzano, K. T. Q. Nguyen, and D. Hui, Additive manufacturing (3D printing): A review of materials, methods, applications and challenges, Compos B Eng 143, 172 (2018).

[62] M. D. Monzón, Z. Ortega, A. Martínez, and F. Ortega, Standardization in additive manufacturing: activities carried out by international organizations and projects.

[63] I. Gibson, D. Rosen, B. Stucker, and M. Khorasani, Additive Manufacturing Technologies, Additive Manufacturing Technologies (2021).

[64] ASTM F2792-10. Standard Terminology for Additive Manufacturing Technologies, Copyright ASTM International, 100 Barr Harbor Drive, West Conshohocken, PA 19428, https://www.astm.org/.

[65] B. Blakey-Milner, P. Gradl, G. Snedden, M. Brooks, J. Pitot, E. Lopez, M. Leary, F. Berto, and A. du Plessis, Metal additive manufacturing in aerospace: A review, Mater Des 209, 110008 (2021).

[66] W. J. Sames, I. F. A. List, S. Pannala, R. R. Dehoff, and S. S. Babu, The metallurgy and processing science of metal additive manufacturing, International Materials Reviews 61, 315 (2016).

[67] K. S. Prakash, T. Nancharaih, and V. V. S. Rao, Additive Manufacturing Techniques in Manufacturing -An Overview, Mater Today Proc 5, 3873 (2018).

[68] S. Kumar, A. K. S. Choudhary, A. Kishore, S. Amit, K. Gupta, and U. G. Student, A Comparison of Additive Manufacturing Technologies, IJIRST-International Journal for Innovative Research in Science & Technology| 3, (2016).

[69] S. Cooke, K. Ahmadi, S. Willerth, and R. Herring, Metal additive manufacturing: Technology, metallurgy and modelling, J Manuf Process 57, 978 (2020).

[70] K. Özsoy, B. Duman, and D. İ. Gültekin, Metal Part Production with Additive Manufacturing for Aerospace and Defense Industry, International Journal of Technological Sciences 11, 201 (2019).

[71] H. L. Wei, T. Mukherjee, W. Zhang, J. S. Zuback, G. L. Knapp, A. De, and T. DebRoy, Mechanistic models for additive manufacturing of metallic components, Prog Mater Sci 116, 100703 (2021).

[72] R. Konecna, F. Uriati, G. Nicoletto, and V. Tibor, Surface quality and fatigue behavior of L-PBF AlSi10Mg in as-built condition, Procedia Structural Integrity 34, 135 (2021).

[73] J. L. Leirmo and I. Baturynska, Challenges and proposed solutions for aluminium in laser powder bed fusion, Procedia CIRP 93, 114 (2020).

[74] L. Dowling, J. Kennedy, S. O'Shaughnessy, and D. Trimble, A review of critical repeatability and reproducibility issues in powder bed fusion, Mater Des 186, (2020).

[75] M. A. Obeidi, Metal additive manufacturing by laser-powder bed fusion:Guidelines for process optimisation, Results in Engineering 15, 100473 (2022).

[76] Z. Liu, B. He, T. Lyu, and Y. Zou, A Review on Additive Manufacturing of Titanium Alloys for Aerospace Applications: Directed Energy Deposition and Beyond Ti-6Al-4V, JOM 73, 1804 (2021).

[77] D. G. Ahn, Directed Energy Deposition (DED) Process: State of the Art, International Journal of Precision Engineering and Manufacturing-Green Technology 2021 8:2 8, 703 (2021).

[78] M. Jiménez, L. Romero, I. A. Domínguez, M. D. M. Espinosa, and M. Domínguez, Additive Manufacturing Technologies: An Overview about 3D Printing Methods and Future Prospects, Complexity 2019, (2019).

[79] J. H. Schneberger, J. Kaspar, and M. Vielhaber, Post-processing and testing-oriented design for additive manufacturing – A general framework for the development of hybrid AM parts, Procedia CIRP 90, 91 (2020).

[80] A. Nazir, K. M. Abate, A. Kumar, and J. Y. Jeng, A state-of-the-art review on types, design, optimization, and additive manufacturing of cellular structures, The International Journal of Advanced Manufacturing Technology 2019 104:9 104, 3489 (2019).

[81] J. Liu, J. Ye, D. Silva Izquierdo, A. Vinel, N. Shamsaei, and S. Shao, A review of machine learning techniques for process and performance optimization in laser beam powder bed fusion additive manufacturing, J Intell Manuf 34, 3249 (2023).

[82] İ. Gökdağ and E. Acar, Simultaneous optimization of topology and process parameters for laser-powder bed fusion additive manufacturing, Structural and Multidisciplinary Optimization 66, 1 (2023).

[83] K. A. Shiyas and R. Ramanujam, A review on post processing techniques of additively manufactured metal parts for improving the material properties, Mater Today Proc 46, 1429 (2021).

[84] L. Hackel, J. R. Rankin, A. Rubenchik, W. E. King, and M. Matthews, Laser peening: A tool for additive manufacturing post-processing, Addit Manuf 24, 67 (2018).

[85] E. Maleki, S. Bagherifard, N. Razavi, M. Bandini, A. du Plessis, F. Berto, and M. Guagliano, On the efficiency of machine learning for fatigue assessment of post-processed additively manufactured AlSi10Mg, Int J Fatigue 160, 106841 (2022).

[86] P. D. Enrique, A. Keshavarzkermani, R. Esmaeilizadeh, S. Peterkin, H. Jahed, E. Toyserkani, and N. Y. Zhou, Enhancing fatigue life of additive manufactured parts with electrospark deposition post-processing, Addit Manuf 36, 101526 (2020).

[87] S. Yadav, T. A. Jack, R. K. Zadeh Davani, E. Ohaeri, and J. Szpunar, Effect of post-processing heat treatment on hydrogen embrittlement susceptibility of API 5L X70 pipeline steel, International Journal of Pressure Vessels and Piping 199, 104762 (2022).

[88] S. Afkhami, M. Dabiri, H. Piili, and T. Björk, Effects of manufacturing parameters and mechanical post-processing on stainless steel 316L processed by laser powder bed fusion, Materials Science and Engineering: A 802, 140660 (2021).

[89] S. Pal, H. R. Tiyyagura, I. Drstvenšek, and C. S. Kumar, The Effect of Post-processing and Machining Process Parameters on Properties of Stainless Steel PH1 Product Produced by Direct Metal Laser Sintering, Procedia Eng 149, 359 (2016).

[90] X. Shui, K. Yamanaka, M. Mori, Y. Nagata, K. Kurita, and A. Chiba, Effects of post-processing on cyclic fatigue response of a titanium alloy additively manufactured by electron beam melting, Materials Science and Engineering: A 680, 239 (2017).

[91] A. H. Maamoun, M. A. Elbestawi, and S. C. Veldhuis, Influence of Shot Peening on AlSi10Mg Parts Fabricated by Additive Manufacturing, Journal of Manufacturing and Materials Processing 2018, Vol. 2, Page 40 2, 40 (2018).

[92] L. Wagner and C. Mueller, Effect of shot peening on fatigue behavior in al-alloys, Materials and Manufacturing Processes 7, 423 (1992).

[93] N. E. Uzan, S. Ramati, R. Shneck, N. Frage, and O. Yeheskel, On the effect of shot-peening on fatigue resistance of AlSi10Mg specimens fabricated by additive manufacturing using selective laser melting (AM-SLM), Addit Manuf 21, 458 (2018).

[94] M. B. Djukic, W. A. Curtin, Z. Zhang, and A. Sedmak, Recent Advances on Hydrogen Embrittlement Understanding and Future Research Framework, Editorial, Eng Fract Mech 241, 107439 (2021).

[95] M. B. Djukic, G. M. Bakic, V. S. Zeravcic, A. Sedmak, and B. Rajicic, Hydrogen embrittlement of industrial components: Prediction, prevention, and models, Corrosion 72, 943 (2016).

[96] H. Yu, A. Cocks, and E. Tarleton, Discrete dislocation plasticity HELPs understand hydrogen effects in bcc materials, J Mech Phys Solids 123, 41 (2019).

[97] Y. Gu and J. A. El-Awady, Quantifying the effect of hydrogen on dislocation dynamics: A three-dimensional discrete dislocation dynamics framework, J Mech Phys Solids 112, 491 (2018).

[98] M. Alnajjar, E. Christien, E. Bosch, and K. Wolski, A comparative study of microstructure and hydrogen embrittlement of selective laser melted and wrought 17-4 PH stainless steel, Materials Science and Engineering: A 785, 139363 (2020).

[99] S. W. Baek, E. J. Song, J. H. Kim, M. Jung, U. B. Baek, and S. H. Nahm, Hydrogen embrittlement of 3-D printing manufactured austenitic stainless-steel part for hydrogen service, Scr Mater 130, 87 (2017).

[100] L. Barsanti, M. Cabrini, T. Pastore, and C. Spinelli, Effect of microstructure on the hydrogen-embrittlement behaviour of HSLA steels under cathodic protection, Environment-Induced Cracking of Materials 279 (2008).

[101] O. Takakuwa and H. Soyama, Suppression of hydrogen-assisted fatigue crack growth in austenitic stainless steel by cavitation peening, Int J Hydrogen Energy 37, 5268 (2012).

[102] X. Li, J. Zhang, Y. Wang, M. Ma, S. Shen, and X. Song, The dual role of shot peening in hydrogen-assisted cracking of PSB1080 high strength steel, Mater Des 110, 602 (2016).

[103] E. Lunarska and D. Samatowicz, The hydrogen-induced modification of the properties of the metal surface coated with oil and lubricant, Tribol Int 33, 491 (2000).

[104] A. Behvar, M. Haghshenas, and M. B. Djukic, Hydrogen embrittlement and hydrogen-induced crack initiation in additively manufactured metals: A critical review on mechanical and cyclic loading, Int J Hydrogen Energy 58, 1214 (2024).

[105] D. Sobola and R. Dallaev, Exploring Hydrogen Embrittlement: Mechanisms, Consequences, and Advances in Metal Science, Energies 2024, Vol. 17, Page 2972 17, 2972 (2024).

[106] A. Islam, T. Alam, N. Sheibley, K. Edmonson, D. Burns, and M. Hernandez, Hydrogen blending in natural gas pipelines: A comprehensive review of material compatibility and safety considerations, Int J Hydrogen Energy 93, 1429 (2024).

[107] S. P. Lynch, Progress Towards Understanding Mechanisms Of Hydrogen Embrittlement And Stress Corrosion Cracking.

[108] W. Li, X. Zhu, C. Wang, and X. Jin, Effect of S-phase on the Hydrogen Induced Phase Transition and Hydrogen Embrittlement Susceptibility in AISI 304 Stainless Steel, Mater Today Proc 2, S691 (2015).

[109] S. L. Lee and D. J. Unger, A Decohesion Model of Hydrogen Assisted Cracking, Eng Fract Mech (1988).

[110] M. B. Djukic, G. M. Bakic, V. Sijacki Zeravcic, A. Sedmak, and B. Rajicic, The synergistic action and interplay of hydrogen embrittlement mechanisms in steels and iron: Localized plasticity and decohesion, Eng Fract Mech 216, (2019).

[111] M. S. Hasan, M. F. Kapci, B. Bal, M. Koyama, H. Bayat, and W. Xu, An atomistic study on the HELP mechanism of hydrogen embrittlement in pure metal Fe, Int J Hydrogen Energy 57, 60 (2024).

[112] M. B. Djukic, V. Sijacki Zeravcic, G. M. Bakic, A. Sedmak, and B. Rajicic, Hydrogen damage of steels: A case study and hydrogen embrittlement model, Eng Fail Anal 58, 485 (2015).

[113] B. N. Popov, J. W. Lee, and M. B. Djukic, Hydrogen Permeation and Hydrogen-Induced Cracking, Handbook of Environmental Degradation Of Materials: Third Edition 133 (2018).

[114] M. Wasim and M. B. Djukic, External corrosion of oil and gas pipelines: A review of failure mechanisms and predictive preventions, J Nat Gas Sci Eng 100, 104467 (2022).

[115] H. W. Lee, M. B. Djukic, and C. Basaran, Modeling fatigue life and hydrogen embrittlement of bcc steel with unified mechanics theory, Int J Hydrogen Energy 48, 20773 (2023).

[116] D. H. Lee, B. Sun, S. Lee, D. Ponge, E. A. Jägle, and D. Raabe, Comparative study of hydrogen embrittlement resistance between additively and conventionally manufactured 304L austenitic stainless steels, Materials Science and Engineering: A 803, 140499 (2021).

[117] S. W. Baek, E. J. Song, J. H. Kim, M. Jung, U. B. Baek, and S. H. Nahm, Hydrogen embrittlement of 3-D printing manufactured austenitic stainless steel part for hydrogen service, Scr Mater 130, 87 (2017).

[118] S. Li, Y. Li, Y. C. Lo, T. Neeraj, R. Srinivasan, X. Ding, J. Sun, L. Qi, P. Gumbsch, and J. Li, The interaction of dislocations and hydrogen-vacancy complexes and its importance for deformation-induced proto nano-voids formation in α-Fe, Int J Plast 74, 175 (2015).

[119] X. Lu, D. Wang, D. Wan, Z. B. Zhang, N. Kheradmand, and A. Barnoush, Effect of electrochemical charging on the hydrogen embrittlement susceptibility of alloy 718, Acta Mater 179, 36 (2019).

[120] A. Zafra, G. Álvarez, G. Benoit, G. Henaff, E. Martinez-Pañeda, C. Rodríguez, and J. Belzunce, Hydrogen-assisted fatigue crack growth: Pre-charging vs in-situ testing in gaseous environments, Materials Science and Engineering: A 871, 144885 (2023).

[121] M. F. Baltacioglu, B. Cetin, and B. Bal, The Effect of Strain Rate on the Hydrogen Embrittlement Susceptibility of Aluminum 7075, J Eng Mater Technol 145, (2023).

[122] C. Park, N. Kang, and S. Liu, Effect of grain size on the resistance to hydrogen embrittlement of API 2W Grade 60 steels using in situ slow-strain-rate testing, Corros Sci 128, 33 (2017).

[123] M. Wasim and M. B. Djukic, External corrosion of oil and gas pipelines: A review of failure mechanisms and predictive preventions, J Nat Gas Sci Eng 100, 104467 (2022).

[124] L. Wagner and C. Mueller, Effect of shot peening on fatigue behavior in al-alloys, Materials and Manufacturing Processes 7, 423 (1992).

[125] M. Daoud, R. Kubler, A. Bemou, P. Osmond, and A. Polette, Prediction of residual stress fields after shot-peening of TRIP780 steel with second-order and artificial neural network models based on multi-impact finite element simulations, J Manuf Process 72, 529 (2021).

[126] B. AlMangour and J. M. Yang, Improving the surface quality and mechanical properties by shot-peening of 17-4 stainless steel fabricated by additive manufacturing, Mater Des 110, 914 (2016).

[127] K. Mallieswaran, S. Rajasekaran, M. Vinoth Kumar, and C. Rajendran, Steel shot peening effects on friction stir welded AA2014-T6 aluminum alloys, Materialpruefung/Materials Testing 64, 1202 (2022).

[128] M. Kahlin, H. Ansell, D. Basu, A. Kerwin, L. Newton, B. Smith, and J. J. Moverare, Improved fatigue strength of additively manufactured Ti6Al4V by surface post processing, Int J Fatigue 134, 105497 (2020).

[129] A. K. Gujba and M. Medraj, Laser peening process and its impact on materials properties in comparison with shot peening and ultrasonic impact peening, Materials 7, 7925 (2014).

[130] A. Rajesh, P. Ashoka Varthanan, J. Srikant, T. Shoban, K. S. Sanjaykanna, and P. V. Suchith, Optimization of shot peening process parameters using PSO algorithm to maximise the fatigue strength, flexural strength and surface hardness of AA2024-T3 alloy, Mater Today Proc (2021).

[131] A. Teo, K. Ahluwalia, and A. Aramcharoen, Experimental investigation of shot peening: correlation of pressure and shot velocity to Almen intensity, International Journal of Advanced Manufacturing Technology 106, 4859 (2020).

[132] J. O. Almen, P. H. Black, and T. J. Dolan, Residual Stresses And Fatigue In Metals, J Appl Mech 31, 368 (1963).

[133] J. O. Almen, P. H. Black, and T. J. Dolan, Residual Stresses And Fatigue In Metals, J Appl Mech 31, 368 (1963).

[134] A. M. S. B. F. P. and F. Committee, Shot Peening.

[135] A. M. S. E. C. and L. A. S. Committee, Steel Strip 0.64-0.76C (SAE 1070).

[136] S. E. Committee, Procedures for Using Standard Shot Peening Almen Test Strip.

[137] S. E. Committee, Shot Peening Coverage Determination.

[138] S. E. Committee, Test Strip, Holder, and Gage for Shot Peening.

[139] H. Y. Miao, D. Demers, S. Larose, C. Perron, and M. Lévesque, Experimental study of shot peening and stress peen forming, J Mater Process Technol 210, 2089 (2010).

[140] H. Y. Miao, D. Demers, S. Larose, C. Perron, and M. Lévesque, Experimental study of shot peening and stress peen forming, J Mater Process Technol 210, 2089 (2010).

[141] X. Wang, Z. Wang, G. Wu, J. Gan, Y. Yang, H. Huang, J. He, and H. Zhong, Combining the finite element method and response surface methodology for optimization of shot peening parameters, Int J Fatigue 129, (2019).

[142] B. S. Yildiz, N. Pholdee, P. Mehta, S. M. Sait, S. Kumar, S. Bureerat, and A. R. Yildiz, A novel hybrid flow direction optimizer-dynamic oppositional based learning algorithm for solving complex constrained mechanical design problems, Materialpruefung/Materials Testing 65, 134 (2023).

[143] P. Mehta, B. S. Ylldlz, S. M. Sait, and A. R. Ylldlz, Gradient-based optimizer for economic optimization of engineering problems, Materialpruefung/Materials Testing 64, 690 (2022).

[144] Z. Wang, P. Zhang, Q. Zhang, L. Zhou, R. Abd Ali, W. Chen, and L. Xie, Process-based deep learning model: 3D prediction method for shot peen forming of an aircraft panel, Chinese Journal of Aeronautics (2023).

[145] A. Nazir, K. M. Abate, A. Kumar, and J. Y. Jeng, A state-of-the-art review on types, design, optimization, and additive manufacturing of cellular structures, The International Journal of Advanced Manufacturing Technology 2019 104:9 104, 3489 (2019).

[146] G. Taguchi, System of Experimental Design: Engineering Methods to Optimize Quality and Minimize Costs (UNIPUB/Kraus International Publications, 1987).

[147] A. C. Atkinson, A. N. Donev, and R. D. Tobias, Optimum Experimental Design With Sas, Optimum Experimental Designs, with SAS.

[148] B. Ait-Amir, P. Pougnet, and A. El Hami, Meta-Model Development, in Embedded Mechatronic Systems, Vol. 2 (Elsevier, 2015), pp. 151–179.

[149] M. Savran and L. Aydin, Stochastic optimization of graphite-flax/epoxy hybrid laminated composite for maximum fundamental frequency and minimum cost, Eng Struct 174, 675 (2018).

[150] P. Mehta, B. S. Yildiz, S. Kumar, N. Pholdee, S. M. Sait, N. Panagant, S. Bureerat, and A. R. Yildiz, A Nelder Mead-infused INFO algorithm for optimization of mechanical design problems, Materialpruefung/Materials Testing 64, 1172 (2022).

[151] S. Ozturk, L. Aydin, and E. Celik, A comprehensive study on slicing processes optimization of silicon ingot for photovoltaic applications, Solar Energy 161, 109 (2018).

[152] M. C. Fu, Feature Article: Optimization for simulation: Theory vs. Practice, INFORMS J Comput 14, 192 (2002).

[153] J. Zhang and A. C. Sanderson, JADE, IEEE Transactions on Evolutionary Computation 13, 945 (2009).

[154] Z. Gao, T. Xiao, and W. Fan, Hybrid differential evolution and Nelder-Mead algorithm with re-optimization, Soft Comput 15, 581 (2011).

[155] A. Ramasubramaniam, M. Itakura, M. Ortiz, and E. A. Carter, Effect of atomic scale plasticity on hydrogen diffusion in iron: Quantum mechanically informed and on-the-fly kinetic Monte Carlo simulations, J Mater Res 23, 2757 (2008).

[156] A. Beukers, M. Van Tooren, and C. Vermeeren, Aircraft structures in the century ahead: From arts to science, from craftsmanship to multidisciplinary design and engineering, The Aeronautical Journal 107, 343 (2003).

[157] E. A. Starke and J. T. Staley, Application of modern aluminum alloys to aircraft, Progress in Aerospace Sciences 32, 131 (1996).

[158] A. Kumar Sharma, R. Bhandari, C. Sharma, S. Krishna Dhakad, and C. Pinca-Bretotean, Polymer matrix composites: A state of art review, Mater Today Proc 57, 2330 (2022).

[159] J. B. Rae, Science and Engineering in the History of Aviation, Technol Cult 2, 391 (1961).

[160] D. D. Boyd, A review of general aviation safety (1984-2017), Aerosp Med Hum Perform 88, 657 (2017).

[161] Aviation Results, https://www.ntsb.gov/Pages/ResultsV2.aspx?queryId=c36fa52b-395f-4135-a089-d3601cc8ea35 (21.05.2025).

[162] Safety Reports, https://www.icao.int/safety/pages/safety-report.aspx (21.05.2025).

[163] F. De Florio, Airworthiness: An introduction to aircraft certification, Airworthiness: An Introduction to Aircraft Certification 1 (2010).

[164] D. Lercel Ph.D., M. Patankar Ph.D., and R. Steckel Ph.D., Assessing Past Airworthiness Directives And How Safety Management Systems May Benefit Aviation Product Design And Manufacturing, Journal of Aviation/Aerospace Education & Research 33, 6 (2024).

[165] Dynamic Regulatory System, https://drs.faa.gov/browse/ADFRAWD/doctypeDetai ls (21.05.2025).

[166] M. L. Martin and P. Sofronis, Hydrogen-induced cracking and blistering in steels: A review, J Nat Gas Sci Eng 101, 104547 (2022).

[167] R. A. Oriani and P. H. Josephic, Equilibrium aspects of hydrogen-induced cracking of steels, Acta Metallurgica 22, 1065 (1974).

[168] S. K. Dwivedi and M. Vishwakarma, Hydrogen embrittlement in different materials: A review, Int J Hydrogen Energy 43, 21603 (2018).

[169] N. E. Laadel, M. El Mansori, N. Kang, S. Marlin, and Y. Boussant-Roux, Permeation barriers for hydrogen embrittlement prevention in metals – A review on mechanisms, materials suitability and efficiency, Int J Hydrogen Energy 47, 32707 (2022).

[170] S. Lynch, Hydrogen embrittlement phenomena and mechanisms, Corrosion Reviews 30, 105 (2012).

[171] X. Li, X. Ma, J. Zhang, E. Akiyama, Y. Wang, and X. Song, Review of Hydrogen Embrittlement in Metals: Hydrogen Diffusion, Hydrogen Characterization, Hydrogen Embrittlement Mechanism and Prevention, Acta Metallurgica Sinica (English Letters) 33, 759 (2020).

[172] H. K. Birnbaum and P. Sofronis, Hydrogen-enhanced localized plasticity—a mechanism for hydrogen-related fracture, Materials Science and Engineering: A 176, 191 (1994).

[173] Maciej Serda et al., Hydrogen enhanced localized plasticity: A mechanism for hydrogen related fracture, Uniwersytet Śląski 7, 15 (1993).

[174] S. P. Lynch, Environmentally assisted cracking: Overview of evidence for an adsorption-induced localised-slip process, Acta Metallurgica 36, 2639 (1988).

[175] S. P. Lynch, Hydrogen embrittlement (HE) phenomena and mechanisms, Stress Corrosion Cracking: Theory and Practice 90 (2011).

[176] J. Song and W. A. Curtin, A nanoscale mechanism of hydrogen embrittlement in metals, Acta Mater 59, 1557 (2011).

[177] J. Song and W. A. Curtin, Atomic mechanism and prediction of hydrogen embrittlement in iron, Nature Materials 2012 12:2 12, 145 (2012).

[178] X. Li, J. Yin, J. Zhang, Y. Wang, X. Song, Y. Zhang, and X. Ren, Hydrogen embrittlement and failure mechanisms of multi-principal element alloys: A review, J Mater Sci Technol 122, 20 (2022).

[179] Airbus Identifies Heat, Humidity As Causes Of A380 Wing-Spar Cracking | Aviation Week Network, https://aviationweek.com/air-transport/safety-ops-regulation/airbus-identifies-heat-humidity-causes-a380-wing-spar-cracking&utm_source=chatgpt.com.

[180] H. Zhao, P. Wang, and J. Li, Effect of vanadium content on hydrogen embrittlement of 1400 MPa grade high strength bolt steels, Int J Hydrogen Energy 46, 34983 (2021).

[181] K. C. Lan, Y. T. Chen, H. M. Tung, Y. F. Tseng, and Y. C. Li, Hydrogen permeation resistance of ZrN thin film deposited by ion-plating, Surf Coat Technol 484, 130866 (2024).

[182] R. Fratesi and G. Roventi, Corrosion resistance of Zn-Ni alloy coatings in industrial production, Surf Coat Technol 82, 158 (1996).

[183] D. Hardie, E. A. Charles, and A. H. Lopez, Hydrogen embrittlement of high strength pipeline steels, Corros Sci 48, 4378 (2006).

[184] E. M. K. Hillier and M. J. Robinson, Hydrogen embrittlement of high strength steel electroplated with zinc–cobalt alloys, Corros Sci 46, 715 (2004).

[185] Y. Fan, Y. Huang, B. Cui, and Q. Zhou, Graphene coating on nickel as effective barriers against hydrogen embrittlement, Surf Coat Technol 374, 610 (2019).

[186] J. Xue, C. Zhou, P. Dai, X. Liu, H. Wu, X. Li, and P. K. Chu, Manipulating nano-WS2 aggregates in electroplated Ni coating to mitigate hydrogen embrittlement in X70 pipeline steel, Corros Sci 241, 112517 (2024).

[187] S. H. Hong, H. J. Cho, S. Kim, S. Y. Song, H. Chung, S. kyu Lee, S. Lee, S. S. Sohn, and S. J. Kim, Enhancing resistance to hydrogen embrittlement in high-strength hot-press-forming steel sheets through Al-Si-Zn coating optimization, Acta Mater 283, 120527 (2025).

[188] L. S. Araujo, L. H. de Almeida, and D. S. dos Santos, Hydrogen embrittlement of a hard chromium plated cylinder assembly, Eng Fail Anal 103, 259 (2019).

[189] R. Singh, A. Arab, A. Caceres, R. Eybel, and M. Medraj, Establishing industrial Zn-Ni brush electroplating process without post-plating hydrogen embrittlement relief baking, Surf Coat Technol 478, 130363 (2024).

[190] S. Wu, Z. Gao, Y. Liu, and W. Hu, Effect of cathodic protection potential on stress corrosion susceptibility of X80 steel, Corros Sci 218, 111184 (2023).

[191] P. Yin, X. Li, W. Lu, Y. Chen, Z. Yang, B. Zhang, Y. Guo, J. Ding, and R. Cao, Effect of Cathodic Potentials on the Hydrogen Embrittlement Susceptibility of 10Ni5CrMo Steel, Int J Electrochem Sci 14, 8479 (2019).

[192] L. Sanchez and H. Cong, AC interference on hydrogen absorption in low carbon steel under cathodic protection, Int J Hydrogen Energy 48, 1202 (2023).

[193] X. Wang, Y. Wang, B. Wang, Y. Xing, M. Lu, L. Qiao, and L. Zhang, Effect of scratches on hydrogen embrittlement sensitivity of carbon steel in cathodic protection and dynamic DC stray current interference environments, International Journal of Pressure Vessels and Piping 199, 104712 (2022).

[194] X. Chen, F. Xie, D. Wang, D. Sun, M. Wu, and Y. Li, Hydrogen-induced cracking of X70 steel affected by sulfate-reducing bacteria and cathodic potential: experiment and density functional theory study, Int J Hydrogen Energy 49, 798 (2024).

[195] Q. Xu and J. Zhang, Novel Methods for Prevention of Hydrogen Embrittlement in Iron, Scientific Reports 2017 7:1 7, 1 (2017).

[196] A. Khare, M. Vishwakarma, and V. Parashar, A Review on Failures of Industrial Components due to Hydrogen Embrittlement & Techniques for Damage Prevention, International Journal of Applied Engineering Research 12, 1784 (2017).

[197] H. J. Kim, H. K. Park, C. W. Lee, B. G. Yoo, and H. Y. Jung, Baking Effect on Desorption of Diffusible Hydrogen and Hydrogen Embrittlement on Hot-Stamped Boron Martensitic Steel, Metals 2019, Vol. 9, Page 636 9, 636 (2019).

[198] H. S. Han, K. H. Lee, S. H. Park, S. Park, and M. K. Song, The effect of baking time, fillet radius, and hardness on the lifecycles of pole fastening screws in an electric motor with hydrogen embrittlement, Eng Fail Anal 48, 62 (2015).

[199] C. K. Soundararajan, D. Wang, and A. Vinogradov, Effect of hydrogen on nanomechanical properties of Inconel 625 studied using in-situ electrochemical nanoindentation technique, J Alloys Compd 948, 169742 (2023).

[200] X. An et al., Investigation of the interaction between hydrogen and irradiation defects in titanium by using positron annihilation spectroscopy, Int J Hydrogen Energy 46, 13162 (2021).

[201] A. Basa, D. Wang, N. Espallargas, and D. Wan, An In-Situ Electrochemical Nanoindentation (ECNI) Study on the Effect of Hydrogen on the Mechanical Properties of 316L Austenitic Stainless Steel, Materials 2021, Vol. 14, Page 6426 14, 6426 (2021).

[202] G. Hultquist, M. J. Graham, J. L. Smialek, and B. Jönsson, Hydrogen in metals studied by Thermal Desorption Spectroscopy (TDS), Corros Sci 93, 324 (2015).

[203] F. Von Zeppelin, M. Haluška, and M. Hirscher, Thermal desorption spectroscopy as a quantitative tool to determine the hydrogen content in solids, Thermochim Acta 404, 251 (2003).

[204] A. Campari, F. Ustolin, A. Alvaro, and N. Paltrinieri, A review on hydrogen embrittlement and risk-based inspection of hydrogen technologies, Int J Hydrogen Energy 48, 35316 (2023).

[205] S. Samanta, P. Kumari, K. Mondal, M. Dutta, and S. B. Singh, An alternative and comprehensive approach to estimate trapped hydrogen in steels using electrochemical permeation tests, Int J Hydrogen Energy 45, 26666 (2020).

[206] O. Takakuwa, T. Fujisawa, and H. Soyama, Experimental verification of the hydrogen concentration around a crack tip using spot X-ray diffraction, Int J Hydrogen Energy 41, 23188 (2016).

[207] S. Li, M. Liu, Y. Ren, and Y. Wang, Hydrogen embrittlement behaviors of additive manufactured maraging steel investigated by in situ high-energy X-ray diffraction, Materials Science and Engineering: A 766, 138341 (2019).

[208] R. Yasuda, M. Nakata, M. Matsubayashi, K. Harada, Y. Hatakeyama, and H. Amano, Application of hydrogen analysis by neutron imaging plate method to Zircaloy cladding tubes, Journal of Nuclear Materials 320, 223 (2003).

[209] S. Shukla, R. N. Singh, Y. S. Kashyap, T. N. Murty, N. Keskar, T. Roy, P. Singh, and M. Shukla, Anisotropy study of hydrogen diffusion along different directions of Zr-2.5%Nb alloy pressure tube using neutron imaging, Journal of Nuclear Materials 580, 154414 (2023).

[210] ERA10TA493-NTSB Docket - Docket Management System, https://data.ntsb.gov/Docket/?NTSBNumber=ERA10TA493 (21.05.2025).

[211] CEN10FA291 - NTSB Docket - Docket Management System, https://data.ntsb.gov/Docket/?NTSBNumber=ERA10TA493 (21.05.2025).

[212] IAD02FA091-NTSB Docket - Docket Management System, https://data.ntsb.gov/Docket/?NTSBNumber=IAD02FA091 (21.05.2025).

[213] MIA02LA108-NTSB Docket - Docket Management System, https://data.ntsb.gov/Docket/?NTSBNumber=MIA02LA108 (21.05.2025).

[214] ENG08IA025-NTSB Docket - Docket Management System, https://data.ntsb.gov/Docket/?NTSBNumber=ENG08IA025 (21.05.2025).

[215] M. Khorram Niaki and F. Nonino, What Is Additive Manufacturing? Additive Systems, Processes and Materials, 1 (2018).

[216] W. E. Frazier, Metal additive manufacturing: A review, J Mater Eng Perform 23, 1917 (2014).

[217] K. Kempen, L. Thijs, J. Van Humbeeck, and J. P. Kruth, Mechanical Properties of AlSi10Mg Produced by Selective Laser Melting, Phys Procedia 39, 439 (2012).

[218] E. Brandl, U. Heckenberger, V. Holzinger, and D. Buchbinder, Additive manufactured AlSi10Mg samples using Selective Laser Melting (SLM): Microstructure, high cycle fatigue, and fracture behavior, Mater Des 34, 159 (2012).

[219] A. H. Maamoun, Y. F. Xue, M. A. Elbestawi, and S. C. Veldhuis, The Effect of Selective Laser Melting Process Parameters on the Microstructure and Mechanical Properties of Al6061 and AlSi10Mg Alloys, Materials (Basel) 12, (2018).

[220] E. Beevers, A. D. Brandão, J. Gumpinger, M. Gschweitl, C. Seyfert, P. Hofbauer, T. Rohr, and T. Ghidini, Fatigue properties and material characteristics of additively manufactured AlSi10Mg – Effect of the contour parameter on the microstructure, density, residual stress, roughness and mechanical properties, Int J Fatigue 117, 148 (2018).

[221] C. Li, Z. Y. Liu, X. Y. Fang, and Y. B. Guo, Residual Stress in Metal Additive Manufacturing, Procedia CIRP 71, 348 (2018).

[222] W. Muhammad, J. Kang, and K. Inal, The competing role of defects and surface roughness on the fatigue behavior of additively manufactured AlSi10Mg alloy, Int J Fatigue 177, 107965 (2023).

[223] I. Rosenthal, A. Stern, and N. Frage, Strain rate sensitivity and fracture mechanism of AlSi10Mg parts produced by Selective Laser Melting, Materials Science and Engineering: A 682, 509 (2017).

[224] A. Salandari Rabori and V. Fallah, Room temperature strain rate sensitivity of as-built 3D printed AlSi10Mg by laser powder bed fusion, Mater Lett 320, 132395 (2022).

[225] N. B. Ghisi, H. Ramos, L. Kindleyside, N. T. Aboulkhair, and R. Santiago, The influence of the characteristic microstructure of additively manufactured AlSi10Mg on the plastic behaviour at various strain rates, Mater Des 223, 111112 (2022).

[226] E. Maleki, S. Bagherifard, O. Unal, A. Jam, S. Shao, M. Guagliano, and N. Shamsaei, Superior effects of hybrid laser shock peening and ultrasonic nanocrystalline surface modification on fatigue behavior of additive manufactured AlSi10Mg, Surf Coat Technol 463, 129512 (2023).

[227] Q. Zhang, B. Duan, Z. Zhang, J. Wang, and C. Si, Effect of ultrasonic shot peening on microstructure evolution and corrosion resistance of selective laser melted Ti–6Al–4V alloy, Journal of Materials Research and Technology 11, 1090 (2021).

[228] A. Tridello, J. Fiocchi, C. A. Biffi, G. Chiandussi, M. Rossetto, A. Tuissi, and D. S. Paolino, VHCF response of Gaussian SLM AlSi10Mg specimens: Effect of a stress relief heat treatment, Int J Fatigue 124, 435 (2019).

[229] A. Speidel, R. Sélo, I. Bisterov, J. Mitchell-Smith, and A. T. Clare, Post processing of additively manufactured parts using electrochemical jet machining, Mater Lett 292, 129671 (2021).

[230] J. Damon, S. Dietrich, F. Vollert, J. Gibmeier, and V. Schulze, Process dependent porosity and the influence of shot peening on porosity morphology regarding selective laser melted AlSi10Mg parts, Addit Manuf 20, 77 (2018).

[231] L. Wagner, M. Mhaede, M. Wollmann, I. Altenberger, and Y. Sano, Surface layer properties and fatigue behavior in Al 7075-T73 and Ti-6Al-4V Comparing results after laser peening; Shot peening and ball-burnishing, International Journal of Structural Integrity 2, 185 (2011).

[232] B. Bal, B. Okdem, F. C. Bayram, and M. Aydin, A detailed investigation of the effect of hydrogen on the mechanical response and microstructure of Al 7075 alloy under medium strain rate impact loading, Int J Hydrogen Energy 45, 25509 (2020).

[233] R. A. Oriani, Hydrogen Embrittlement of Steels, Annual Review of Materials Science 8, 327 (1978).

[234] B. E. Wilde and I. Chattoraj, The effect of shot peening on hydrogen absorption by and hydrogen permeation through AISI 4130 steels, Scripta Metallurgica et Materialia 26, 627 (1992).

[235] W. H. Johnson, On some remarkable changes produced in iron and steel by the action of hydrogen and acids, Proceedings of the Royal Society of London 23, 168 (1875).

[236] Y. Hong, C. Zhou, S. Wagner, S. Schlabach, A. Pundt, L. Zhang, and J. Zheng, Corrigendum to "Strain-induced twins and martensite: Effects on hydrogen embrittlement of selective laser melted (SLM) 316L stainless steel", Corros Sci 215, 111041 (2023).

[237] Y. Hong, C. Zhou, S. Wagner, S. Schlabach, A. Pundt, L. Zhang, and J. Zheng, Strain-induced twins and martensite: Effects on hydrogen embrittlement of selective laser melted (SLM) 316 L stainless steel, Corros Sci 208, 110669 (2022).

[238] W. H. Kan, Y. Nadot, M. Foley, L. Ridosz, G. Proust, and J. M. Cairney, Factors that affect the properties of additively-manufactured AlSi10Mg: Porosity versus microstructure, Addit Manuf 29, 100805 (2019).

[239] K. Kempen, L. Thijs, J. Van Humbeeck, and J. P. Kruth, Mechanical Properties of AlSi10Mg Produced by Selective Laser Melting, Phys Procedia 39, 439 (2012).

[240] N. ; Read, W. ; Wang, K. ; Essa, and Attallah, Selective laser melting of AlSi10Mg alloy: Process optimisation and mechanical properties development, Mater Des 65, 417 (2015).

[241] Y. Wang, X. Wu, Z. Zhou, and X. Li, Numerical analysis of hydrogen transport into a steel after shot peening, Results Phys 11, 5 (2018).

[242] Y. Wang, H. Xie, Z. Zhou, X. Li, W. Wu, and J. Gong, Effect of shot peening coverage on hydrogen embrittlement of a ferrite-pearlite steel, Int J Hydrogen Energy 45, 7169 (2020).

[243] E. Edin, F. Svahn, M. Neikter, and P. Åkerfeldt, Stress relief heat treatment and mechanical properties of laser powder bed fusion built 21-6-9 stainless steel, Materials Science and Engineering: A 868, 144742 (2023).

[244] E. Edin, F. Svahn, P. Åkerfeldt, M. Eriksson, and M. L. Antti, Rapid method for comparative studies on stress relief heat treatment of additively manufactured 316L, Materials Science and Engineering: A 847, 143313 (2022).

[245] M. Frkan, R. Konecna, G. Nicoletto, and L. Kunz, Microstructure and fatigue performance of SLM-fabricated Ti6Al4V alloy after different stress-relief heat treatments, Transportation Research Procedia 40, 24 (2019).

[246] J.-Y. Lee, A. P. Nagalingam, and S. H. Yeo, A review on the state-of-the-art of surface finishing processes and related ISO/ASTM standards for metal additive manufactured components, Https://Doi.Org/10.1080/17452759.2020.1830346 16, 68 (2020).

[247] P. Sofronis and R. M. McMeeking, Numerical analysis of hydrogen transport near a blunting crack tip, J Mech Phys Solids 37, 317 (1989).

[248] I. M. Robertson, P. Sofronis, A. Nagao, M. L. Martin, S. Wang, D. W. Gross, and K. E. Nygren, Hydrogen Embrittlement Understood, Metall Mater Trans A Phys Metall Mater Sci 46, 2323 (2015).

[249] Y. Zheng, Z. Zhao, R. Xiong, G. Ren, M. Yao, W. Liu, and L. Zang, Effect of post heat treatment on microstructure, mechanical property and corrosion behavior of AlSi10Mg alloy fabricated by selective laser melting, Progress in Natural Science: Materials International 34, 89 (2024).

[250] R. Ramesh, S. Gairola, R. Jayaganthan, and M. Kamaraj, Effects of post-processing on the microstructural evolution and mechanical behaviour of an additively manufactured AlSi10Mg alloy, Journal of Materials Research and Technology 34, 2802 (2025).

[251] R. F. Fernandes, J. S. Jesus, R. Branco, L. P. Borrego, J. D. Costa, and J. A. M. Ferreira, Effect of low-temperature stress relieving heat treatments on fatigue behaviour and failure mechanisms of L-PBF AlSi10Mg aluminium alloy, Eng Fail Anal 169, 109210 (2025).

[252] M. L. Montero Sistiaga, R. Mertens, B. Vrancken, X. Wang, B. Van Hooreweder, J. P. Kruth, and J. Van Humbeeck, Changing the alloy composition of Al7075 for better processability by selective laser melting, J Mater Process Technol 238, 437 (2016).

[253] H. Hyer, L. Zhou, A. Mehta, S. Park, T. Huynh, S. Song, Y. Bai, K. Cho, B. McWilliams, and Y. Sohn, Composition-dependent solidification cracking of aluminum-silicon alloys during laser powder bed fusion, Acta Mater 208, 116698 (2021).

[254] Y. Li, C. Chen, and F. Zhang, Al and Si Influences on Hydrogen Embrittlement of Carbide-Free Bainitic Steel, Advances in Materials Science and Engineering 2013, 382060 (2013).

[255] L. Chen, S. Antonov, K. Song, H. Zhi, W. Li, Y. Chen, K. Hu, Y. Zhong, Y. Su, and L. Qiao, Effect of solute atoms (C, Al and Si) on hydrogen embrittlement resistance of high-Mn TWIP steels, Corros Sci 203, 110376 (2022).

[256] H. Jian, M. Yang, W. Fang, J. Pai, and X. Yang, Effect of Heat Treatment on Microstructure and Properties of Selective Laser Melting AlSi10Mg Alloy, J Mater Eng Perform 1 (2024).

[257] X. Xing, X. Duan, T. Jiang, J. Wang, and F. Jiang, Ultrasonic Peening Treatment Used to Improve Stress Corrosion Resistance of AlSi10Mg Components Fabricated Using Selective Laser Melting, Metals 2019, Vol. 9, Page 103 9, 103 (2019).

CURRICULUM VITAE

2011 – 2016	B.Sc., Materials Engineering, Yıldırım Beyazıt University, Ankara, TURKİYE
2017 – 2018	M.Sc., Advanced Materials and Nanotechnology, Abdullah Gül University, Kayseri, TURKİYE
2018 – Present	Ph.D. Candidate, Materials Science and Mechanical Engineering, Abdullah Gül University, Kayseri, TURKİYE
2021 – Present	MRB Structural Design Engineer, Turkish Aerospace Industries, Ankara, TURKİYE

SELECTED PUBLICATIONS AND PRESENTATIONS

J1) B. Bal, **K. K. Karaveli**, B. Cetin, B. Gumus, The Precise Determination of the Johnson–Cook Material and Damage Model Parameters and Mechanical Properties of an Aluminum 7068-T651 Alloy published in Journal of Engineering Materials and Technology (Feb. 2019).

J2) K. K. Karaveli, B. Bal, Comprehensive optimization of shot peening intensity using a hybrid model with AI-based techniques via Almen tests published in Journal of Materials Testing (June 2025).

C1) K. K. Karaveli, B. Bal, Mechanical Responses of Lightweight Aluminum Alloys and Their Applications in The International Conference on Materials Science and Technology in Cappadocia (IMSTEC'18) (Sep. 2018).

C2) K. K. Karaveli, B. Bal, Effects of Shot Peening on Mechanical Performance and Optimization Strategies in 10th National Aviation and Space Conference (Sep. 2024).

C3) K. K. Karaveli, B. Bal, Investigation of the Effects of Secondary Processes and Strain Rate on the Mechanical Behavior of AlSi10Mg Alloys Produced by Additive Manufacturing in Anadolu 17th International Conference on Applied Sciences (May 2025).

C4) K. K. Karaveli, B. Bal, Numerical Modeling of Parametric Interactions in Shot Peening Process and a Hybrid Optimization Approach Based on Artificial Intelligence in Anadolu 17th International Conference on Applied Sciences (May 2025).